Development of a Priest Interferometer for
Measurement of the Thermal Expansion of
Graphite-Epoxy in the Temperature
Range 116-366K

Virginia Polytechnic Inst. and State Univ.
Blacksburg

Prepared for

National Aeronautics and Space Administration
Langley Station, VA

Sep 82

DEPARTMENT OF DEFENSE
PLASTICS TECHNICAL EVALUATION CENTER
ARRADCOM, DOVER, N. J. 07801
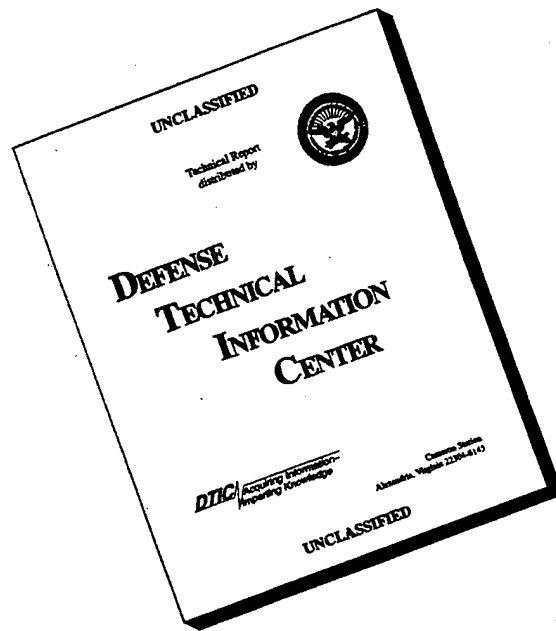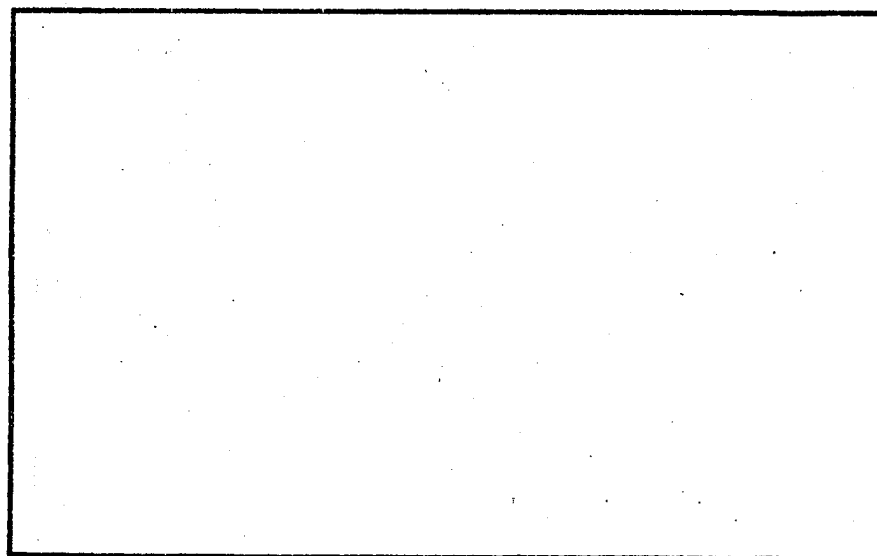
19960315 020

PLASTIC

DISCLAIMER NOTICE

THIS DOCUMENT IS BEST
QUALITY AVAILABLE. THE
COPY FURNISHED TO DTIC
CONTAINED A SIGNIFICANT
NUMBER OF PAGES WHICH DO
NOT REPRODUCE LEGIBLY.

COLLEGE
OF
ENGINEERING

VIRGINIA
POLYTECHNIC
INSTITUTE
AND
STATE
UNIVERSITY

BLACKSBURG,
VIRGINIA

College of Engineering

Virginia Polytechnic Institute and State University

Blacksburg, VA 24061

VPI-E-82-18   September 1982

Development of a Priest Interferometer for
Measurement of the Thermal Expansion of
Graphite-Epoxy in the Temperature
Range 116-366K

John S. Short[1]
Michael W. Hyer[2]   David E. Bowles[4]
Daniel Post[3]   Stephen S. Tompkins[5]

Department of Engineering Science & Mechanics

[1]Graduate student now with Carolina Power and Light Co.

[2]Associate Professor of Engineering Science & Mechanics

[3]Professor of Engineering Science & Mechanics

[4]Materials Engineer, Materials Division, NASA-Langley

[5]Senior Scientist, Materials Division, NASA-Langley

BIBLIOGRAPHIC DATA SHEET	1. Report No. VPI-E-82-18	2.	3. Recipient's Accession No. SPX 116640

4. Title and Subtitle	5. Report Date
Development of a Priest Interferometer for Measurement of the Thermal Expansion of Graphite-Epoxy in the Temperature Range 116-366K	September 1982
	6.

7. Author(s)	8. Performing Organization Re No.
Short, J.S.; Hyer, M.W.; Post, D.; Bowles, D.E.; Tompkins, S.S.	VPI-E-82-18

9. Performing Organization Name and Address	10. Project/Task/Work Unit N
Virginia Polytechnic Institute and State University Department of Engineering Science and Mechanics Blacksburg, VA 24061	
	11. Contract/Grant No. CA NCC1-15

12. Sponsoring Organization Name and Address	13. Type of Report & Period Covered
National Aeronautics and Space Administration Langley Research Center Hampton, VA 23665	Interim
	14.

15. Supplementary Notes

16. Abstracts

The thermal expansion behavior of graphite epoxy laminates between 116 and 366 degrees Kelvin was investigated using a novel implementation of the Priest interfero meter concept. This report describes the design, construction and use of the inter ferometer along with the experimental results it was used to generate.

The experimental program consisted of 25 tests on 25.4 mm and 6.35 mm wide, 8-
π/4 quasi-isotropic T300-5208 graphite/epoxy specimens and 3 tests on a 25.4 mm wide unidirectional specimen. Experimental results are presented for all tests along wit a discussion of the interferometer's limitations and some possible improvements in its design.

17. Key Words and Document Analysis. 17a. Descriptors

thermal expansion
composite materials
Priest interferometer
Fizeau interferometer
graphite-epoxy
environmental effects

17b. Identifiers/Open-Ended Terms

17c. COSATI Field/Group 24-01, 39-08, 39-02, 39-07, 35

18. Availability Statement	19. Security Class (This Report) UNCLASSIFIED	21. No. of Pages 133
Release unlimited	20. Security Class (This Page) UNCLASSIFIED	22. Price

FORM NTIS-35 (REV. 10-73)   ENDORSED BY ANSI AND UNESCO.   THIS FORM MAY BE REPRODUCED   USCOMM-DC 8265-

ABSTRACT

The thermal expansion behavior of graphite epoxy laminates between 116 and 366 degrees Kelvin was investigated using a novel implementaticn of the Priest interferometer concept. This repcrt describes the design, construction and use of the interferometer along with the experimental results it was used to generate.

The experimental program consisted of 25 tests on 25.4 mm and 6.35 mm wide, 8-ply $\pi/4$ quasi-isotropic T300-5208 graphite/epoxy specimens and 3 tests on a 25.4 mm wide unidirectional specimen. Experimental results are presented for all tests along with a discussion of the interferometer's limitations and some possible improvements in its design.

ACKNOWLEDGEMENTS

TABLE OF CONTENTS

LIST OF TABLES

LIST OF FIGURES

Chapter 1

INTRODUCTION

1.1 Fiber Reinforced Composites

Fiber-reinforced composite materials offer vast improvements in the structural performance of aircraft and spacecraft components. Also, when compared with more conventional materials such as aluminum or titanium, the cost to fabricate a component from fiber-reinforced materials is in many instances less than the cost to fabricate the same component from metal. The ability to orient fibers in preferred directions, in addition to the high specific strength and stiffness of the fiber materials, has led to these improvements. Future components fabricated from fiber-reinforced composites will see wider usage of laminates employing several types of fibers, laminates which use improvements in the curing process, laminates which take advantage of the elastic coupling available, and laminates which employ high strain-to-failure matrix materials.

While these features will no doubt lead to even further improvements in structural performance, future gains in performance will also come about because of innovative laminate design. These laminate designs will result through efforts to take full advantage of the orthotropic nature of the mechanical and thermal properties of the individual lamina. Each lamina will be chosen to have material properties and fiber orientation so that the overall laminate properties are tailored to meet certain specifications.

1

The unique nature of composites must be exploited, of course, in the context of a specific problem. It is not possible to make general statements regarding novel laminate design. It is possible, however, to say that certain material and structural problems probably could not be solved without the use of fiber reinforced composites.

To date, there have been several design problems for which tailored laminates have been a solution. One of these problems is the aeroelastic tailoring of aircraft wings and control surfaces. In this case, through a proper selection of lamina thickness and orientation, the bending-twist coupling of lifting surface primary structures are controlled. This results in minimized drag and efficient spanwise load distributions along the lifting surface. In another application, the fiber-reinforced composites are used in an orbiting antenna design. The antenna is launched into orbit as a small compact package. Once this package is in orbit, the antenna is formed by the unfurling of the fiber-reinforced composite ribs and other members of the antenna dish. Finally, and more associated with the subject of the present work, fiber-reinforced composite laminates have been designed to have specific thermal expansion properties. Graphite fibers contract when heated while resin matrix materials expand. By choosing the proper percentage of fibers and matrix and by judicious selection of fiber direction, specific thermal expansion characteristics can be obtained. One of the primary focuses of this effort has been to fabricate laminates which have minimal thermal deformation when subjected to temperature changes. An example of the tailoring of laminates to have specific thermal expan-

sion properties is shown in Fig. 1.1. This figure is taken from a recent publication [1] and illustrates how several families of laminates can be tailored to have a specific coefficient of thermal expansion. The information in the figures is theoretical, the results being based on classical lamination theory. From the figure it is clear that a laminate can be made to have a positive, negative, or zero coefficient of thermal expansion.

The information presented in Fig. 1.1 must be interpreted correctly. Bowles, et al. [2] have shown that thermal deformation characteristics of most graphite-epoxy composite materials are nonlinear functions of temperature. Although the nonlinearity is weak, it is less than exact to assume a constant coefficient of thermal expansion is valid over a wide temperature range. Thus Fig. 1.1 should be interpreted to mean that for small temperature excursions around a particular temperature, it is possible to design a laminate with specific thermal deformation characteristics, including the case of no deformation. This is not to say a laminate cannot be designed to have zero deformation as a result of the temperature changing significantly, say several hundred degrees centigrade. However, caution should be used when interpreting theoretical results.

1.2 Large Space Structures

Because of the potential for zero or even negative expansion characteristics, fiber-reinforced composites are being considered for use in large orbiting space structures where dimensional stability is critical
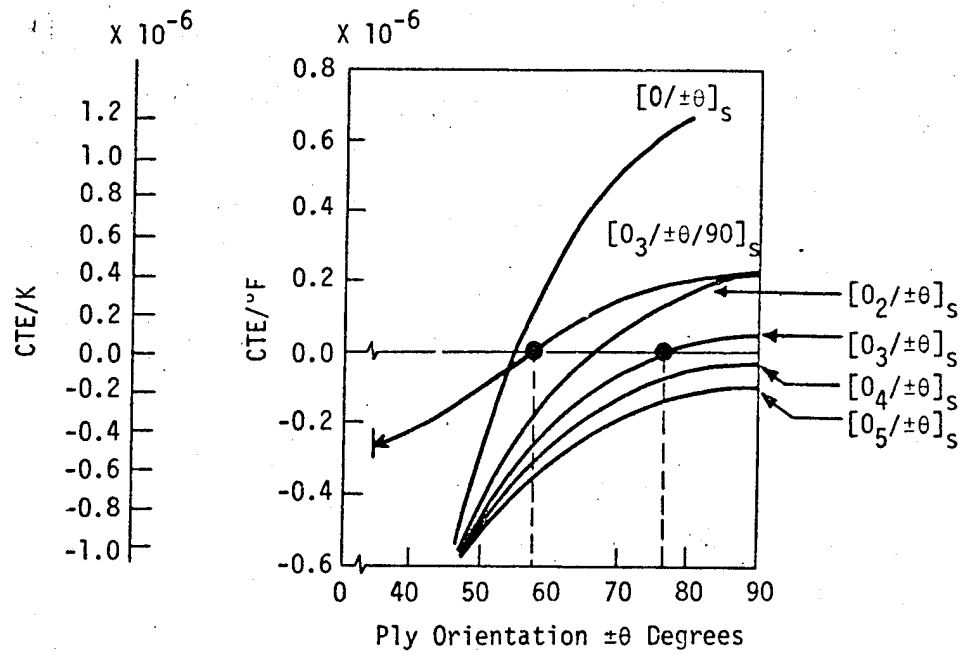
Fig. 1.1 Sensitivity of Laminate CTE to
Fiber Orientation, θ

and, in fact, the primary design goal. Global crop monitoring, large

scale pollution assessment, and soil moisture content measurements are

but a few proposed applications of large space structures. The common

characteristic of such structures is their antenna-like shape. However,

because of the desire for resolution measurements regarding, for exam-

ple, the depth of soil moisture, the wavelength of the electromagnetic

radiation used to survey the land area of interest requires large dia-

meter antennas. Parabolic antennas up to 1000 meters in diameter are

envisioned.

To keep the antenna tuned to a particular wavelength, the shape of

the parabolic antenna must remain fixed to within a very fine tolerance.

The antenna may well be in such an orbit that throughout its orbital

trajectory the orientation of the sun's rays relative to the antenna

surface is constantly changing. Because of the periodic nature of the

orbit, such a condition would cause the antenna's temperature to change

in a periodic fashion. This would in turn cause the parabolic shape of

the antenna to distort periodically. While electronics may be able to

compensate for some of this shape distortion, it would be desirable to

have a structure that was very close to being thermally inert as far as

thermal deformations are concerned. In light of Fig. 1.1, it appears

that fiber-reinforced composites can be used to advantage in such struc-

tures.

Because of this application, there has been much interest in under-

standing the thermo-mechanical behavior of fiber-reinforced composites.

Specifically, because of their high stiffness and strength, attention

has been focused on graphite-epoxy composites. General designs of large orbiting structures have evolved but nothing is concrete. It appears that the first generation structures will be composed of long slender members, primarily in compression, and thinner members, perhaps wires, in tension. These members will be connected together to form frame-work and lattice structures. The connectors will be designed for easy assembly by astronauts, remote manipulators, or robots. Specific stiffness and strength requirements are still quite general but it is clear that if shape stability is critical, the structural materials have to possess finely controlled thermal expansion characteristics.

Although thermal expansion will need to be controlled, it is not clear that zero expansion materials are a goal. Connectors may well be the worst offenders for maintaining dimensional stability, with structural members having to compensate for the large expansivities of the connectors. Consider, for example, a member 100 units long which has a connector one unit long. If the connector expands significantly when heated, the member itself will have to contract the same amount if a total deformation of zero is required. Thus, since the member is 100 units long, the material in the member must have a negative expansion characteristic 1/100th of the positive characteristic of the connector material. If, for example, the connector is aluminum with a coefficient of thermal expansion of 24×10^{-6}/K, then the material in the member itself must have a negative thermal expansion coefficient of 0.24×10^{-6}/K. Negative expansion characteristics may be of more interest than zero expansion characteristics.

Whether ultimate interest in positive, zero, or negative character-
isics, much effort must still be made to fully understand the thermo-
mechanical characteristics of fiber-reinforced composites under the con-
ditions encountered in space.

1.3 Space Environment and Composite Behavior

The space environment is a very dry, hard vacuum environment with
ambient temperatures in the neighborhood of 116K (-250°F). Due to the
lack of atmosphere, radiant heating and cooling effects can be quite
dramatic. Also, due to the lack of atmospheric filtering effects,
structures in space will experience ultraviolet radiation and high ener-
gy electron bombardment at levels much greater than those normally en-
countered on earth.

This environment is in itself quite harsh. However, in addition to
operating in this environment, large space structures must be designed
to have a long service life. Thus if composites are to be used in di-
mensionally stable space structures, their long term thermo-mechanical
behavior under a light load, in a hard vacuum, and exposed to varying
amounts of heating, cooling, and radiation must be understood. Specif-
ically, the effect of these operating conditions on composite behavior
as a function of laminate design must be quantified.

1.4 Purpose of Present Work

It is difficult to imagine that the first attempts at understanding
behavior of composites in space would involve the building of an experi-

mental apparatus to measure material response in an accurately simulated space environment. Such a task would be overwhelming. The approach which has to be taken is to build environmental chambers, loading fixtures, measuring devices, etc. one step at a time, in iterative fashion, so that experimental techniques and hardware can be refined. These refinements would be based on experience gained in studying the behavior of composites as experiments progress. In this iterative approach, analytical theories of composite behavior can be tested and special measurements made to help validate particular theories.

In any iterative process there is always the question of where to start. As mentioned in Section 1.2, there is current interest in graphite-epoxy fiber-reinforced composites for use in dimensionally stable space structures. Unfortunately, little or no data exists which describes the behavior of these materials in space. Thus, a logical starting place, and the one selected as the subject of this work, is the measurement of the thermal deformations of graphite-epoxy. Specifically, in this work, thermal deformations were measured for temperatures ranging from 116K to 366K (-250° to 200°F), the temperature range encountered in the space environment.

The following chapters describe the design and operation of an experimental device which was built to make these thermal deformation measurements. Also presented are quantitative experimental results regarding the thermal deformation of quasi-isotropic and unidirectional graphite-epoxy laminates. The primary goals of these experiments were to assess the repeatability of the thermal deformations of one specimen

in repeated tests and to assess tne similarity of the thermal deforma-
tion of identical specimens. Also of interest was the effect of
specimen width on the measured thermal deformation characteristics.

Chapter 2

EXPERIMENTAL APPARATUS

2.1 Selection of Measurement Technique

Bowles, et al. [2], in their previous work on thermal strain measurement for graphite-epoxy laminates, posed the following requirements for any thermal strain measurement technique for fiber-reinforced composites:

i) The method should have the capability to measure very small as well as intermediate strains with a high degree of accuracy,

ii) it should be capable of measuring strains under static and cyclic thermal loading, as well as combined thermal and mechanical loading, and,

iii) it should be easy to maintain and operate without the need of complicated experimenal equipment and procedures.

They went on to describe a particular optical interferometer technique, moiré interferometry with fringe multiplication, which was considered to meet these criteria.

Wolff [3] has presented a comprehensive review of small strain measurement techniques in which he distinguishes three categories of techniques:

i) electro-mechanical techniques (resistance strain gage, LVDT);

ii) optical non-interferometric techniques (autocollimator);

ii) optical interferometric techniques (Michelson, Fizeau, moiré).

He compared over thirty separate techniques on the basis of resolution, range, accuracy, and degree of specimen contact required. He concluded that in general, optical techniques were superior.

Other investigators, however, have successfully used electrical resistance strain gages [2,4] and quartz rod dilatometers [5] to measure thermal strains in composites. Obviously, there are a large number of measurement techniques from which to choose. The design criteria used in selecting a technique are discussed below.

2.2 Design Criteria

2.2.1 Resolution

A critical feature of any sensitive measuring device is its ability to detect variation in the measured quantity, i.e. its resolution. Although infinite resolution is ideal, practical limits may be determined for the application here by considering the minimum change in specimen strain which must be reliably detected.

For the graphite-epoxy laminates studied herein, a minimum resolution of 1 µε is chosen. The condition of micro-yielding in fiber-reinforced composites is defined [6] as the occurrence of 1 µε permanent set in the material. Thus, a device which can reliably detect strain differences of 1 µε is, by definition, capable of detecting micro-yielding in a specimen due to, say, resin matrix micro-cracking.

2.2.2 Specimen Geometry

Generally speaking, for large space structures the thermal expansion test specimens will be much, much smaller than the space structures themselves. This difference in size may be significant if, for example, the fiber volume fraction of a small specimen is considerably different than the average volume fraction of the component from which it came. Also, if they are present, the effect of voids, delaminations, or other imperfections must be assessed in terms of their volume relative to the volume of imperfection-free material. Thus, assessment of specimen size effect on thermal response should be possible with the device.

Specimen shape is dictated by specimen fabrication and load application requirements. Flat specimens are easily cut from laminated graphite-epoxy panels and grips which can load such specimens are available or easily built for most mechanical testing machines. For these reasons a flat, variable-width specimen was selected for use. Also, the capacity for variable length specimens was considered in the interferometer design.

2.2.3 Specimen Preparation

As with resolution, the amount of specimen preparation considered minimal is based on each investigator's definition and is thus somewhat arbitrary. Based on previous investigators' experience with strain gauges and moiré gratings, it was decided to rule out techniques which required adhesive application of any transducer to the specimen surface as this can sometimes bias transducer readings. Only point contact or non-contact techniques were considered.

Application of these design criteria quickly narrowed the field of candidate designs to the various optical interferometric techniques. Several Fizeau interferometer schemes were considered. However, the approach finally chosen was that of a very simple Priest interferometer. Most Fizeau interferometers depend on knowing instantaneous interference fringe position to determine changes in specimen length. The Priest interferometer, on the other hand, uses instantaneous fringe density to sense the change of specimen length. This subtle difference can greatly simplify data collection, particularly if the specimen length is changing with time as it would, say, with thermal cycling.

2.3 Theory of Operation

Both Priest and Fizeau interferometers are discussed in ASTM standard E289 [7] and in many elementary books on optics. The ASTM document describes several generic optical interferometric techniques for measuring linear thermal expansion of rigid solids. The method used herein to relate interferometer measurements to thermal deformation is similar to that presented in Ref. 7. However, an additional correction has been included here to account for the out-of-plane rotation of the interferometer components. This correction is discussed in Chapter 3.

The Priest interferometer utilizes an equal thickness (Fizeau) fringe pattern to measure specimen expansion relative to a calibrated reference. Figure 2.1 illustrates a typical Priest interferometer. The top flat is supported in tripod fashion above the bottom flat by two reference support points and one specimen support point. The fringe

Top Flat

Specimen
Support Point

Reference Support
Points (2)
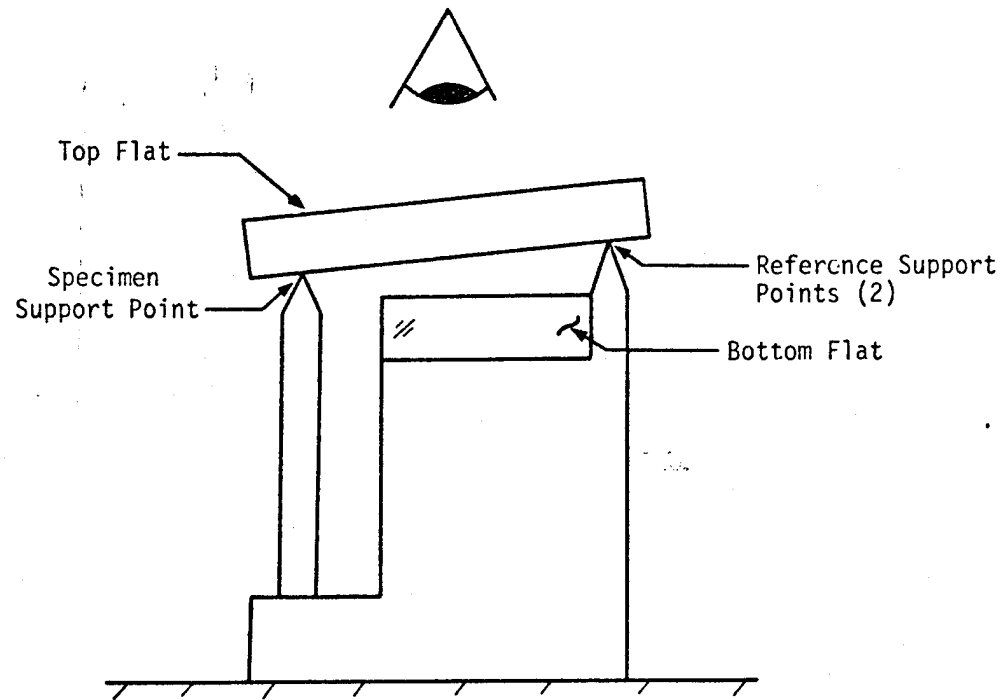
Bottom Flat

Fig. 2.1 Typical Priest Interferometer

pattern is created by interference of wavefronts reflected from the bottom of the top flat and the top of the bottom flat and is visible when looking downward on the device.

When the interferometer is heated both the specimen and the reference material experience thermal deformation. The change in length of the specimen may be expressed as

$$\Delta L_s = \Delta L_{s,r} + \Delta L_r .$$

(2.1)

Here ΔL_s = change in the specimen length,

$\Delta L_{s,r}$ = change in the specimen length relative to a change in the reference length,

ΔL_r = change in the reference length.

In the above formulation, the change in the specimen length is unknown and is the quantity of interest. The change in the specimen length relative to the change in the reference length is the information the interferometer provides. The change in the reference length must be determined from a separate calibration experiment. If the specimen and reference are both the same length, L_0, at the reference temperature, T_0, then at the temperature T the thermal strain in the specimen may be defined as

$$\epsilon_s = \Delta L_s / L_0 ,$$

(2.2)

or

$$\epsilon_s = \epsilon_{s,r} + \epsilon_r ,$$

(2.3)

where

$$\epsilon_{s,r} = \Delta L_{s,r}/L_0 \; , \tag{2.4}$$

and

$$\epsilon_r = \Delta L_r/L_0 \; . \tag{2.5}$$

The required expression for $\epsilon_{s,r}$ in terms of information provided by the Fizeau fringes is derived below.

Consider first Fig. 2.2. In the figure are shown two optical flats which are exposed to an incident collimated light beam. There is a small included angle between the two flats. Plane wavefront n has been reflected from the bottom flat and wavefronts m and m + 1 have been reflected from the top flat. At point a, wave fronts m and n intersect and thus interfere. If, however, we move the top flat up a distance $\lambda/2$, where λ is the wavlength of the incident beam, wavefront m + 1 moves upward a distance λ. Now wavefronts n and m + 1 intersect at a. Thus, a change in the vertical distance between the flats of $\lambda/2$ corresponds to a unit change in interference fringe order at a. This is the basic principle underlying the design of both the Priest and Fizeau interferometers. It can be expressed mathematically as

$$L_a = \frac{N_a \lambda}{2} \; , \tag{2.6}$$

where L_a = change in vertical distance between flats, and N_a = number of fringes which move past point a. In Fig. 2.3 some additional reflected wavefronts are pictured along with an image plane perpendicular to
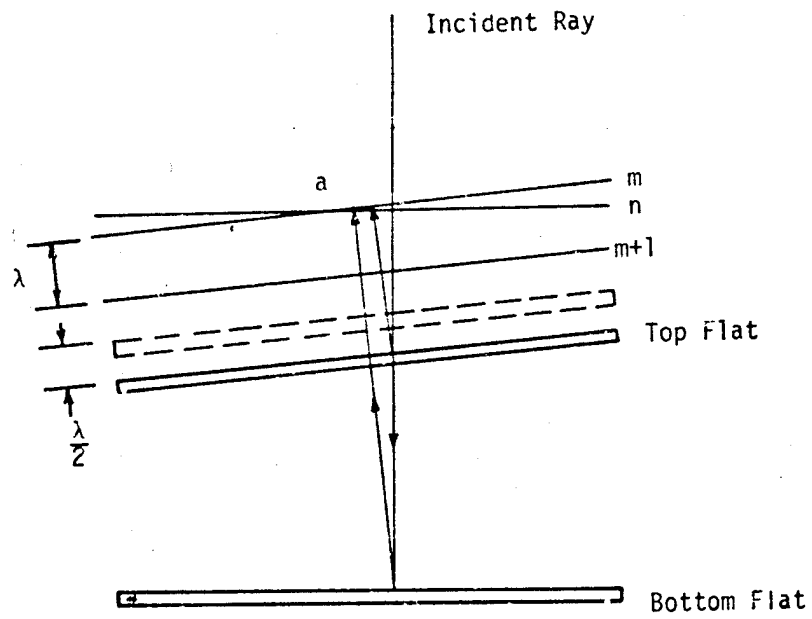
Fig. 2.2   Illustration of Interferometer Sensitivity

the page. It can be seen from the figure that there is a one-to-one corespondence between the impge plane fringe points a", b", and c" and the points a, b, and c which lie along the perpendicular from the bottom flat through a. This relationship is described by as Eqn. (2.6) with L_a now replaced by $L_{c,a}$ and N_a replaced by $N_{c,a}$ where

$$L_{c,a} = h_a - h_c \qquad (2.7)$$

and

$$N_{c,a} = n_a - n_c = (n + 2) - n = 2 . \qquad (2.8)$$

Thus for this case

$$L_{c,a} = \frac{N_{c,a}\lambda}{2} = \lambda . \qquad (2.9)$$

Physically, $L_{c,a}$ is the vertical distance between points a and c and $N_{c,a}$ is the number of fringes viewed in the image plane. Of prime importance is the fact that the difference in vertical distance between point a and c at the top flat is directly related to the number of interference fringes observed in the image (horizontal) plane. This is different than observing, and counting, the number of fringes going past a particular point in the image plane as the flats move vertically, relative to each other. Owing to changes in the angle between flats caused by differential thermal expansion of specimen and reference materials, the fringe density, $N_{c,a}$ will be a function of temperature.

It is now an easy matter to obtain an expression for $\varepsilon_{s,r}$ for use in Eqn. 2.3. Let $\varepsilon_{s,r}$ be represented as
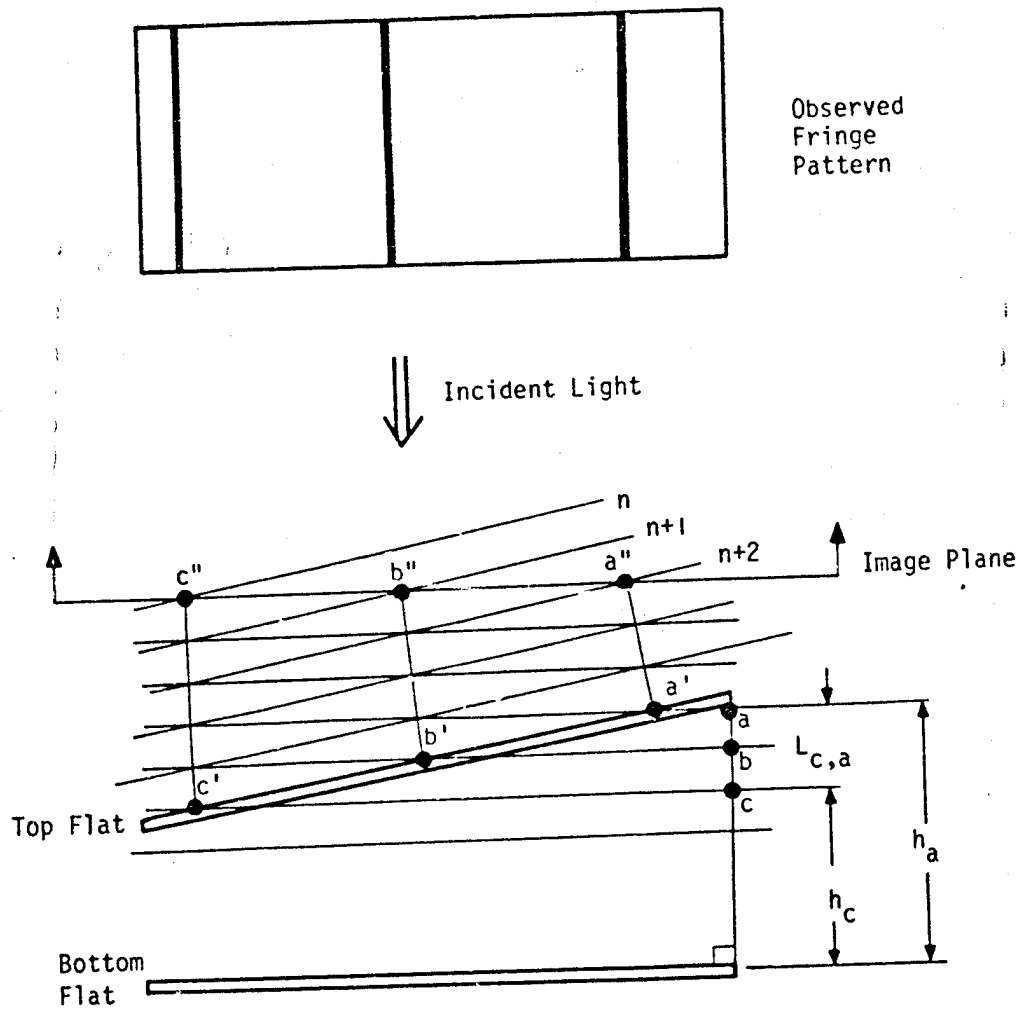
Fig. 2.3 Correspondence of Image Plane Fringes
and Relative Displacement of Top Flat Ends

$$\epsilon_{s,r} = \frac{\Delta L_{s,r}}{L_0} = \frac{L_{s,r}(T) - L_{s,r}(T_0)}{L_0} , \qquad (2.10)$$

where the arguments T_0 and T denote that these lengths are functions of a reference temperature and some other temperature of interest. Referring to Fig. 2.4, $L_{s,r}$ becomes, using Eqn. 2.9,

$$L_{s,r} = \frac{N_f \lambda}{2} , \qquad (2.11)$$

where N_f is the number of fringes which would appear in an interference field of width L_f. It is often convenient to count fringes over some gage distance L_g. In this case N_f can be found using the expression

$$\frac{N_f}{L_f} = \frac{N_g}{L_g} . \qquad (2.12)$$

This is just a mathematical statement of the fact that Fizeau fringes are evenly spaced. Combining Eqns. 2.11 and 2.12 results in

$$L_{s,r} = \frac{N_g \lambda}{2} \frac{L_f}{L_g} . \qquad (2.13)$$

Thus, we may write,

$$L_{s,r}(T_0) = \frac{N_g(T_0) \lambda}{2} \frac{L_f}{L_g} \qquad (2.14)$$

and

$$L_{s,r}(T) = \frac{N_g(T) \lambda}{2} \frac{L_f}{L_g} . \qquad (2.15)$$

Using Eqns. 2.4 and 2.10 and defining $\Delta N = N_g(T) - N_g(T_0)$, the desired expression for $\epsilon_{s,r}$ becomes
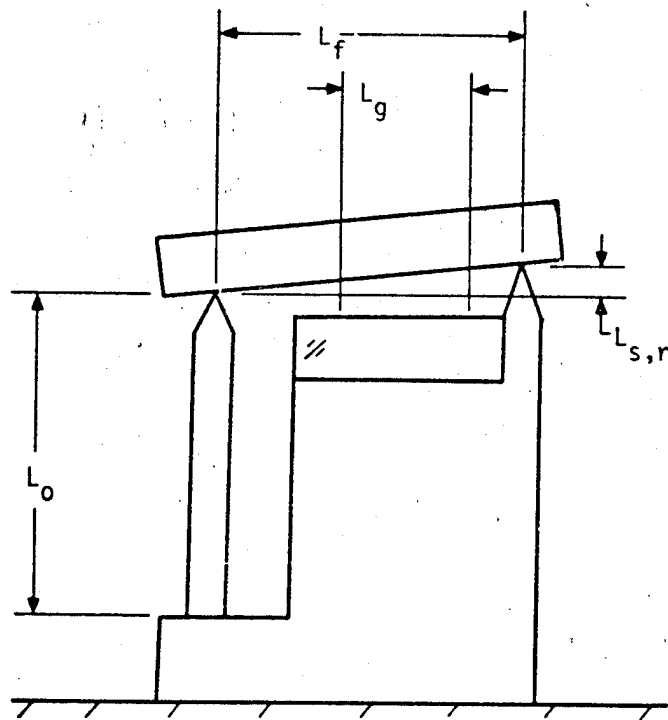
Fig. 2.4 Dimensions Used in Analysis

$$\epsilon_{s,r} = \frac{\Delta N \lambda L_f}{2 L_o L_g} . \qquad (2.16)$$

The corresponding expression for ϵ_s is

$$\epsilon_s = \frac{\Delta N \lambda}{2 L_o} \frac{L_f}{L_g} + \epsilon_r . \qquad (2.17)$$

Several fine points were omitted in the derivation of Eqn. 2.17. These are:

i)   the correction for apparent strain due to the temperature dependence of the index of refraction of the atmostphere between the flats;

ii)   the assumption that the specimen and reference are intially the same length;

iii)   the consideration of apparent strain caused by an unwanted rotational degree of freedom in the top optical flat; and

iv)   the consideration of end effects in the calculation of thermal strains.

These issues are addressed in the next chapter under the heading of data analysis.

2.4   Description of Apparatus

This section describes the specific small strain measurement device developed in this study. A picture of the device appears in Fig. 2.5. The reader may wish to refer to this picture while reading to fix in his

mind the relation of the part being described to the rest of the device. Each component of this system will be decribed in detail.

In essence, the system may be thought of as being composed of three elements:

    i) a transducer (interferometer)

   ii) data processing, (two shelf optical track), and

  iii) environmental control.

The environmental control was provided by an environmental chamber, thermal strains were sensed by the Priest interferometer, and the fringe pattern data were processed using an optical tack of mirror and lenses. Fringe images were recorded with a 35 mm camera.

2.4.1 Interferometer

Figure 2.6 shows an exploded view of the Priest interferometer. The primary components are: the optical flats, the quartz reference rods (quartz rods), and the _pecimen. Figure 2.7 is a photograph showing the assembled interferometer.

2.4.2 Optical Flats

After deciding to use a flat specimen and the Priest interferometer concept, a complete interferometer design was required. The top and bottom optical flats needed to be flat and highly polished. In addition, the flats had to be arranged to minimize the air gap between them. This minimizes uncertainties in optical path length due to laser wavelength drift. This problem is discussed in [8].
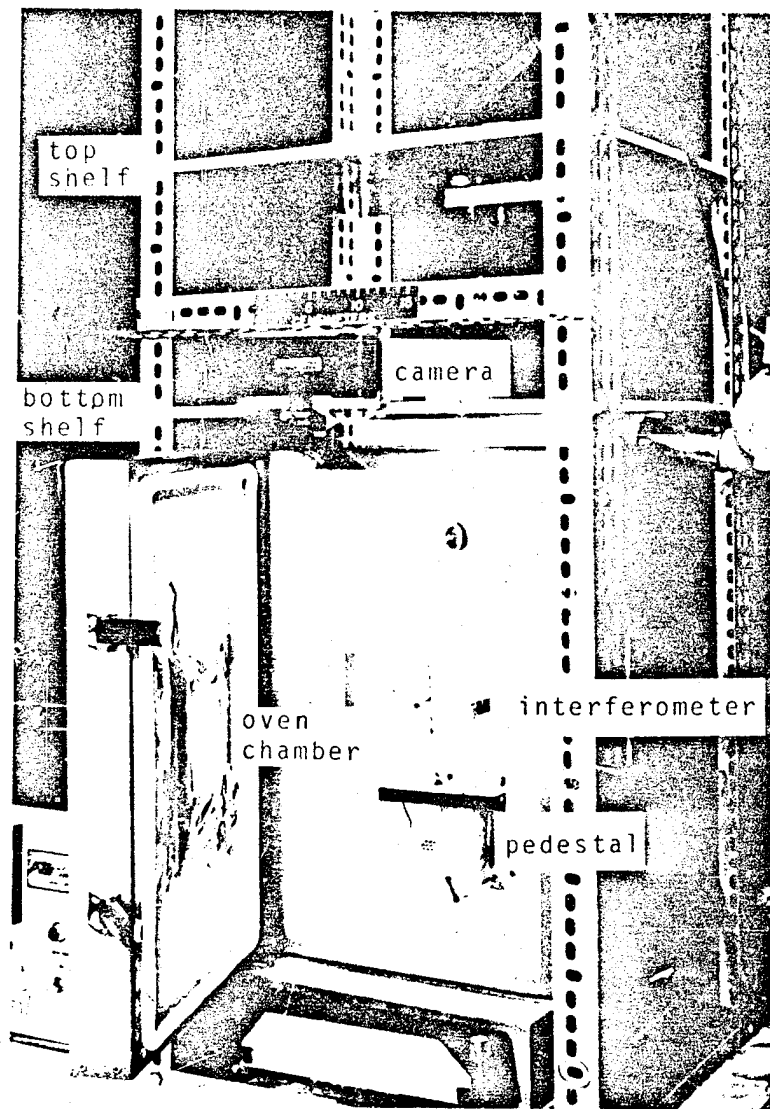
Fig. 2.5 Overall View of Experimental Apparatus

bottom flat

specimen

quartz rod spring (2)

specimen
spring

quartz rod (2)

top
flat

CENTIMETERS
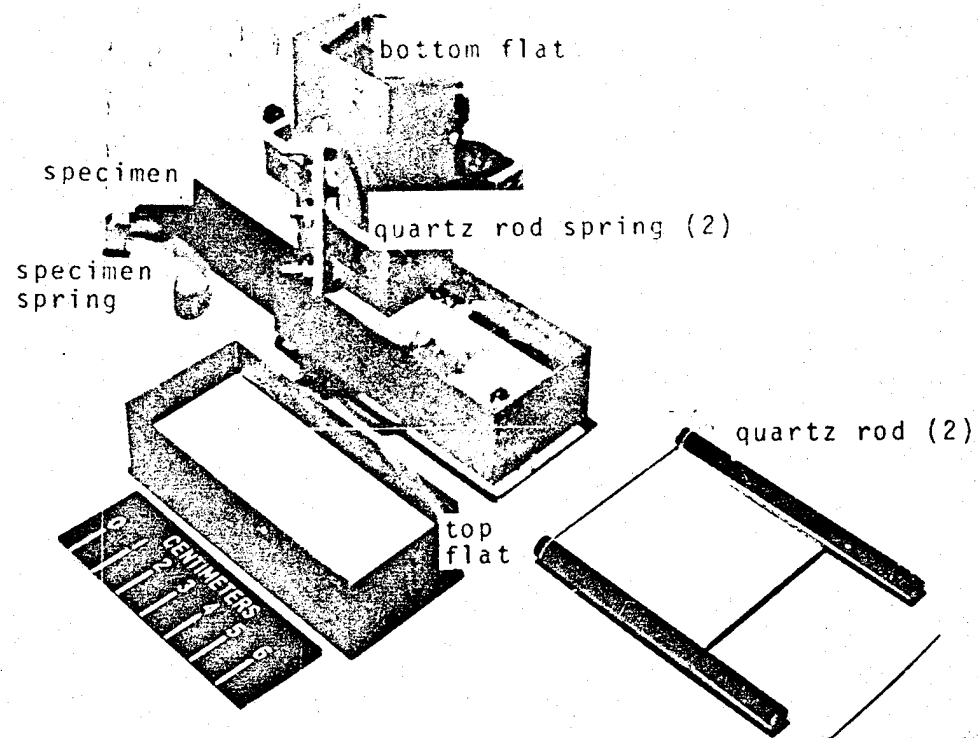
Fig. 2.6 Disassembled Priest Interferometer
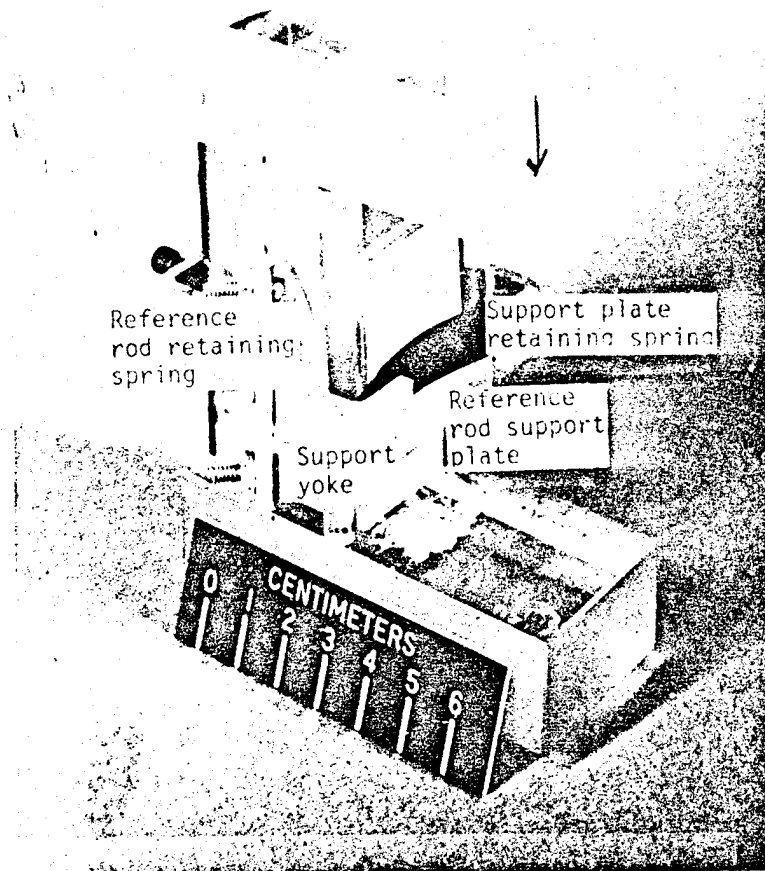
Fig. 2.7 Assembled Priest Interferometer

Previous studies on thermal expansion had been conducted at
Virginia Tech using a unitized-construction Fizeau interferometer. The
components and geometry of this interferometer had all the attributes
needed to construct a Priest interferometer, including a small gap be-
tween the top and bottom flats. All three pieces of this particular in-
terferometer were made of Corning ultra-low expansion titanium silicate
glass. This interferometer, shown in Fig. 2.8, consisted of three
pieces of ultra-low expansion glass held together by optical contact.
An optical contact is generated in the same manner as the contact be-
tween two highly polished steel gage blocks. In the unitized interfer-
ometer the expansivity characteristics of the center piece were being
studied. The end pieces served as optical flats.

To utilize the components of this interferometer, the top end piece
was removed, exposing an optically flat surface. This is shown in Fig.
2.8. This surface was to serve as the bottom optical flat in the
schematics of Figs. 2.2 and 2.3. The upper end piece would serve as the
top optical flat of those figures. What was the central piece of the
unitized interferometer could now be thought of as a pedestal. The ped-
estal would serve as a support for the reference and the specimen. The
lower end piece would serve as a stable base for the Priest interferom-
eter. Using the upper end piece of the unitized interferometer resulted
in a top optical flat that was physically much larger than it needed to
be. Use of this piece was strictly a convenience and its oversize dim-
ensions did not detract from the operation of the interferometer. An-
other feature of the top flat which made it convenient was a slight lack

rays interfere

end piece

optical
contacts

center
piece

end piece

(a)

optically flat.

(b)
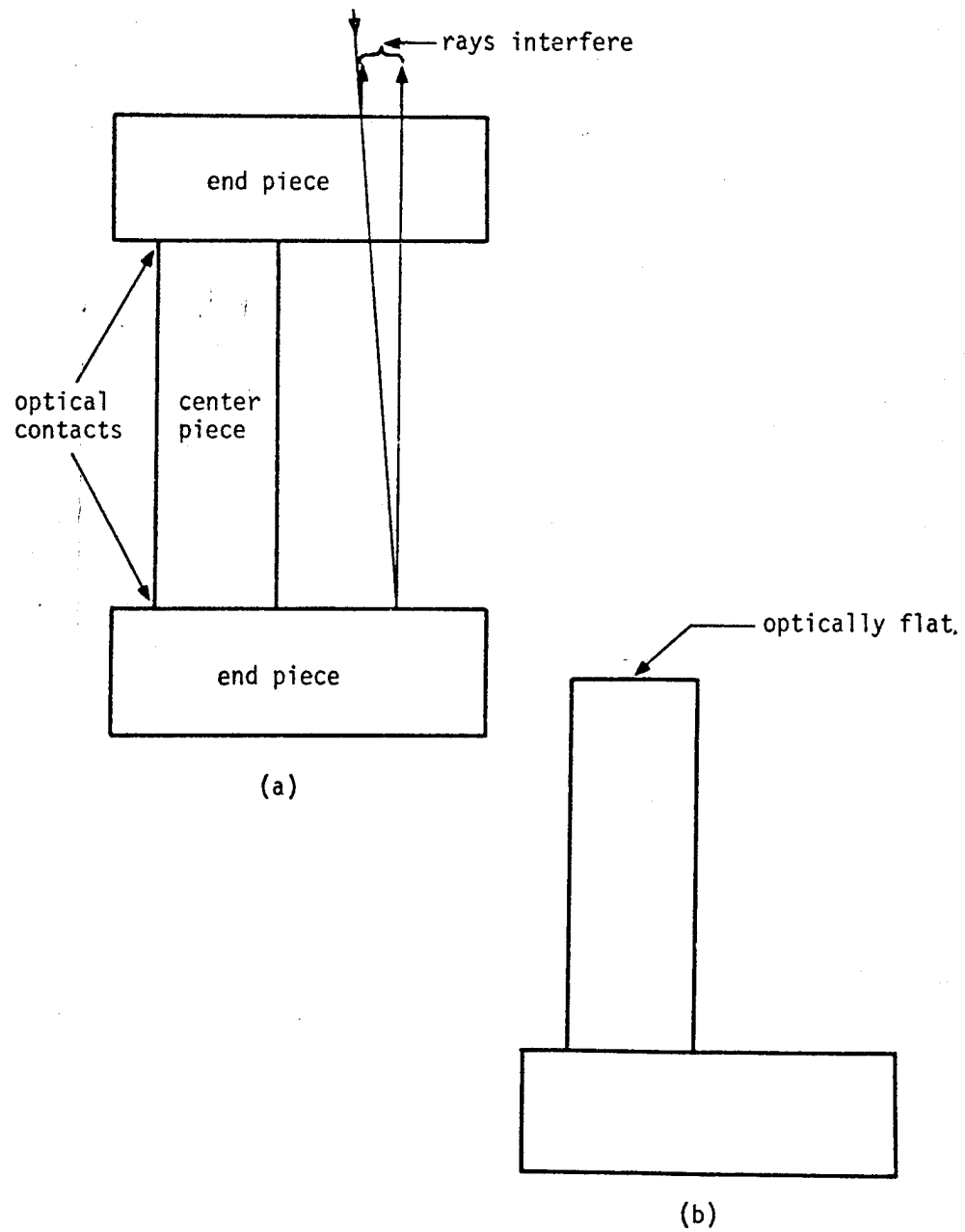
Fig. 2.8 (a) Unitized-Construction Fizeau Interferometer
         (b) Interferometer with One Flat Removed

of parallelism between the top and bottom surfaces of the top flat.
This small misalignment, which caused the light reflected from the top
of the top flat to be deflected away from the interfering beams for the
unitized interferometer, served exactly the same purpose for the Priest
interferometer.

2.4.3 Reference Rods

Since the pedestal was 76.2 mm (3.00 in.) long and since it was de-
sirable to keep the air gap small, the specimen and reference rods were
restricted to be only slightly longer than 76.2 mm (3.00 in.). Other
requirements for the reference rods were that they have expansivity
characteristics roughly the same as the specimen being studied. In ad-
dition, it was necessary to have reliable information about of their
thermal expansion behavior. The National Bureau of Standards standard
reference material denoted as SRM 739, fused silica, was selected for
the present application. Its thermal expansion characteristics were on
the order of $[0/45/-45/90]_s$ specimens being tested. SRM 739, as ob-
tained from the National Bureau of Standards, is a 102 mm long x 6.35 mm
in diameter (4 x 0.25 in.) right circular cylindrical rod of commercial-
ly pure fused silica. The axial thermal expansion behavior of SRM 739
has been determined by the Bureau and their findings are reported in
[9].

In the experimental set-up being designed, two reference rods were
needed. These rods had to be the same length to within a fraction of a
wavelength of the light being used. Since the rod length available from

the Bureau was 102 mm, the rods had to be shortened to match the 76.2 mm (3.00 in.) pedestal if the air gap was to be small. In addition, both rods had to be shortened the same amount. More importantly there was the question of point contact, which has been shown schematically in all the figures, between the top flat and the reference rods. A point contact is necessary to be able to accurately determine L_g and L_0 for use in Eqn. 2.17. In most engineering materials, points are quite fragile, can blunt easily, or even break off. For optical work the concern is the point blunting by even a few wavelengths or, in the case of glass, chipping an imperceptibly small amount. The requirements of having the rods the same length and also having a point contact led to the following scheme for shortening the rods.

Instead of establishing contact with the rods on the centerline of the rod cross-section, contact was established on the outer edge. Thus instead of using a cone-shaped end on the rods, which would result in a sharp central point, the rod ends were beveled. This bevel was extremely small, 30 minutes ± 10 minutes. From a machining point of view, this beveling was a much simpler operation than making a cone. With the bevel, one was assured the contact point was exactly at the outside edge. Machining a cone on the end would require extreme accuracy to assure the apex was coincident with the centerline of the rod.

Another idea was incorporated into the rod machining operation. Two rods were all that were needed for the interferometer. However, if one rod was inadvertently chipped or in any other way damaged to the extent that its length changed by even a few wavelengths of light, the in-

terferometer would have been difficult to use. Working around other pieces of glass, around steel, and moving in an out of the environmental chamber with rods could well produce a situation where a rod was hit against something and chipped. Thus spare rods were made. Specifically, 6 rods were machined at one time. This was accomplished by rough-cutting the 102 mm rods to something slightly greater than 76 mm. The 6 rods were then bonded together in a cluster by potting them in an epoxy-powdered glass slurry. This is shown in Fig. 2.9. The potted rods and the epoxy were then polished on each end until the desired length and bevel were achieved. By polishing each end of the potted assembly to be flat over the 6-rod surface area to within a fraction of a wavelength, equal lengths of the rods were assured to with the tolerances needed. To aid in setting up the interferometer, the low side of the bevel was identified on the rods. The machining of the rods was performed by Planar Optics of Webster, NY.

2.4.4 Specimens

Two specimen sizes were used in this work, all of the same shape. Figure 2.10 shows the basic specimen shape. The composite specimens were all made from 8 plys of T300/5208 graphite-epoxy in a quasi-isotropic configuration, specifically $[0/45/-45/90]_s$, with the exception of specimen 7 which had a $[0]_8$ layup. According to C-scans of the original panels, the batch of material from which these specimens were cut was essentially void free.
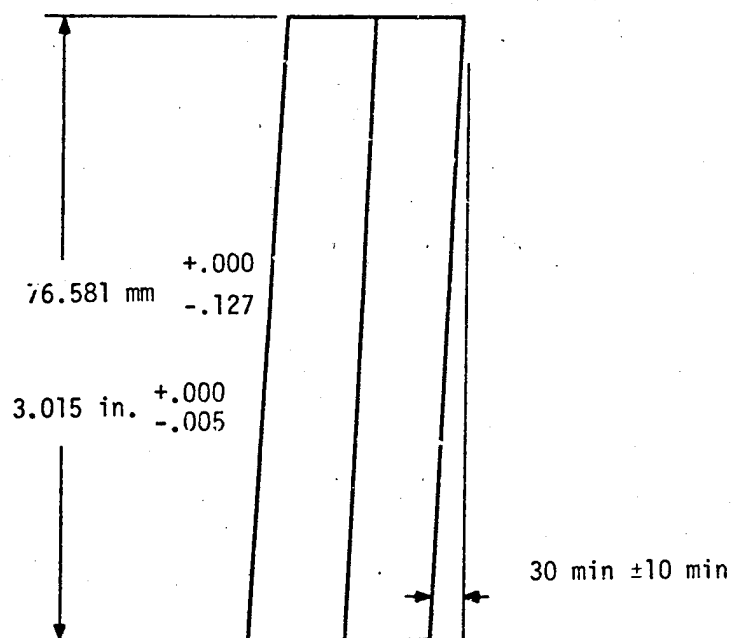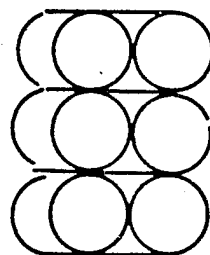
Fig. 2.9 Quartz Rod Polishing Configuration

The specimen length was specified so that the specimens, as machined, would be 0.05 to 0.10 mm (0.002 - 0.004 in.) longer than the quartz rods. This allowed manual sanding of the specimen ends in order to achieve an initial specimen length which provided the optimal initial fringe pattern. This sanding procedure is further discussed in Chapter 3 when describing interferometer alignment procedures.

Specimen ends were machined with the radius shown in order to provide point contact between the specimen and top optical flat. Although the specimen ends were flat in the thickness direction after machining, point contact was achieved as a result of the previously mentioned sanding operation.

2.5 Other Components

Remaining interferometer components were non-critical in the sense that they had no strict thermal response or dimensional requirements. These components (Figs. 2.6,7) consisted of the support yoke, specimen restraining spring, reference rod restraining spring, reference rod support plate, and support plate retaining spring. The retaining springs were formed of 0.127 mm (0.005 in.) spring steel and the yoke itself was formed from 1.59 x 12.7 mm (0.0625 x 0.5 in.) aluminum bar stock. The springs and the yoke were hand-formed. The primary purpose of the yoke and retainer spring system was to provide lateral support for the two reference rods and the specimen. The yoke-spring system was located about half way up the pedestal. The yoke was fastened to the pedestal with RTV silicone rubber. There was a subtle feature to supporting the
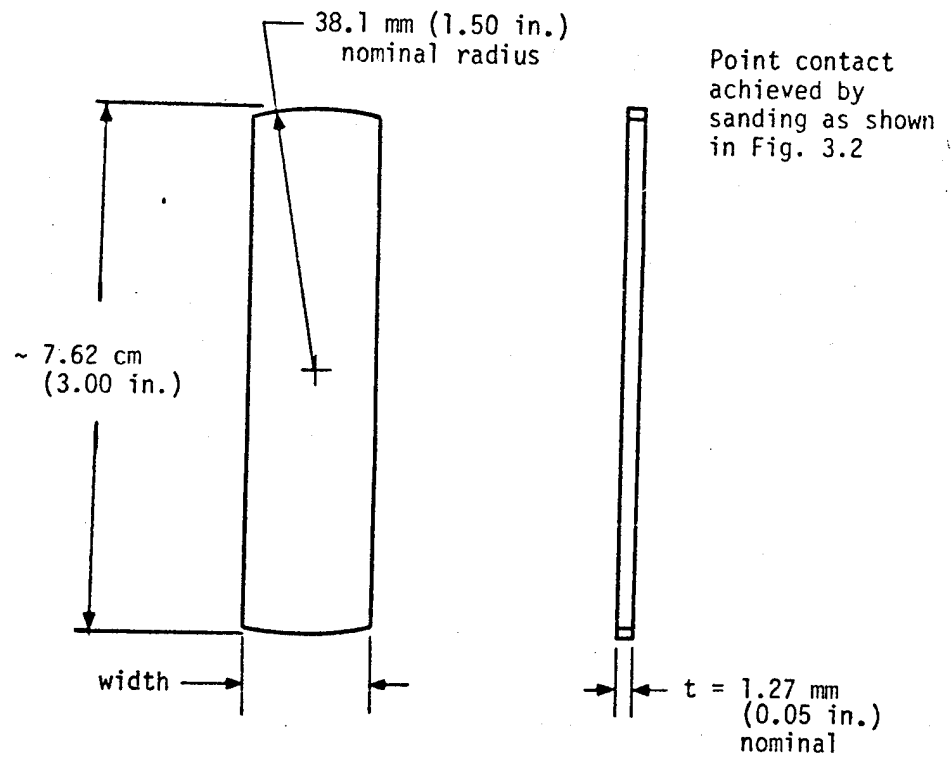
Fig. 2.10 Specimen Geometry

reference rods with the spring system. A glass plate wider than the pedestal, was held against the pedestal with a spring. This plate was on the side of the pedestal opposite the specimen. Each reference rod was held, by other springs, in the corner formed by the reference rod support plate and the pedestal. Thus the reference rods were forced into a corner to minimize any lateral movement. Figure 2.11 shows the direction of the forces provided by the various springs.

2.6 Assembly

All that is required to insert a test specimen is to slide the specimen between the spring and the pedestal and put the top flat in place. After some alignment procedures to be discussed in Chapter 3, illuminating the top flat with a collimated beam of coherent light produces the fringe pattern. The optical components involved in producing the collimated beam will now be discussed.

2.7 Optical Track

The collimated beam is provided by means of the optical track. Ultimately, this optical track focuses the interference pattern on the film plane of the camera used to record fringe images. This optical track is shown schematically in Fig. 2.12. The key elements are the collimating lens, partial mirror, and focusing lens.

The cabinet or shelf-type optical bench, visible as the metal framework in Fig. 2.5, consisted of a top and bottom shelf which allowed for a very compact vertical arrangement of these optical elements. The
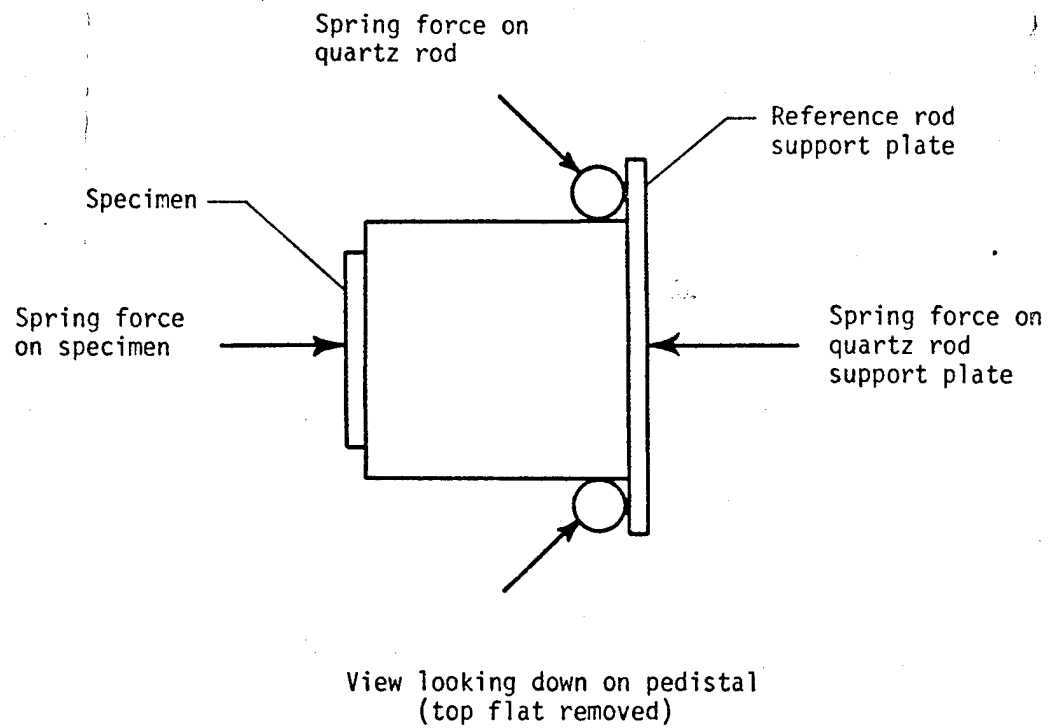
Fig. 2.11   Spring Force on Specimen
            and Reference Rods

only additional requirement for this arrangement was to have a mirror on the top shelf to turn the light vertically from the horizontally mounted laser. This mirror could be thought of as a vertical light source. The optical path from laser to camera is traced below.

2.7.1 Top Shelf

The light source is a Spectra Physics Model 155 He-Ne laser. Light emerges from this source as a coherent, collimated beam about 6.35 mm (0.25 in.) in diameter. Since a wider beam is desired, a beam expander--actually a 40x microscope objective--is placed in the path to diffuse the beam. The last element on the top shelf is an adjustable mirror which turns the beam through approximately 90°, from horizontal to vertical. The top shelf, a 9.53 mm (0.375 in.) thick aluminum plate, has a 63.5 mm (2.50 in.) diameter hole through which passes the diverging beam.

2.7.2 Bottom Shelf

The beam next passes through a 50% partially reflecting mirror oriented at a 45° angle relative to the vertical. By passing through this partial-mirror the beam intensity is cut in half. The other half of the beam is reflected away from the optical path. At this point the still-diverging beam passes through a hole in the bottom shelf in which is located a 63.5 mm (2.50 in.) diameter, 330 mm (13.0 in.) focal length collimating lens.

Full
Mirror

Objective
Lens

Laser Source

Focusing
Lens

35 mm
Camera

Partial Mirror

Collimating Lens

Oven Window
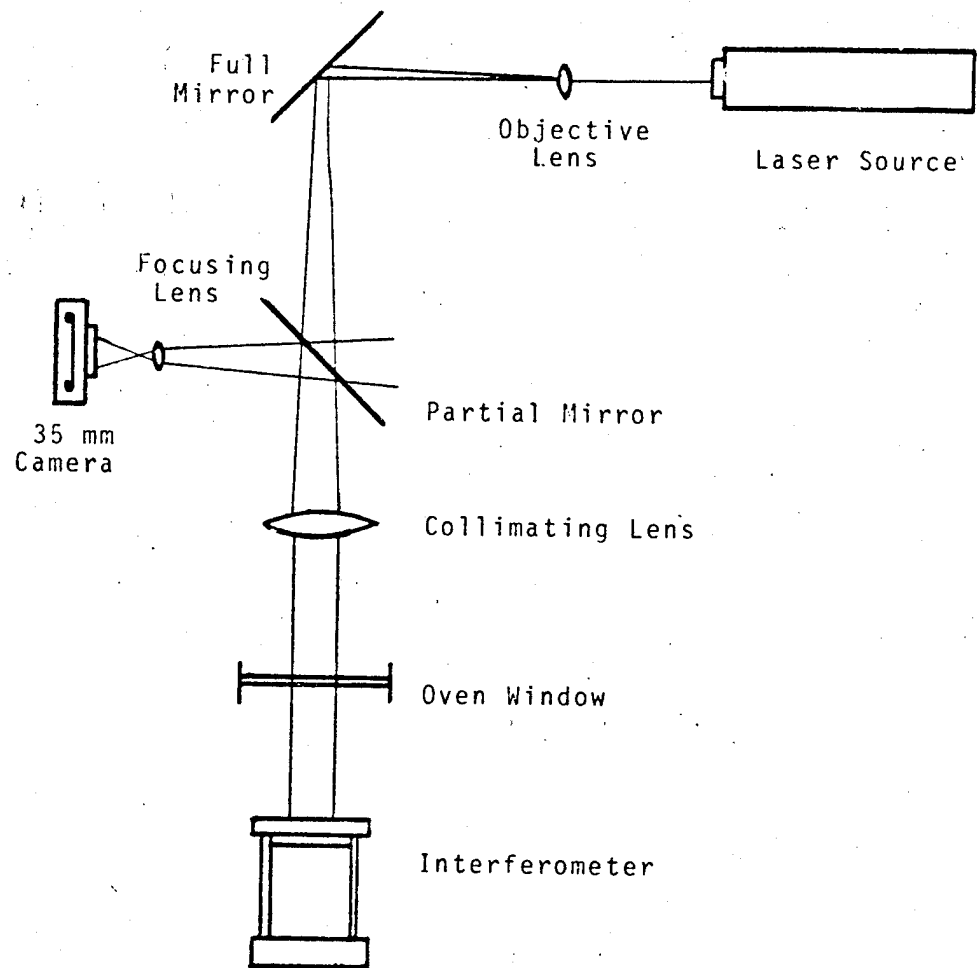
Interferometer

Fig. 2.12 Optical Track

The now-collimated beam passes through a window in the top of the oven, reflects from the top and bottom flats of the interferometer and returns to the collimating lens. The beam, now carrying the fringe pattern created by the interferometer, is converged somewhat by the collimating lens as it returns through the bottom shelf. Upon contact with the partial mirror the beam is again divided and half of the beam is reflected to a camera while the rest passes through the mirror and back to the source.

The return beam reflected from the 50% mirror next passes through a focusing lens. This 152 mm (6.00 in.) focal length lens is not needed to focus the fringes themselves--they can be viewed in any plane. However, it is important to be able to locate the edges of the fringe field precisely to determine L_g for use in Eqn. 2.17. Thus the camera is focused at reference marks on the bottom flat of the interferometer. The final element on the bottom shelf is a 35 mm camera used to record the focused fringe image.

The portion of the returning beam transmitted through the partial mirror back to the source is also quite important. It is used to perform alignment checks. Alignment is discussed in Chapter 3.

2.8 Environmental Chamber

The environmental chamber consisted on an Applied Test Systems Series 2911 test chamber fitted with a liquid nitrogen supply. The nitrogen supply was controlled by an on-off solenoid valve. The chamber was heated with conventional resistance heating elements. This arrange-

ment was capable of achieving and holding the chamber at any temperature between 116 to 366K, ± 2K (-250 to 200°F, ± 3°F). The chamber was fitted with triple pane windows on its top and two sides. Through a hole in the bottom of the chamber passed a stand on which the interferometer was set. This stand was fitted with a base having an adjustable three-point support. Using two adjustable screws, visible in Fig. 2.5, the stand and interferometer could be tilted slightly away from vertical in any direction. This adjustment was used during interferometer alignment as discussed in the next chapter.

The chamber was not evacuated during testing. Instead a small tube in the bottom of the oven was used to bleed N_2 gas into the oven. This gas flow maintained a slight over-pressure during testing to prevent entry of humid air into the chamber.

Chapter 3

EXPERIMENTAL PROGRAM

3.1 Test Program

3.1.1 Purpose of Tests

The test program described in this section had four basic
objectives:

i)   develop a test procedure;

ii) establish the range and resolution of the Priest Interferometer
     described in Chapter 2;

iii) measure the thermal expansion of 8-ply quasi-isotropic Gr/Ep
     between 116 and 366K (-250 and 200°F); and

iv) assess the effect of specimen width on thermal expansion of
     quasi-isotropic Gr/Ep.

The purpose behind each of these objectives is briefly discussed
below.

Development of Test Procedure

Prior to testing, the Priest Interferometer was untried as a device
for measuring thermal expansion of composites. Also, very little infor-
mation was available concerning problems associated with measuring ther-
mal expansion of composites at low temperatures. In order to overcome
these difficulties prior to the testing of Gr/Ep, a series of prelimin-
ary tests were conducted.

41

Range and Resolution

Every measuring device has limits. Each device possesses a limited range over which reliable measurements can be made and a minimum change in the measured quantity which can be reliably detected. These characteristics of range and resolution must be established if out-of-range or falsely precise measurements are to be avoided.

Thermal Expansion of Quasi-Isotropic Gr/Ep

Chapter 1 gave the main reasons for measuring the thermal expansion Gr/Ep. Not mentioned there was the fact that, as a first step, "baseline" thermal expansion data is needed in order to assess the effects of other environmental factors, i.e., moisture and radiation, on dimensional stability. Thus, the data collected here should be useful as an experimental control against which environmental effects on thermal expansion of Gr/Ep may be assessed.

Specimen Width Effect

There were two reasons for investigating specimen width effect on thermal expansion. First, a simple comparison study of the type discussed above was needed to assess the feasibility of the approach. Width effect was chosen as a relatively simple comparison study since no special treatment of specimens, other than machining, was required.

Secondly, thermal expansion of composites is often measured using dilatometers which require specimens 6.35 mm (0.25 in.) wide [5] whereas elastic constants are often determined from mechanical tests on 25.4 mm

(1 in.) wide coupon specimens. Thus, differences in thermal expansion results in Gr/Ep due to the width of the specimen must be known if such a dilatometer is to be used in characterizing the material properties of a standard coupon specimen.

3.1.2 Test Plan

Table 3.1 lists the thermal expansion tests which were conducted to achieve the above objectives. The first tests were preliminary in nature and were used to develop a test procedure. These tests were conducted using a 25.4 x 76.2 mm (1.00 x 3.00 in.) specimen made from a 1.0 mm (0.039 in.) thick piece of commercially pure molybdenum. The molybdenum specimen was selected for use since its C.T.E. (thermal expansion coefficient) was close to the thermal expansion values of the quasi-isotropic Gr/Ep to be measured, because the material was readily available, and because of the molybdenum's highly isotropic and stable thermal expansion behavior.

Tests were run using this specimen to assess the effect of specimen mounting, optical track alignment, and heating and cooling rate on thermal expansion measurements. These tests were continued until a test procedure yielding repeatable results for the molybdenum specimen had been developed. This procedure is discussed in Sec. 3.2.

The last three valid molybdenum tests (several tests in between were invalid because of procedural problems) were considered along with three tests on a 25.4 x 76.2 mm (1.00 x 3.00 in.) $[0_8]$ Gr/Ep specimen as

TABLE 3.1

Test Matrix

	Specimen	# Tests	Width, mm (in.)	Comments
[0/45/-45/90]$_s$	1	3	25.4 (1.00)	
[0/45/-45/90]$_s$	2	6	25.4 (1.00)	tested twice as much as others
[0/45/-45/90]$_s$	3	3	25.4 (1.00)	lots of scatter
[0/45/-45/90]$_s$	4	3	25.4 (1.00)	
[0/45/-45/90]$_s$	5	3	6.35 (0.25)	
[0/45/-45/90]$_s$	6	4	6.35 (0.25)	strange low temperature behavior called for fourth test
[0/45/-45/90]$_s$	8	3	6.35 (0.25)	
[0]$_8$	7	3	25.4 (1.00)	
Molybdenum		3†	25.4 (1.00)	
		28		

† A large number of Moly runs, not discussed herein, were made during development of the experimental procedure.

defining the range and resolution of the measuring device. As discussed in the next chapter, results of these tests showed that the range of the device could be as small as 30 $\mu\epsilon$ or as large as 1700 $\mu\epsilon$, full scale, while the resolution was on the order of 2 $\mu\epsilon$. The upper bound on the range was established with the molybdenum tests, and the lower bound with the [0_8] results. Resolution was assesed by considering scatter in the thermal expansion data for all tests.

The last two objectives of the test program were met by testing seven quasi-isotropic Gr/Ep specimens--three 6.35 mm (0.25 in.) wide and four 25.4 mm (1.00 in.) wide--for a total of 25 tests. The original plan was to test three specimens of each width, three times each, for a total of 18 tests. However, several anomalies in the results--discussed in the next chapter--prompted the decisions to test a fourth 6.35 mm wide specimen, run three extra tests on specimen #2 and add a fourth test for specimen #6. Thus (when the smoke had cleared), 25 tests of quasi-isotropic Gr/Ep specimens were conducted. This fairly large number of tests was conducted so that variations in thermal expansion could be assessed:

   i)   between successive thermal cycles for an individual specimen;

  ii)   between specimens of the same width; and

 iii)   between groups of specimens having different widths.

The results of these tests and the comparisons listed above are given in chapter 4.

3.2 Test Procedure

3.2.1 Preparation for Testing

Interferometer

Before each series of tests on a specimen, all glass interferometer components were disassembled and cleaned by dusting and polishing all non-optical surfaces with lens paper. This cleaning was an attempt to reduce fringe rotation problems (see Sect. 3.3). After cleaning, the interferometer was reassembled with special care being taken to make sure the quartz rods were securely seated with no pivot points of dust or grit between them and their supporting surfaces.

Specimen

As noted in Fig. 2.10, preparation of the specimen consisted of sanding the specimen ends to provide a contact point on each end and to adjust the specimen initial length. The length was sanded so as to provide a reasonable number of fringes at room temperature. This reasonable number was chosen to be roughly the midpoint between the number of fringes obtained at 116 and 366K (-250 and 200°F). This length was achieved by sanding the specimen ends slightly and putting the specimen in the interferometer to check the number of fringes; removing the specimen from the interferometer, sanding the ends; putting the specimen back into the interferometer, etc. The process was continued until the specimen was a suitable length.

Next, two thermocouples were fastened to the specimen--now mounted on the interferometer in the oven--using RTV Silicon Rubber. The ther-

mocouples were located on the specimen longitudinal axis about 6.35 mm (0.25 in.) from the specimen ends.

3.2.2 Conducting a Test

Drying

All Gr/Ep specimens were stored in a dessicator prior to testing for a period exceeding two weeks. Calculations presented in Appendix A indicate that this length of time was sufficient to render the specimens substantially free of moisture. However, due to atmospheric exposure during preparation for testing, some moisture absorption by the specimens was assumed. In order to drive out this moisture and ensure that all specimens were tested in an essentially moisture-free state, all Gr/Ep specimens were exposed to an 18-hour 394°K (250°F) thermal soak prior to each series of three tests. During the thermal soak and subsequent testing, dry nitrogen was bled into the oven at a rate of 0.08 - 0.14 m³/hr (3-5 ft³/hr) to create a slight overpressure and prevent moist ambient air from entering the oven. The effect of moisture on the specimens tested is discussed in more detail in Appendix A.

Alignment and Focusing

Three adjustments to the components of the optical track were required prior to testing. Coarse and fine alignment adjustments were made to ensure that a constant optical path length could be maintained throughout the test and focusing of the camera on the bottom optical flat was performed to ensure that the gage length across which fringes

were counted was sharply defined. After alignment had been completed,
focusing was accomplished by simply moving the camera body back and
forth with respect to the focusing lens until the clearest focus on the
edges of the bottom optical flat was obtained. Alignment of the optical
track is discussed below.

In Fig. 3.1, the distance between points A and B along a ray of
light is called the optical path length (OPL) between points A and B.
The incident rays 1 and 2 each have a different OPL, since $\theta_1 \neq \theta_2$,
even though d is the same for both rays. Thus, changes in the angle of
the collimated beam incident on the top flat, due to, say, thermal ex-
pansion of the interferometer support, will cause changes in the OPL
which are unrelated to thermal expansion of the specimen. Since the
number of fringes in a fringe pattern depends on the number of wave-
lengths or the OPL between flats, such spurious changes in OPL are unde-
sirable. The purpose of optical track alignment is to maintain a con-
stant value for θ throughout the test, removing the possibility of ap-
parent changes in OPL discussed above. For these tests, it was decided
to use the minimum OPL, corresponding to normal incidence ($\theta = 0$), as
the reference OPL.

Coarse Adjustment

1. Remove collimating lens and beam expander from optical path.

2. Put a 63.5 mm (2.5 in.) diameter paper disk (cut from a filing
card is fine) with a pin-hole in the center in place of the collimating
lens.
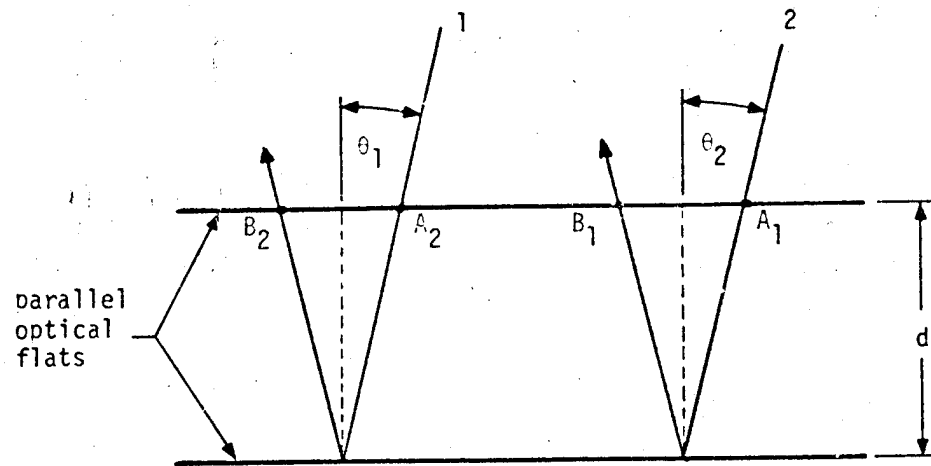
$$OPL_1 = \frac{AB_1}{\lambda} = \frac{2d}{\lambda\cos\theta_1}$$

$$OPL_2 = \frac{AB_2}{\lambda} = \frac{2d}{\lambda\cos\theta_2}$$

Fig. 3.1   Illustration of Optical Path Length

3. Use the adjustable mirror on the top shelf to direct the incident laser beam through the pin-hole and on to the assembled interferometer. Three reflected points of light will be visible on the bottom of the card. One point will reflect from the oven window, one from the top of the top flat, and one from the interference reflection of the top of the bottom flat and bottom of the top flat.

4. Identify the first two reflections mentioned in 3. Tapping the oven window will cause its associated reflection to move while the others stay steady. Tipping the top optical flat slightly will cause the reflections from the top flat to move. One of the points of light will move to reveal a second point "underneath." This is the reflection from the bottom optical flat.

5. Using the adjustment screws on the interferometer support tripod, change the tilt of the interferometer until the interfering optical flat reflections pass through the pin-hole. If there is not sufficient adjustment available, shift the position of the laser slightly and begin again from step 3.

6. Replace the collimating lens and beam expander in the optical path. Orient the beam expander so that the brightest part of the expanded beam is reflected onto the interferometer. Note that for the collimating lens to work properly, the focusing lens of the beam expander must be located at the collimating lens focal point.

Fine Adjustment

After the coarse adjustment procedure has been completed, the fine adjustments to the optical path should be completed. They are:

1. Attach a card with a hole in it to the front of the beam expander. The reflected beam from the top of the top flat should appear on this card near the emerging expanded beam. The beam expander can be placed at the collimating lens focal point (see step 6 above) by moving the beam expander back and forth until the top flat reflected beam is focused on the card. The reflection from the top optical flat will appear on the card above the beam expander only if the top flat is oriented properly. Recall that the top of the top flat is beveled slightly so that its reflection will not be superimposed on the interference pattern.

2. Carefully adjust the tripod adjustment screws until a small adjustment produces no shift in the fringe pattern viewed through the camera either to the left or right. At this point, the angle of incidence is a minimum and alignment is achieved. Note: If coarse alignment has been done well, this step may not be necessary.

3. Mark on the card the location of the reflected point of light. During testing, the optical path is "targeted" by using the tripod adjustment screws to bring the point of light and this "target" mark back into coincidence.

The effect of θ on OPL is directly proportional to the distance between the flats. For the small gap used in this experiment, θ does not need to be maintained constant to a high degree of precision; however,

for larger gaps targeting is essential. In the present work these targeting adjustments were felt to be consistent with good experimental procedure.

Thermal Cycling

Most of the time spent on test procedure development was used to determine the best way to control the environmental chamber during the thermal cycling tests. Several problems were encountered and overcome, specifically:

i) How to minimize the thermal gradient along the length of the specimen during re-heating from 116K (-250°F).

ii) How to prevent the interferometer from accumulating frost as the temperature in the chamber rose towards the freezing point of water.

These problems are discussed in the course of the thermal cycle description given below.

Each thermal cycle consisted of three stages:

i) initial heating - from room temperature to 366K (250°F),

ii) cooling - from 366K to 116K (250°F to -250°F), and

iii) final heating - from 116K (-250°F) to room temperature.

From a normal room temperature value of 298K (75°F), the oven chamber temperature was varied in 28K (50°F) increments. At the end points of the range a temperature increment of 15K (25°F) was used. After each temperature increment was set, a 45 minute soak time was allowed for all components to come to thermal equilibrium. Calculations which support the use of a 45 minute soak time appear in Appendix B. The control settings and soak times used for each part of the cycle are given in Table 3.2. Heating of the specimen and interferometer was accomplished by using a fan to circulate air heated by environmental chamber's heater coils. Cooling took place as pressurized liquid nitrogen was bled into the chamber through a solenoid valve regulated by a chamber-mounted thermocouple. Final heating was accomplished in the same manner as cooling except that the circulating fan--used for both initial heating and cooling--was disconnected.

It was discovered during early test runs that the chamber would warm very rapidly from low temperatures under the influence of the ambient temperature alone. Thus heater coils were not used for final heating. This solved the thermal gradient problem mentioned above, as the oven chamber tended to warm fairly uniformly on its own. However, it warmed at a more rapid rate than 28K (50°F) every 45 min. so that the liquid nitrogen supply was used to control the rate of final heating and provide the required soak time.

A second and particularly troubling point in the final heating procedure was that of interferometer frosting. As the oven warmed, condensation which had frozen onto the unused heater coils during the cooling

Table 3.2

Control Settings and Soak Times

Portion of Cycle	Heater Coils	Circulating Fan	Liquid Nitrogen Solenoid	Hold Time
Initial Heat	on	on	off	45 min
Cool	off	on	on	45 min
Final Heat	off	off	on	45 min

portion of the cycle thawed before the components of the interferometer temperature reached 273K (32°F). With the fan running, this resulted in water vapor being blown onto the interferometer and freezing. This produced a thin layer of frost on all glass components of the interferometer. This problem was solved by simply turning off the circulating fan during final heating.

A peripheral problem which occurred during low temperature operation was frosting of the exterior chamber windows. This necessitated defrosting the top window with a heat gun prior to recording a fringe image on film.

Recording Data

During each test two types of data were recorded--fringe data and temperature data. In addition, for some tests dummy specimens were weighed before the thermal soaking and before and after each cycle. The changing weight of dummy specimens was used to assess the degree of moisture loss which occurred during testing.

Temperature measurement was straightforward. After preliminary tests to determine the steady state temperature distribution in the oven, it was decided that four thermocouples would be sufficient to determine chamber temperatures. Thermocouples were located at the top and bottom of the specimen and one of the quartz rods. Type K thermocouples were selected for use. They were applied to the specimen and quartz rod surfaces using a small bead of RTV silicon rubber.

After running the first six composite tests, use of thermocouples on the quartz rod was discontinued. By this time fringe rotation had begun to be a problem and it was felt that minute shifts in the quartz rod position during thermal cycling, caused by the thermocouples, may have been a contributing factor. Also, results of these early tests showed that the average temperature readings for the specimen and quartz rods were always within $\pm 1K(2^\circ F)$ of each other. This variation was within the calibrated accuracy of the digital thermometer used. Thus, the quartz rods and specimen were assumed to both be at the specimen temperature during subsequent testing.

Fringe data was recorded by taking a 35 mm photo of the interference fringe pattern after the chamber had been at temperature for 45 minutes. The chamber fan was turned off just prior to each photo to minimize thermal currents which sometimes distorted the fringe pattern.

3.3 Data Analysis

3.3.1 Assumptions

Moisture Effects

Moisture effects on composite thermal response were assumed negligible. Based on the results of Appendix A, this assumption appears justified. As pointed out earlier, care was taken to dry all composite specimens prior to testing in an effort to minimize moisture effects.

End Effects

Laminated composite plates, as do most structures, experience free edge or end-effect mechanical behavior. This free edge behavior differs from the mechanical behavior away from the edges. In this work edge effects were assumed to have negligible effect on the thermal strain. This assumption can be briefly justified as follows.

Assume that the composite specimens are prepared as the one shown in an edge view in Fig. 3.2, i.e. a semicircular end preparation has been achieved.

Assume that the two 90° plys in the middle of the specimen will be unrestrained at each end over a distance h, with the remaining material behaving as the bulk specimen. It is easily shown that $h \simeq .1t$ or for $t = .0127$ mm (.005 in.), $h \simeq .00127$ mm (.00005 in.). The thermal strain of this specimen may now be expressed formally as

$$\varepsilon = (\alpha_1 L_1 + \alpha_2 L_2)T/L \qquad (3.1)$$

where: α_1 = coefficient of thermal expansion of a 0° ply

$\simeq 30 \ \mu\varepsilon/K$, [1]

α_2 = coefficient of thermal expansion of the bulk specimen

$\simeq 2 \ \mu\varepsilon/K$, (see App. C results)

L_1 = 2h

L = total specimen length

L_2 = $L - L_1$

T = change in temperature from the reference value.

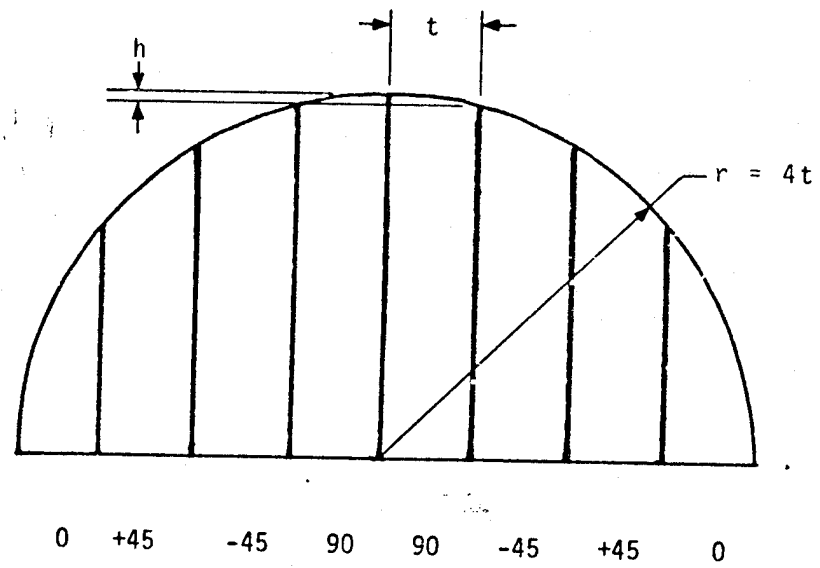Fig. 3.2   Idealized Specimen End View

Based on these numbers, $\alpha_1 L_1 / \alpha_2 L_2 \simeq .0005$, or .05%. Therefore, the first term on the left hand side of eq. (3.1) is considered negligibly small in comparison with the second.

Refractive Index

The index of refraction n is defined as

$$n = \lambda_0 / \lambda \qquad (3.2)$$

where λ depends on the medium thru which the light travels and λ_0 is the wavelength in a vacuum. Using this result in Eqn. 2.17

$$\epsilon_s = \frac{\Delta N \lambda_0}{2 L_0 n} \frac{L_f}{L_g} + \epsilon_r \qquad (3.3)$$

According to [7] the largest change in n which should occur for a test conducted in air between 273 and 394K (32° and 250°F) is .02%. The uncertainty in measuring fringe count ΔN with current methods is ±.5N. Over this temperature range this corresponds to an uncertainty in ΔN of $\sim \pm .5\%$. Referring to Eqn. 3.3 it is obvious that the uncertainty in n will be masked by the uncertainty in ΔN which results from current fringe counting techniques. Thus, until uncertainties in ΔN can be reduced appreciably, uncertainties in ϵ_s due to refractive index are negligibly small and it can be assumed that $\lambda = \lambda_0$.

Difference in Specimen and Quartz Rod Lengths

Equation 2.17 is based on the assumption that the specimen and quartz rods are the same length. In reality these two lengths differ by less than .01%. The effect of this difference on the specimen thermal strain measurement may be assumed negligible when compared to the uncertainty in the quartz rod thermal strain.

3.3.2   Thermal Strain Calculation

Given physical dimensions of the test set-up, the change in number of fringes from room temperature, ΔN, and the quartz rod reference strain, ϵ_r, eqn. 2.17 was used to calculate ϵ_s for each temperature at which data was recorded. The data analysis consisted of three parts:

    i)   fringe data reduction

   ii)   calculation of reference strain

  iii)   presentation of ϵ_s vs. T results

Each will now be discussed in turn.

Fringe Data Reduction

Figure 3.3 shows a typical fringe photo print. Fringe counts were obtained by using an image about twice this size. These images were generated by placing the photo negatives in a microfiche reader. Referring again to Fig. 3.3, two fringe counts were made for each photo; one along the top, called the vertical fringe count, and one down the side

horizontal fringes - counted from top to bottom

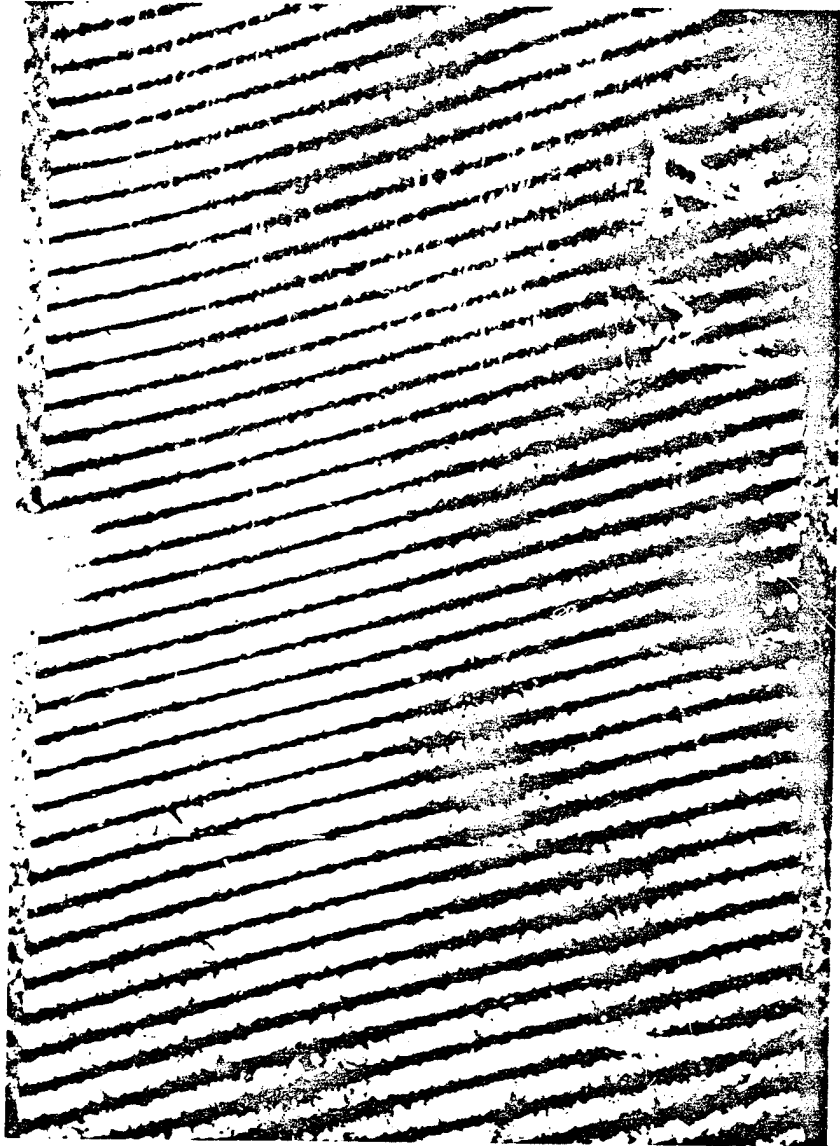vertical fringes - counted from left to right

Fig. 3.3 Typical Fringe Photo Print

called the horizontal fringe count. The vertical fringe count represents the information which the interferometer was designed to produced. Horizontal fringes represent a problem in the interferometer and are discussed in the next section.

Once all fringe counts had been made for a particular thermal cycle the quantity ΔN was obtained for each temperature by subtracting the number of vertical fringes on the initial, room temperature photo from the vertical fringe count at subsequent temperatures.

It should be noted that a negative number of vertical fringes could be obtained at low temperatures. This occurred when the number of vertical fringes decreased to zero on cooling and then began to increase in number with further cooling. Thus, an increasing number of fringes during cooling was considered to be increasingly negative.

Calculating Reference Strain

As discussed in Chapt. 2, the reference material selected for the application was the NBS SRM 739. A table of thermal expansion of the material as a function of temperature is provided by NBS when the quartz rods are purchased. This table is included as figure 3.4

For each test temperature the data appearing in Fig. 3.4 was used to calculate the reference strain based on a reference temperature of 293K. This reference strain was then corrected for the difference between specimen and quartz rod reference temperatures using

$$\epsilon_r = \frac{\Delta L(T)}{L(293)} - \frac{\Delta L(To)}{L(293)} \tag{3.4}$$

Certificate of Analysis

Standard Reference Material 739

Fused-Silica Thermal Expansion

R. K. Kirby and T. A. Hahn

Thermal Expansion as a Function of Temperature

T	Expansion ΔL/L293	Expansivity α	T	Expansion ΔL/L293	Expansivity α
80 K	- 1 × 10⁻⁶	-0.70 × 10⁻⁶/K	320 K	13.₅ × 10⁻⁶	+0.53 × 10⁻⁶/K
90	- 7.₅	-0.61	340	24.₅	0.56
100	-13	-0.53	360	36	0.58
110	-18	-0.46	380	47.₅	0.60
120	-22.₅	-0.38	400	59.₅	0.61
130	-26	-0.31	420	72	0.62
140	-28.₅	-0.24	440	85	0.63
150	-30.₅	-0.17	460	97	0.63
160	-32	-0.10	480	110	0.63
170	-32.₅	-0.04	500	122	0.63
180	-32.₅	+0.02	520	135	0.62
190	-32	0.08	560	159	0.61
200	-31	0.13	600	183	0.59
210	-29.₅	0.19	640	206	0.56
220	-27.₅	0.23	680	228	0.54
230	-25	0.28	720	249	0.51
240	-22	0.32	760	269	0.49
250	-18.₅	0.36	800	288	0.47
260	-14.₅	0.39	840	307	0.44
273	- 9	0.43	880	324	0.42
280	- 6	0.45	920	340	0.40
293	0	0.48	960	356	0.38
298	+ 2.₅	0.49	1000	371	0.37

This SRM is available as a rod 6.4 mm (¼ inch) in diameter: L1 is 51 mm (2 inches) long, L2 is 102 mm (4 inches) long, and L3 is 152 mm (6 inches) long. (Note: Inquiries for longer continuous rods may be directed to the Office of Standard Reference Materials, National Bureau of Standards.) The rods that make up this SRM were obtained as a single drawing from an ingot of fused silica, at least 99.8 wt percent pure. These rods have been annealed by soaking at 1373 K for 7 hours and cooling to 1173 K at 12 K per hour.

The above values of expansion and expansivity were calculated from a least squares fit to expansivity measurements made on five specimens. Linear interpolation can be used between tabulated values without introducing a significant error. The expansion of this material may be altered, however, if the material is heated to temperatures above 1020 K. A description of the experimental method, fitting procedure, and estimate of uncertainties is given on the back of this certificate.

The overall coordination and evaluation of data leading to certification of this SRM was performed by R. K. Kirby and T. A. Hahn.

The technical and support aspects involved in the preparation, certification, and issuance of this Standard Reference Material were coordinated through the Office of Standard Reference Materials by R. E. Michaelis.

Washington, D. C. 20234
May 12, 1971

J. Paul Cali, Chief
Office of Standard Reference Materials

(over)

Fig. 3.4   NBS Data Sheet for SRM 739

Here $\Delta L(T) = L(T) - L(293)$ and T_0 is the specimen reference tempera-
ture. It is assumed that $L(T_0) = L(293)$ so that the second term in Eqn.
3.4 vanishes.

Presentation of ε_s Results

One can find "thermal expansion" data presented in the literature
in a number of ways. However, the fundamental measurement is always one
of dimensional change as a function of temperature. This data may be
converted to thermal expansion coefficients by a number of techniques.

While thermal expansion coefficients may be of interest to design-
ers, actual thermal response is more directly obtained from the raw ex-
perimental data. Chapter 4 presents the thermal strain of the composite
as a function of temperature in the form of the best polynomial least-
squares fit to the data having order three or less. More involved curve
fitting and statistical analysis schemes were considered. However, the
experimental results were reasonably repeatable and resulted an easily
distinguishable quasi-linear trend. Thus, it was felt that these more
elaborate approaches would be of minimal value. A description of the
regression analysis scheme used is included in Appendix C.

3.3.3 Out of Plane Rotation and Horizontal Fringes.

The mathematical model of the Priest interferometer presented in
Chapt. 2 was based on the assumption that all relative motion of the in-
terferometer components could be represented by a model with two degrees

of freedom. One degree of freedom was translation in the plane of figs. 2.2 and 2.3 and the other was rotation about an axis perpendicular to that plane. Due to a problem with the quartz rod support design, this was unfortunately not the case during testing. The following is a discussion of an additional rotational degree of freedom encountered in the system and the approach taken to quantify the uncertainty it introduced into thermal strain measurements.

For the ideal, two degree of freedom Priest interferometer discussed in Chapt. 2 the fringes should all be vertical--hence the name vertical fringes. However, as is readily seen from Fig. 3.3, this was not the case in practice. The deviation of the fringes from a perfectly vertical orientation in this photo is due to an out of plane rotation of the top optical flat. This out of plane rotation produces what will be referred to as horizontal fringes. The superposition of the vertical and horizontal fringe patterns produces the "fringe rotation" apparent in Fig. 3.3. In this figure the number of vertical fringes is much larger than the number of horizontal fringes and so the fringes are 'almost' vertical.

The number of horizontal fringes was very sensitive to the relative position of the two quartz rods used to support the top optical flat. Also, due to what was found to be an unstable quartz rod support scheme the rods' relative position could change during the course of a thermal cycle. This caused changes in the number of horizontal fringes and thus fringe rotation.

Since this problem became evident only after a fairly large number of tests had been run, and since it did not completely invalidate test results, the decision was made not to change the interferometer design for this test program. Several steps were taken to minimize fringe rotation however. These steps were:

i) removal of thermocouples from quartz rods;

ii) cleaning the quartz rods and their supports prior to each test series to remove particles which might prevent positive seating of the rods; and

iii) tapping of the interferometer support prior to each thermal cycle to cause the quartz rods to seat in a stable position.

These measures reduced the fringe rotation problem. However, some uncertainty in the results due to fringe rotation remained. To compound the problem this uncertainty could not be quantified as a systematic error. This is due to the fact that while the maximum magnitude of the uncertainty could be determined from horizontal fringe counts, the direction (apparent increase or decrease in thermal strain) could not.

This situation is illustrated in Fig. 3.5. In (a) the two flats are parallel and the corresponding fringe image (b) shows no fringes--a null field. In (c) the top flat tilts toward the reader so that the rear quartz rod support point moves upward a distance $d = \lambda/2$ and the specimen support point moves vertically upward by a distance $\lambda/4$. This produces one horizontal fringe (d). In (e) the top flat tilts away from

the reader and the rear quartz rod and specimen support points move ver-
tically downward. However, the net result is still one horizontal
fringe (e). Thus, the question arises, "if the interferometer went from
zero to one horizontal fringes, did the specimen move up or down a dis-
tance of $\lambda/4$?" This question asked about a specific situation here can
be asked in general about any two fringe photos which have a different
number of horizontal fringes.

Fringe rotation was most evident during the low temperature portion
of the thermal cycle and never occurred above room temperature. Fur-
thermore, the phenomenon seemed to be reversible so that there were al-
most always the same number of horizontal fringes at the end of a cycle
as at the beginning. This being the case, it was assumed that the un-
certainties due to fringe rotation were not cumulative and a separate
fringe rotation uncertainty was estimated for each data point based on
the following formula (see equation 2.11).

$$U_{\epsilon H} = \pm \frac{|\Delta N_H|\lambda}{2Lo} \, , \qquad (3.5)$$

where $U_{\epsilon H}$ is the maximum uncertainty in the relative strain of the
quartz rods and ΔN_H is the change in number of horizontal fringes from
the beginning of the thermal cycle to any point during the cycle. Eqn.
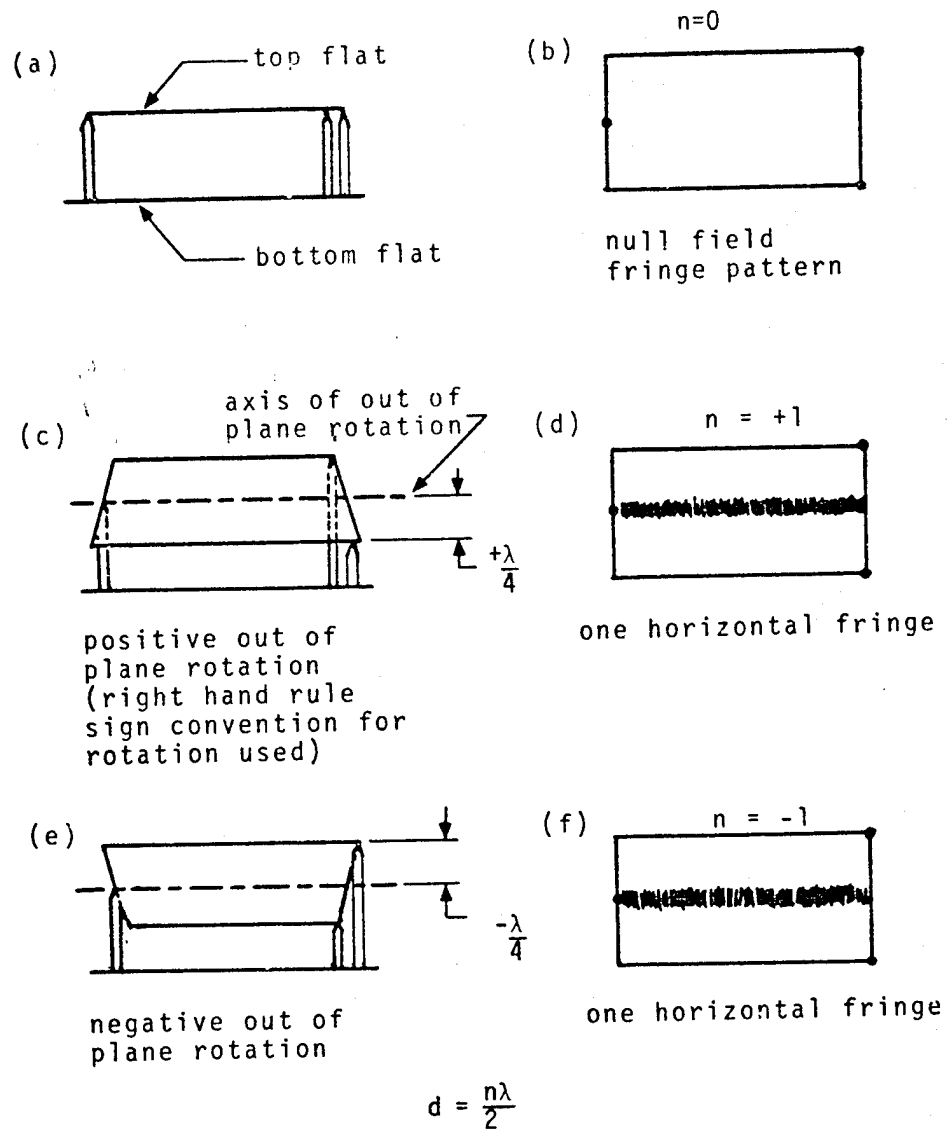3.5 is used to calculate the uncertainty bounds presented in Appendix C.

(a)

top flat

bottom flat

(b)

n=0

null field
fringe pattern

(c)

axis of out of
plane rotation

$+\frac{\lambda}{4}$

positive out of
plane rotation
(right hand rule
sign convention for
rotation used)

(d)

n = +1

one horizontal fringe

(e)

$-\frac{\lambda}{4}$

negative out of
plane rotation

(f)

n = -1

one horizontal fringe

$$d = \frac{n\lambda}{2}$$

Fig. 3.5   Illustration of Horizontal
Fringe Rotation

Chapter 4

EXPERIMENTAL RESULTS

4.1 Introduction

This chapter presents results for the thermal expansion tests list-
ed in Table 3.1. Over 30 tests were performed and in the interest of
conciseness, the detailed thermal expansion results for each test are
not included in this chapter. They are presented in Appendix C. Pre-
sented here is the regression curve for each test. More than one curve
appears on a figure. This reduces the number of figures to be digested
and also facilitates comparison of thermal expansion results for
selected tests.

The test results are presented in chronological order, beginning
with the molybdenum specimen tests which were used to aid in developing
the test procedure. These results are followed by results for 25.4 mm
(1.00 in.) wide and 6.35 mm (0.250 in.) wide $[0/45/-45/90]_s$ Gr/Ep speci-
mens. Finally, results for a wide unidirectional Gr/Ep are presented.

For the molybdenum and all quasi-isotropic Gr/Ep specimens some
comparison of present results to previously reported data is provided.
However, no data was found to allow comparison with the low temperature
results for any of the Gr/Ep specimens.

4.2 Molybdenum Results

A large number of tests using the molybdenum specimen described in
Sect. 3.1.2 were initially conducted in order to develop an experimental
procedure which would yield repeatable results. Results for the seventh

69

tenth and eleventh molybdenum test runs, designated M7, M10 and M11, appear in Fig. 4.1. The low temperature deviation of M10 from M7 and M11 was due to two " spurious" thermal strain readings which occurred during cooling (see Fig. C.3, Appendix C). These data points were the first evidence of a systematic error which was later seen in results for quasi-isotropic specimen number 6. This problem apparently had to do with improper installation of the specimen in the interferometer. Repeated tests after removing and reinstalling the specimen always eliminated the discrepancy.

Figure 4.2 is a comparison of M7 with some typical thermal expansion data for molybdenum [10]. It is interesting to note the slight nonlinearity in the thermal response of the material at low temperature. It was originally thought that this behavior might have been due to a systematic bias in the low temperature performance of the inteferometer. However, as this data corroborates, the slight nonlinearity represents actual material behavior. This confirmation is considered significant since a similar low temperature nonlinearity is also observed for the Gr/Ep specimens discussed next.

4.3 Quasi-Isotropic Gr/Ep Results

The curves presented are referred to below as C1-1, C2-3, etc., where the first digit refers to the composite specimen number and the second to the test number for that specimen. Figure 4.3 presents a comparison of the results obtained above room temperature for 25.4 mm (1.00 in.) wide quasi-isotropic specimens by Brooks [11] with those of
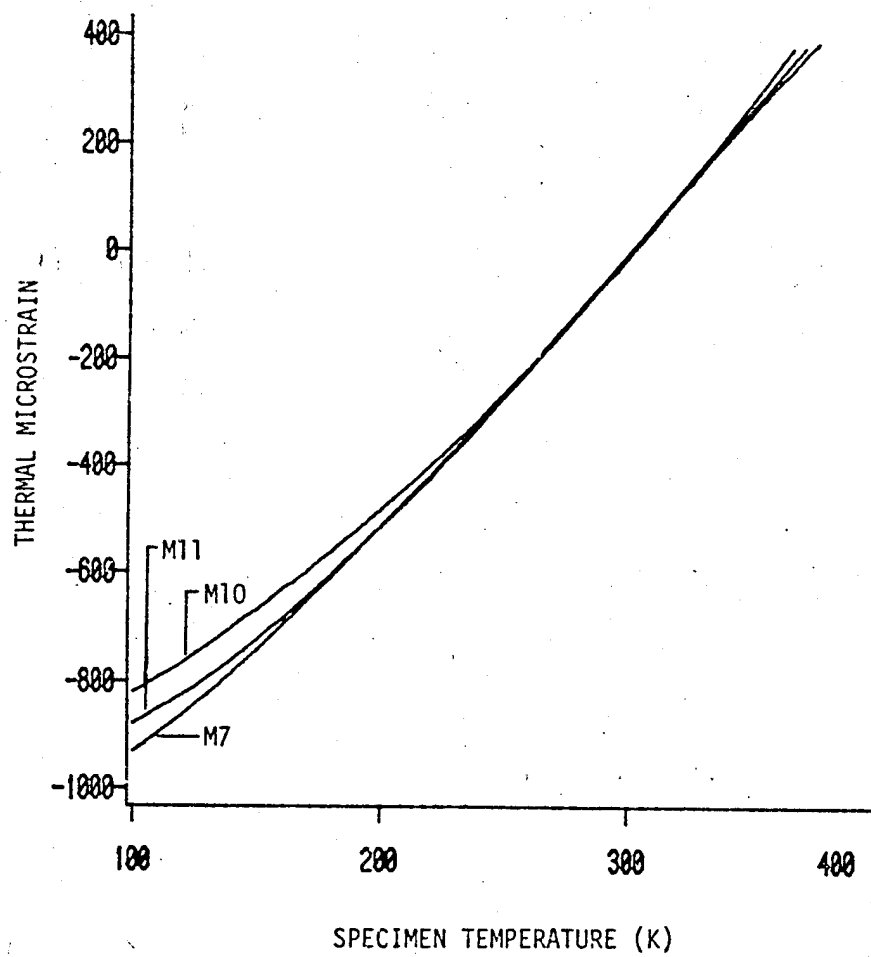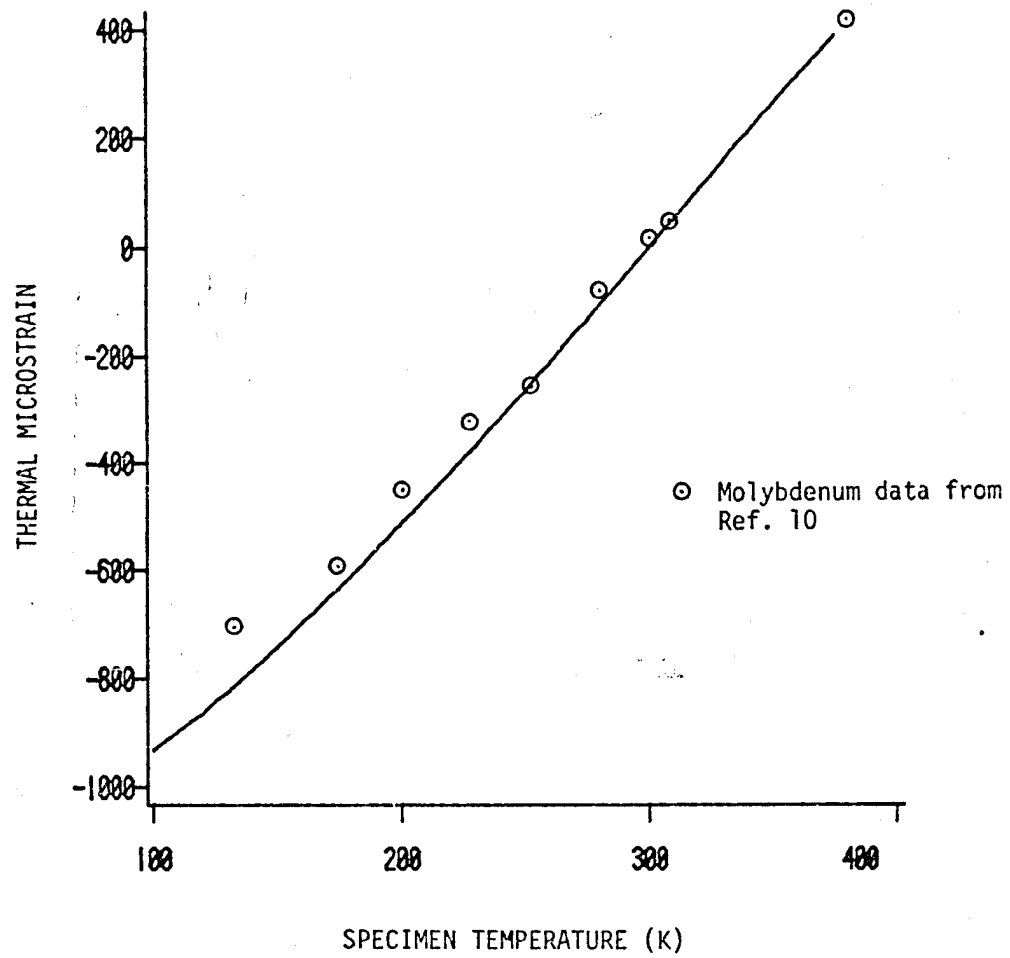
Fig. 4.1
Moly Tests 7, 10, 11

Fig. 4.2
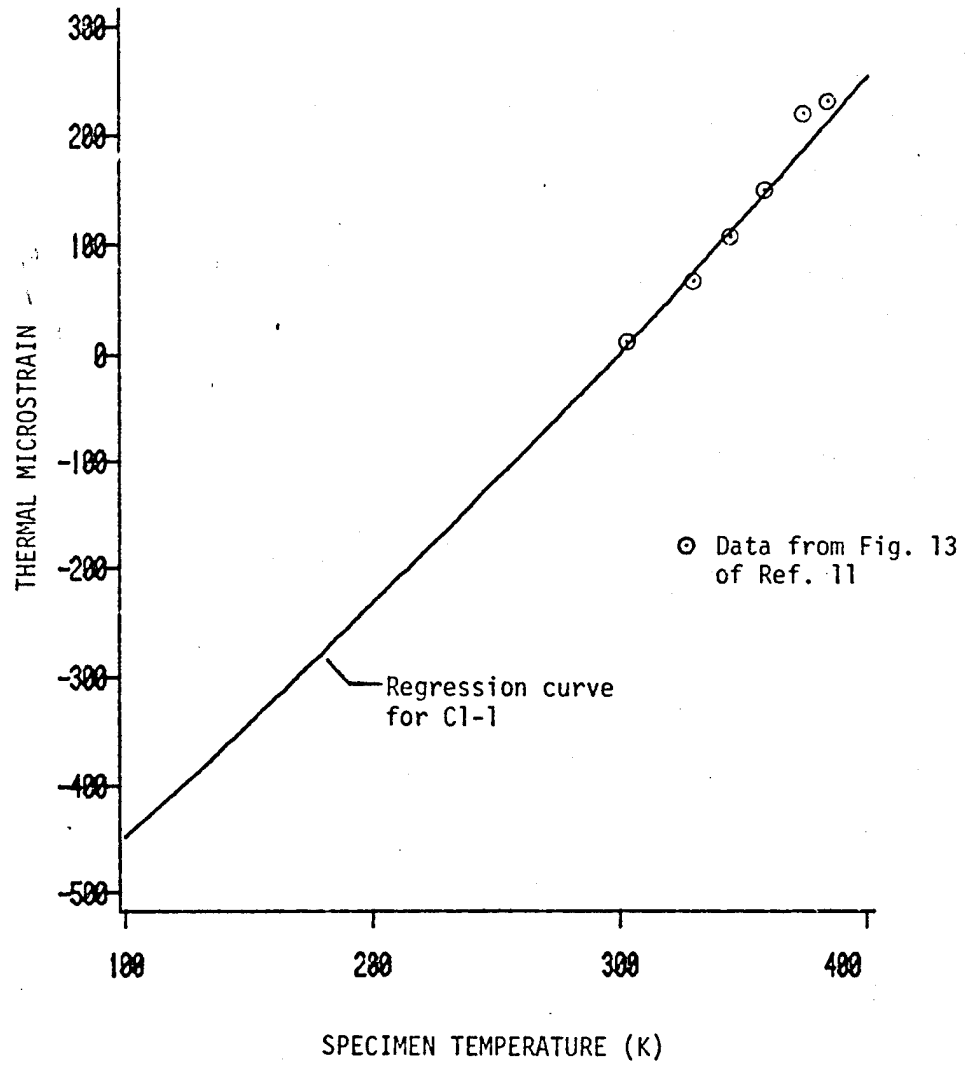Comparison of Moly Run 7 with Results from Ref. 10

Fig. 4.3
Comparison of Cl-1 with Results from Ref. 11

C1-1. This comparison is typical in that all quasi-isotropic results obtained in the present work were similar above room temperature. This similarity is apparent in Figs. 4.4 and 4.5 where all of the 25.4 mm (1.00 in.) wide and 6.35 mm (0.250 in.) wide specimen results are shown. The spread in results at low temperatures can be attributed in part to uncertainty introduced by changes in the number of horiziontal fringes at these temperatures (see Appendix C.). However at elevated temperatures no horizontal fringe changes occurred and the results are more repeatable.

Repeatability of results for several cycles on a specimen is especially interesting. This result indicates, along with the conclusions of Appendix A, that moisture effects in the present test were negligible. The exception is C3-1 shown in Fig. 4.4. The unusual shape of this curve is due to drying of the specimen which took place during the initial heating for cycle 1 on the specimen (see Fig. 13, Appendix C). Another exception here are the curves C6-1 through C6-3 and C8-2. The thermal response of these specimens was completely anomalous at low temperatures and an exhaustive investigation of possible causes of the anomaly lead to the conclusion that it was similar to that reported for M-11. It should be noted that a 4th test on specimen 6 produced no unusual thermal response.

Finally, Fig. 4.6 shows a plot of all quasi-isotropic results. It is apparent from this figure that there are no large difference in thermal expansion behavior caused by the difference in width.
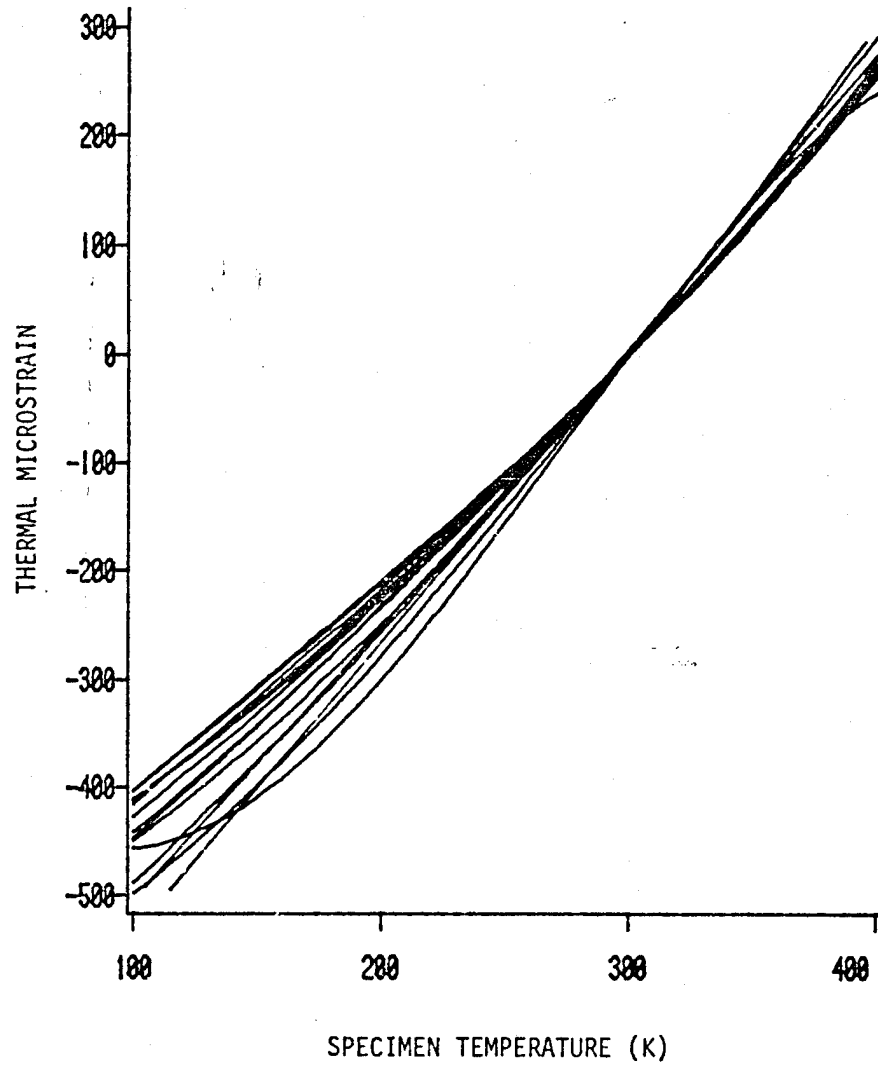
Fig. 4.4
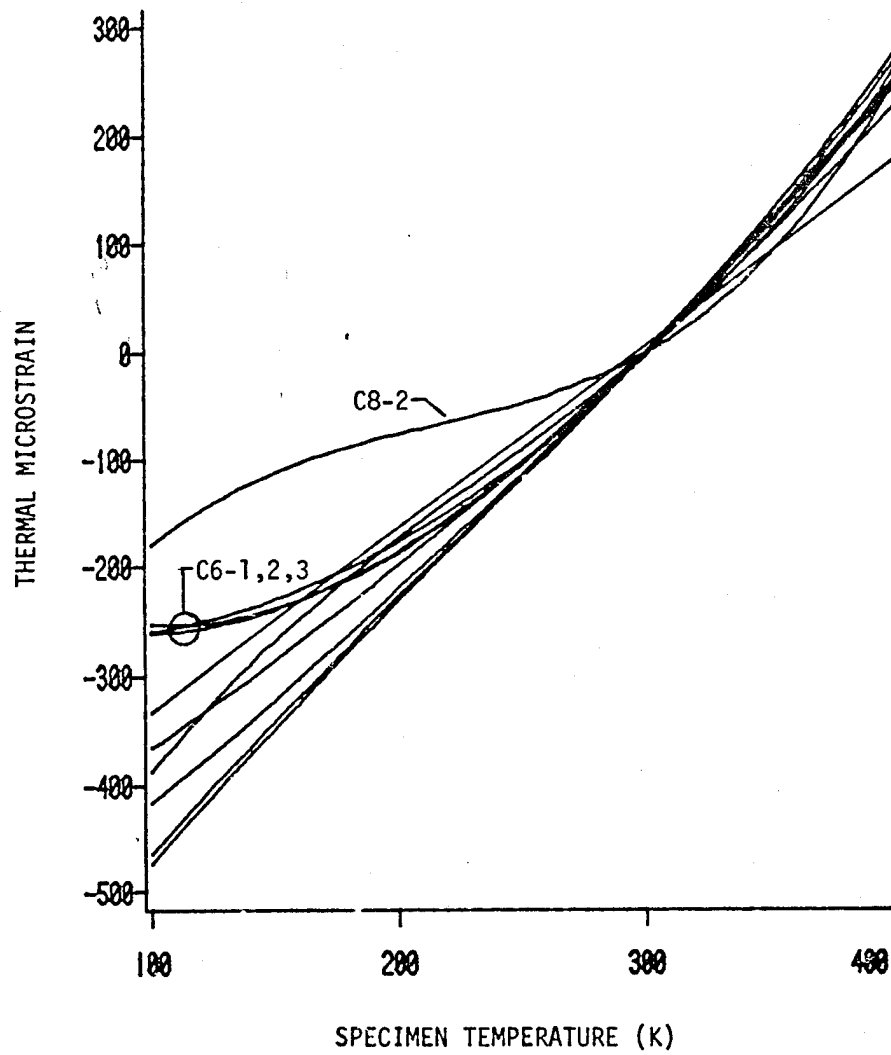25.4mm [0/45/-45/90]$_s$ Specimens - All Tests
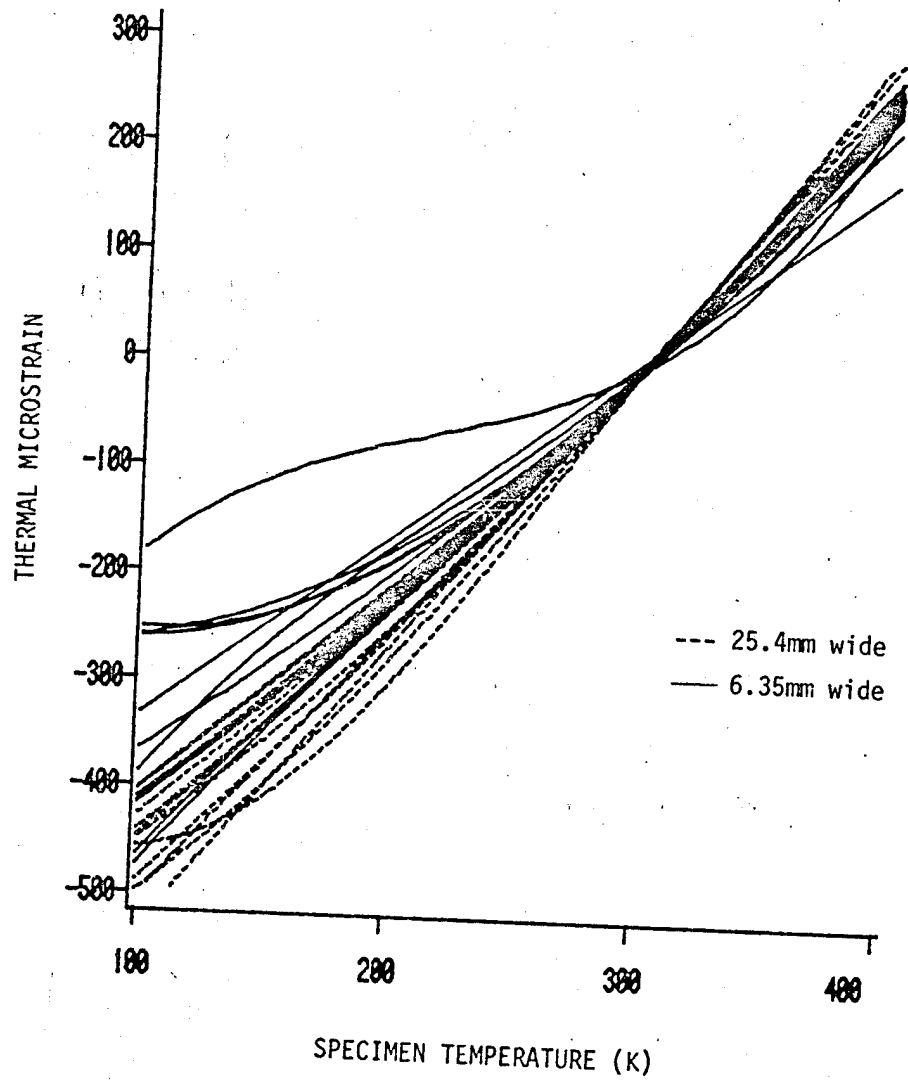
Fig. 4.5
6.35mm $[0/45/-45/90]_s$ Specimens - All Tests

Fig. 4.6
$[0/45/-45/90]_s$ Specimens - All Tests

4.4 Unidirectional Gr/Ep Results

As noted in Chapter 1 unidirectional Gr/Ep exhibits very small thermal strains in the fiber direction. A unidirectional specimen was thus selected to assess the resolution of the Priest interferometer. Figure 4.7 shows results for three tests on a single unidirectional specimen. It should be noted that the procedure described in Sect. 3.4 for quantifying horizontal fringe change uncertainty was not used here. Since apparent strain due to horizontal fringe changes was such a large component of the total strain for this specimen, the direction of the correction could be inferred quite easily by comparing data points with horizontal fringe shifts to those without shifts.

The unusual behavior of the unidirectional specimen below room temperature was completely unexpected. However, the elevated temperature response was expected based on similar results reported by Brooks [11] and Bowles [2]. There is no ready explanation for the highly non-linear response of this specimen below room temperature. All that can be said at this point is that, based on repeated tests and careful checking of the data, it appears to represent actual material behavior. Scatter in the experimental results reported for this specimen in Appendix C is due solely to random error. The horizontal fringe shift error was treated as discussed above. Based on the scatter evident in these figures, along with that observed in the other figures in Appendix C, the current resolution of the Priest interferometer as used in this work is assessed, in a purely qualitative manner, to be about ± 3 µε.
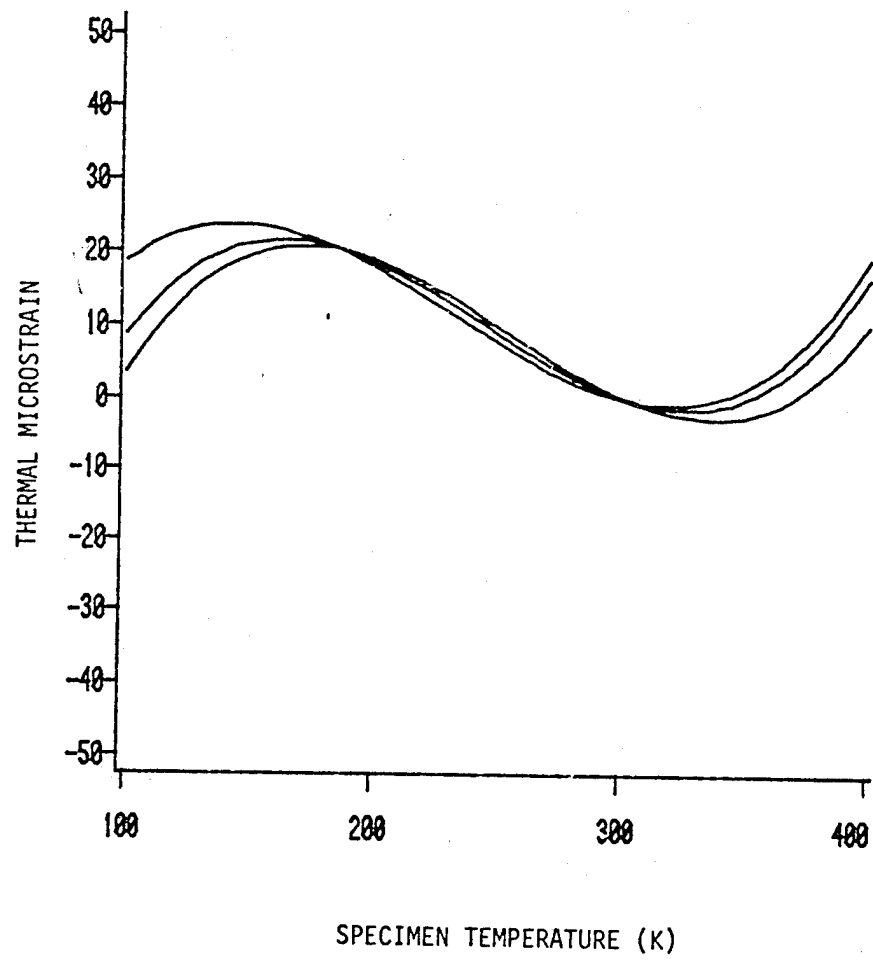
Fig. 4.7
[0]$_8$ Specimen - All Tests

Chapter 5

CONCLUSIONS AND RECOMMENDATIONS

5.1 Apparatus

The fundamental conclusion resulting from this work was that the Priest interferometer is a useful tool for measuring thermal strains of Gr/Ep laminates. Advantages of this technique have been mentioned previously but are restated below for completeness.

First of all the Priest interferometer is simple--both to understand and to use. This factors was important in its construction and subsequent use. A large amount of data was collected in a relatively short period of time, mainly due to the ease of specimen and test preparation. Another benefit of this simplicity, discovered during testing, was the ruggedness of the apparatus. Despite a number of fragile optical components, no down time for repair was required. Part of the credit for this goes to the shelf-type optical bench. But in addition, the interferometer itself required little maintenance.

By its nature the Priest interferometer is best suited to global strain measurements. This makes it adaptable to other geometries-- tubular specimens immediately coming to mind. Also, range and resolution of the device can be varied to some extent by using reference rods made from a material with a different thermal response.

On the negative side, the Priest interferometer is not the technique of choice when specimen bending is suspected. This interferometer is not capable of detecting the rotational motion associated with bend-

ing. If this type of specimen behavior is to be monitored then a local
technique such as moire interferometry [2,11] should be used.

There are several suggestions for improvement of the current appar-
atus which should be made at this point. First of all a better means of
supporting the reference rods should be developed. One possible solu-
tion is a unitized construction interferometer such as that illustrated
in Fig. 2.1. It should also be noted that there is no reason, other
than availability, to have used such a bulky top flat in the present de-
sign. Some relief from the fringe rotation problem could possibly be
realized with the present design by simply reducing the weight of the
top flat.

It is standard practice to conduct small magnitude strain measure-
ments in a vacuum. If this capability were to be added to the present
apparatus there would be two benefits. The problems with moisture in
the oven during final heating would be eliminated and a more accurate
simulation of the space environment would automatically result. If a
vacuum is used care must be taken to make sure temperature measurements
are accurate. This problem may be reduced by operating with an inert
gas environment [7].

5.2 Test Results

Conclusions concerning the composite specimens tested are listed
below. It should be realized that these conclusions are reached based
on limitations imposed by the measuring device used. Subsequent in-
vestigation using an improved Priest interferometer and concentrating on

experimentation rather than technique development could be expected to produce more precise experimental results.

i) There was no appreciable difference in thermal expansion between different specimens of the same width. This fact is illustrated by Figures 4.4 and 4.5.

ii) There was no appreciable difference in thermal expansion between specimens of different widths. See Figure 4.6.

iii) There was no appreciable difference in specimen response from run to run for the same specimen. Moisture effects have been discounted as a source of run to run variability (see App. A) but there still appears to be some variation in response at low temperatures as can be seen by comparing several plots in Appendix C for the same specimen. Unfortunately the fringe rotation problem makes it impossible to say whether this variation is due to differences in material response or experimental error.

iv) The thermal expansion of a $[0]_8$ Gr/Ep specimen is much lower than that for a quasi-isotropic specimen, being essentially zero above room temperature. Also, the behavior of the $[0]_8$ specimen tested herein changed markedly below room temperature with the CTF taking on a relatively large negative value and its sign appearing to reverse again at temperatures near the bottom of the test range.

REFERENCES

1. Johnson, R. Kural, M., MacKey, G., "Thermal Expansion Properties of Composite Materials," NASA Contractor Report 165632, Contract NASI-14887, July, 1981.

2. Bowles, D. Post, D., Herakoyich, C., Tenney, D., "Thermal Expansion of Composites Using Moire Interferometry," Virginia Polytechnic Institute and State University, VPI-E-80-19, August, 1980.

3. Wolff, E., "Measurement Techniques for Low Expansion Materials and Process--In Service Performance." Vol. 9, National SAMPE Technical Conference Series, Oct. 1977.

4. Hyer, M. W., Hagaman, J. A., "Thermal Cycling of Graphite-Polyimide," Virginia Polytechnic Institute and State University, VPI-E-79-15, April 1979.

5. Strife, J., Prewo, K., "The Thermal Expansion Behavior of Unidirectional and Bidirectional Kevlar/Epoxy Composites," J. Comp. Materials, Vol. 13, Oct. 1979, pp. 264-277.

6. Camahort, J., Rennhack, E., Coons, W., "Effects of Thermal Cycling Environments on Graphite Epoxy Composites," Env. Effects on Adv. Comp. Mat'ls., ASTM STP 602, June 1975, pp. 37-49.

7. ASTM Standard Test Method for "Linear Thermal Expansion of Rigid Solids with Interferometry," Designation E289-70, 1980 Annual Book of ASTM Standards, Part 44.

8. Post, D., "Optical Interference for Deformation Measurements--Classical, Holographic and Moire Interferometry," Proceedings of Conference on Mechanics of Nondestructive Testing, VPI & SU, Blacksburg, VA, Plenum Publishing Co., Sept. 1980.

9. Hahn, T., Kirby, R., "Thermal Expansion of Fused Silica From 80 to 1000K--Standard Reference Material 739," Thermal Expansion-1971, AIP Conference Proceedings no. 3, 1972.

10. Wood, J., Graduate Student in Engineering Mechanics, VA Tech, Blacksburg, VA 24061--Personal Correspondence.

11. Brooks, E., Herakovich, C. Post, D., Hyer, M., "Advances in Moire Interferometry for Thermal Response of Composites," Virginia Polytechnic Institute and State University, VPI-E-82-4, March 1982.

12. Draper, N. Smith, H., Applied Regression Analysis, John Wiley & Sons, Inc. New York, 1966, pp. 167-169.

13. McKague, E., Reynolds, J., Halkias, J., "Moisture Diffusion in Fiber Reinforced Plastics," Jl. of Eng. Mat'ls. and Tech., Jan. 1976, pp. 92-95.

14. Loos, A., Springer, G., "Moisture Absorption of Graphite-Epoxy Composites Immersed in Liquids and in Humid Air," J. Comp. Materials, Vol. 13, Oct. 1979, pp. 131-147.

15. Chapman, A. T., Heat Transfer, 3rd edition, Macmillian Pub. Co., New York, 1974, pp. 127-134.

16. Tompkins, S. S., NASA/Langley Research Center, Hampton, VA 23666-- Personal Correspondence.

17. Anonymous, "High Temperature Optical Glasses," ULE-Titanium Silicate-Code 7971," Corning Glass Co., Corning, NY.

Appendix A

Supporting Evidence for the Assumption of

Negligible Moisture Effects

Prior to testing the composite specimens, there was some concern about how to treat moisture effects on the expansion of the test specimens. It was decided to "pre-soak" the specimens for 18 hours at 394°K (250°F) in order to dry them and thus remove moisture effects from the picture. The soak temperature was selected to be below the Gr/Ep curing temperature in order to avoid inadvertent post-curing of the specimens. The 18 hour soak time was chosen somewhat arbitrarily--taking into account scheduling problems for the lengthy experimental program. Because of the arbitrary nature of this presoak specification, special efforts were made to be sure that the pre-soak accomplished the desired result. Evidence indicating that this was indeed the case is presented below.

Theoretical Evidence

McKeague, et al. [13] present a quasi-empirical method of calculating moisture content in Gr/Ep laminates as a function of time, temperature, relative humidity, and initial moisture content. Their method, which correlates well with experimental results on laminates similar to those studied in this work, is used here to calculate the moisture content expected after presoak.

Consider the moisture history given in Table A.1.

Table A.1

Moisture History

Elapsed Time	%Relative Humidity	Temp (K)	Specimen Location
2 yrs.	50	295	Open Air Storage
1 mo.	< 2	295	Dessicator
18 hrs.	< 1	395	Drying Oven

For this moisture history McKeague's formula must be applied twice, once to get the moisture content at the end of dessication, M_1, and a second time to calculate the content after pre-soak, M_2. McKeague's formula is given as

$$M = M_i + (AH - M_i)\tanh((2S/V)(D_0\exp(-E/RT)t/\pi)^{1/2}) \qquad \text{(A.1)}$$

This is equation (6) from [13]. The reader is cautioned that this equation, as presented in the original paper, is slightly in error. This equation is the theoretical solution to the diffusion equation given in [13] modified to account for the experimentally observed nonlinear approach to equilibrium moisture content. The notation is defined as follows:

M = moisture content (wt. %)

M_i = initial moisture content

A = absorptivity coefficient

H = relative humidity (%)

S = total specimen surface area (cm^2)

V = specimen volume (cm^3)

D_0 = permeability index (cm^2/sec)

E = diffusion activation energy (J/gm)

K = gas constant (J/gm-k)

T = temperature (k)

t = time (seconds)

Loos and Springer [14] report a summary of experimental results for constants the A, D_0 and E. However, it appears that the most conservative (slowest drying rate) results are obtained by using the values for these constants reported in [13]. Assuming a specimen size of

7.62cm x 2.54cm x .102cm (3 in. x 1 in. x .04 in.)

and using the constants from [13], equation (A.1) becomes

$$M = M_i + (.0146H - M_i)tanh\left(.889exp(-2165/T)t^{1/2}\right. \quad (A.2)$$

Note that in calculating S/V above the total specimen area--including edges--was used.

From (A.2) the moisture content values M_1 and M_2 are easily calculated. This calculation is summarized below.

Table A.2

Moisture content calculation

	M_i (wt.%)	H(%)	T(K)	t(sec)	M(wt.%)
M_1	.73*	2	295	2.42×10^6	.23
M_2	.23	1	395	64.8×10^3	.07

*This is the equilibrium moisture content at 50% RH based on data reported in [13].

These results indicate that the dessicator plus pre-soak treatment will reduce the specimen moisture content 90% (from .73 to .07 percent by weight) prior to testing. A smaller percent reduction would be calculated for the 6.35 mm (0.25 in.) wide specimen because of the smaller S/V ratio. However, this difference should not be significant. In both cases it appears, based on this "quasi-theoretical" prediction, that the specimens should be substantially dried out prior to testing.

Experimental Evidence

Several dummy specimens were used to check specimen moisture loss prior to and during testing. In each case the dummy specimen was treated identically to the specimen being tested except that it was not mounted on the interferometer. This allowed the dummy specimen to be weighed before and after testing.

Table A-3 shows the results of this weighing operation for four dummy specimens monitored during testing of specimens 3, 4, 5 and 6. In all cases the most significant change in dummy specimen weight occurs during the presoak with specimen weight remaining essentially constant for subsequent weighings.

Perhaps the most compelling evidence that moisture effects were negligible were the experimental results themselves. Except for test C3-1 there are no test results which indicate a large residual thermal strain which could be indicative of significant moisture effects.

Table A.3

Dummy Sample Weights vs. Time

Specimen[3] Number	wt.[1] Before Soak	wt. %[2] Diff.	After Soak	wt. % Diff.	After Run 1	wt. % Diff.	After Run 2	wt. % Diff.	After Run 3
3	3.2729		3.2489		3.2500		3.2500		3.2500
		-.738		+.003		.000		.000	
4	3.3500		3.3275		3.3281		3.3280		3.3216
		-.676		+.018		-.003		-.012	
5	.8389		.8344		.8346		.8338		.8346
		-.500		+.024		-.096		+.096	
6	.8274		.8244		.8245		.8245		.8245
		-.364		+.012		.000		.000	

Note:

1. All wts. in grams
2. % Diff. = (previous wt. - subsequent wt.) x 100/previous wt.
3. Specimens 3 and 4 were 25.4 mm wide while specimens 5 and 6 were 6.35 mm wide. All four specimens were 8 ply Quasi-isotropic Gr/Ep.

APPENDIX B

Supporting Evidence for Use of 45 Minute Soak Time

The 45 minute soak time was assumed to provide sufficient time for the interferometer and specimen to reach thermal equilibrium between fringe photos. Results of a simple heat transfer calclation assuming the top optical flat and the specimen to be infinite slabs (thus neglecting heat transfer through the edges) are presented below to verify that this length of time was adequate.

First make the following assumptions:

   i)   composite specimen and interferometer top flat can be modeled as infinite slabs.

  ii)   Upon changing the oven temperature the specimen and top flat surfaces immediately come to the oven temperature.

 iii)   After it has changed, the oven temperature remains constant.

The one dimensional heat transfer problem defined by these assumptions is solved in many heat transfer texts such, as Chapman [15]. This author gives a graphically tabulated solution for the nondimensional temperature change, $\Delta\theta$, at the center of the slab in terms of the Fourier modulus N_{FO}. Using this solution for $\Delta\theta$, the time required for a slab to reach 90% of equilibrium can be calculated based on a knowledge of N_{FO} as defined below.

Define:

$$\Delta\theta = (T - t_f)/(t_i - t_f) \text{ where,}$$

t = temperature at middle of slab

t_i = initial temperature at middle of slab

t_f = ambient temperature to which slab is heated

and $N_{FO} = \alpha\tau/L^2$ where

α = thermal diffusivity of slab

τ = elapsed time

L = slab half-thickness.

These definitions are used in Table B.1.

The values for τ given in Table B.1 represent the time required for a slab of material having the given characteristics to come to 90% of the ambient temperature. Both of these values are quite small compared with a soak time of 45 minutes (2700 sec.).

Although the above analysis is approximate, the small soak times it predicts for the specimen and top flat indicate that the 45 minute soak time is adequate. The quartz rods must also come to thermal equilibrium for the interferometer to function properly. However, since thermal equilibrium will be approached more rapidly for the thin quartz rods than for the bulky top flat (given similar values of α for the two glasses), the quartz rods were not included in the analysis.

Table B.1

Heat Transfer Calculation Summary

Material[1]	$\Delta\theta$	N_{FO}[2]	α[3] $(mm^2/sec.)$	$L(mm)$	$\tau(sec.)$
Gr/Ep	.9	1.04	.31	.508	1
ULE	.9	1.04	.79	12.7	212

Notes:

1. Materials are Quasi-Isotropic Gr/Ep Laminate and Corning ULE.

2. Obtained from ref. [15], Figure 4.11.

3. Room temperature thermal diffusivity values obtained from Refs. [16] and [17], respectively.

APPENDIX C

Experimental Data

Experimental results for each test are presented in this appendix. The plotted data represents measured thermal strain vs. temperature results--the strains being calculated using equation 2.17. These data were fit to either a cubic, quadratic, or linear least squares model using the backward elimination technique described by Draper and Smith [12].

After fitting the regression curve a corrected thermal strain, ε_{corr}, was calculated as

$$\varepsilon_{corr} = \varepsilon_s(T) - \varepsilon_s(T_0) \qquad (C.1)$$

where T_0 is a reference temperature, taken to be 300K. This correction was applied so the regression curves presented in Chapter 4 would have a common reference. The plotted results are ε_{corr} vs. T (deg. K) and their associated regression curve. Regression coefficients for each curve are presented in the appendix. The order of the polynomial regression model was selected using the technique mentioned above.

Vertical bars appearing on some of the plotted points represent horizontal fringe uncertainty estimated using equation 3.5 and horizontal fringe change information taken from the fringe photos. The specimen and test numbers are designated as described in Chapter 4, i.e. M7 is read "Molybdenum run no. 7" and C1-2 is read "composite specimen no. 1, test run no. 2."

$$\varepsilon_s(T) = c_0 + c_1 T + c_2 T^2 + c_3 T^3$$

$c_0 = -1158.18$

$c_1 = 0.841706$

$c_2 = 0.015100$

$c_3 = -0.000017126$
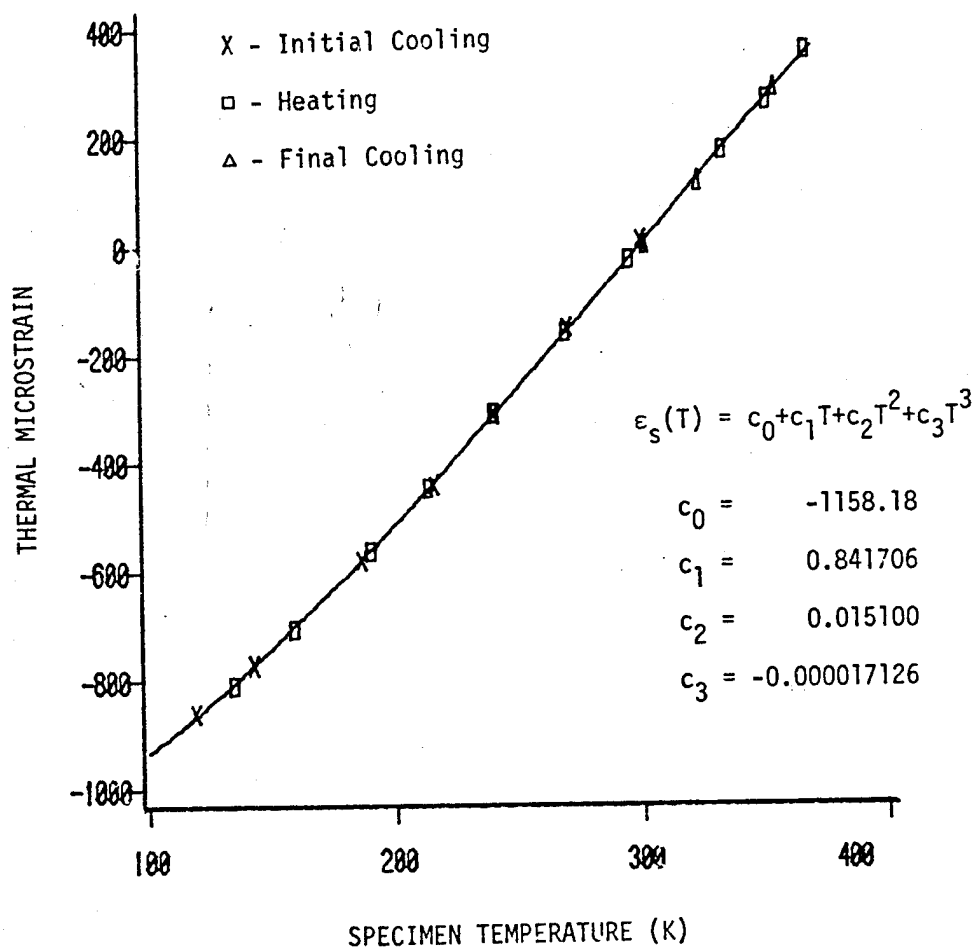
Fig. C.1 Moly Run 7
Thermal Strain vs Temperature
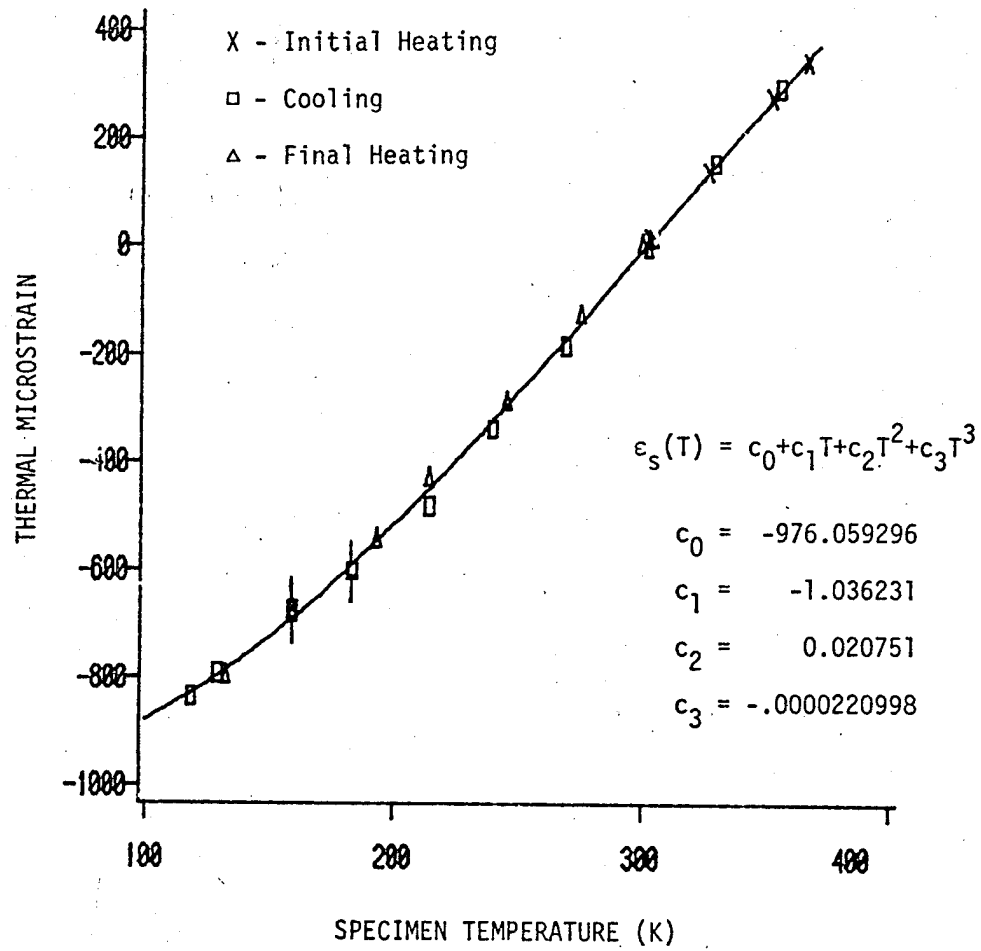
Fig. C.2 Moly Run 10
Thermal Strain vs Temperature
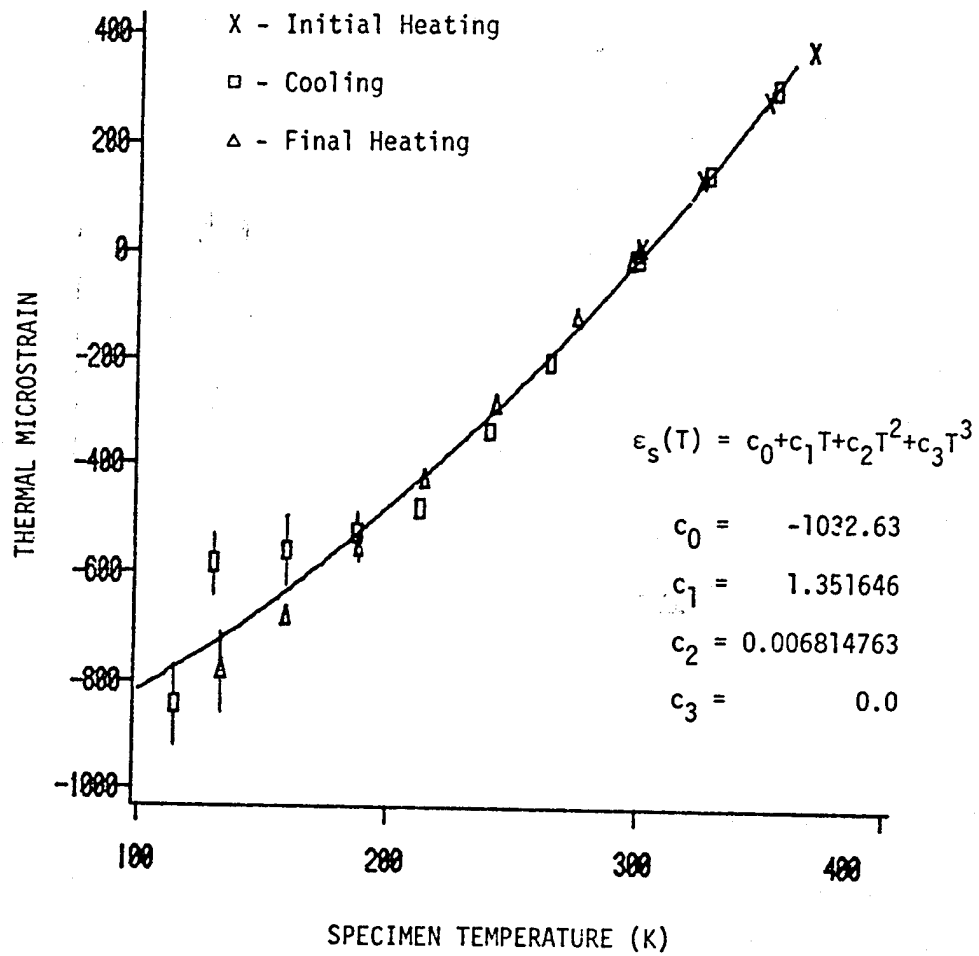
Fig. C.3 Moly Run 11
Thermal Strain vs Temperature

99
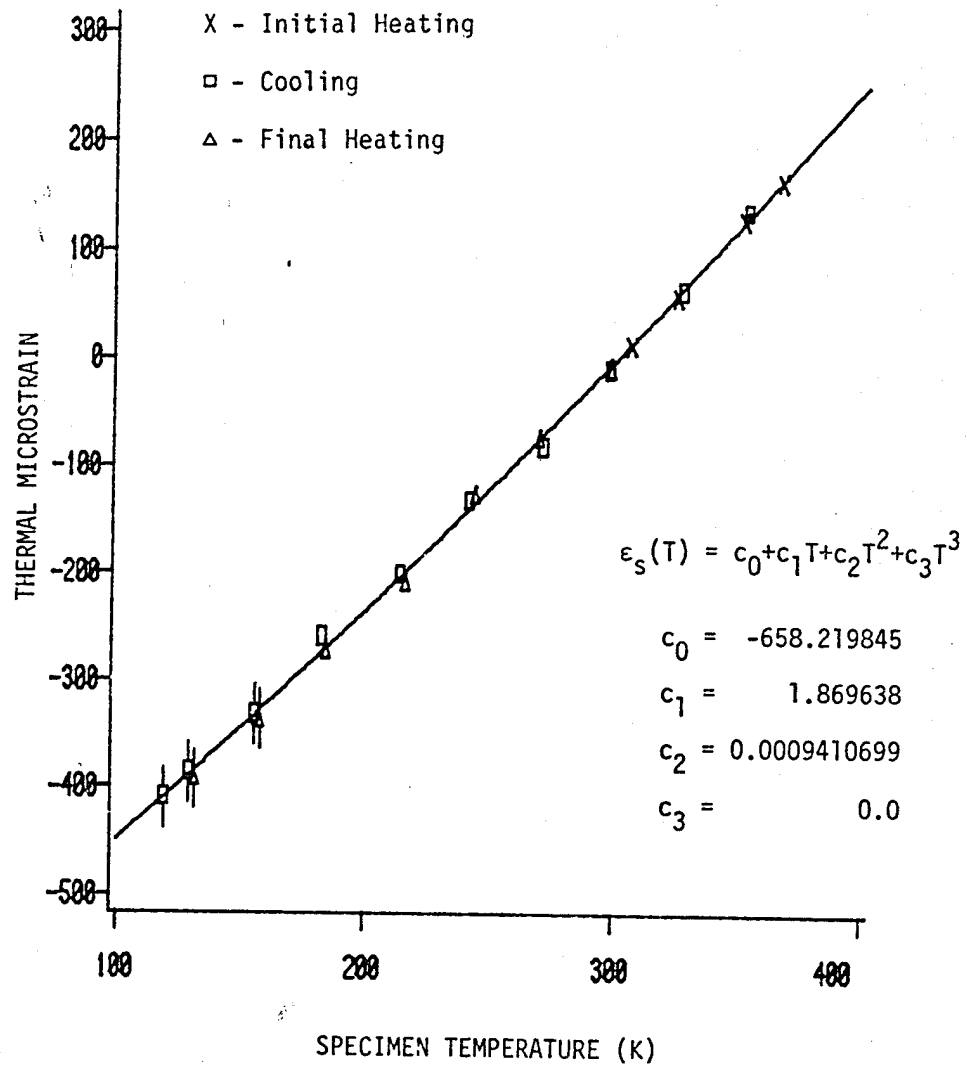
Fig. C.4 Run C1-1
Thermal Strain vs Temperature
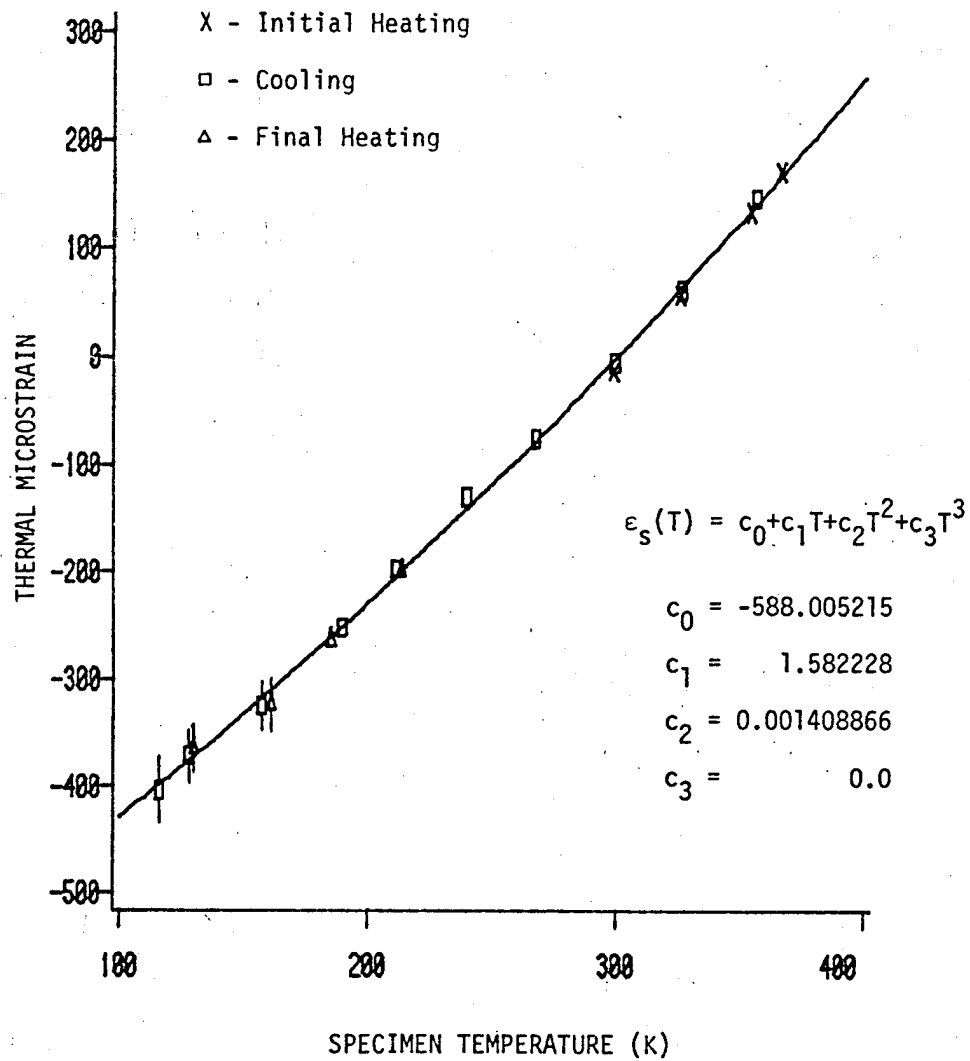
Fig. C.5 Run C1-2
Thermal Strain vs Temperature
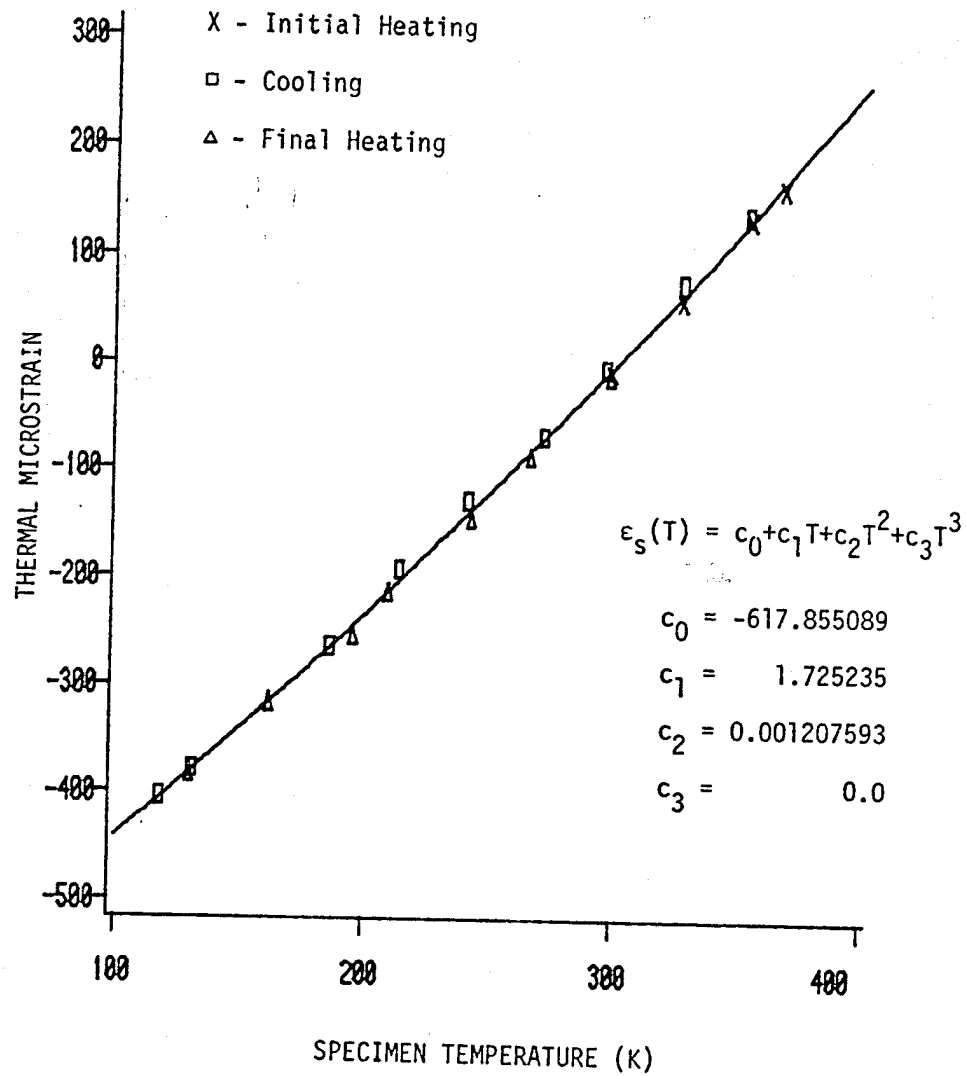
Fig. C.6 Run C1-3
Thermal Strain vs Temperature
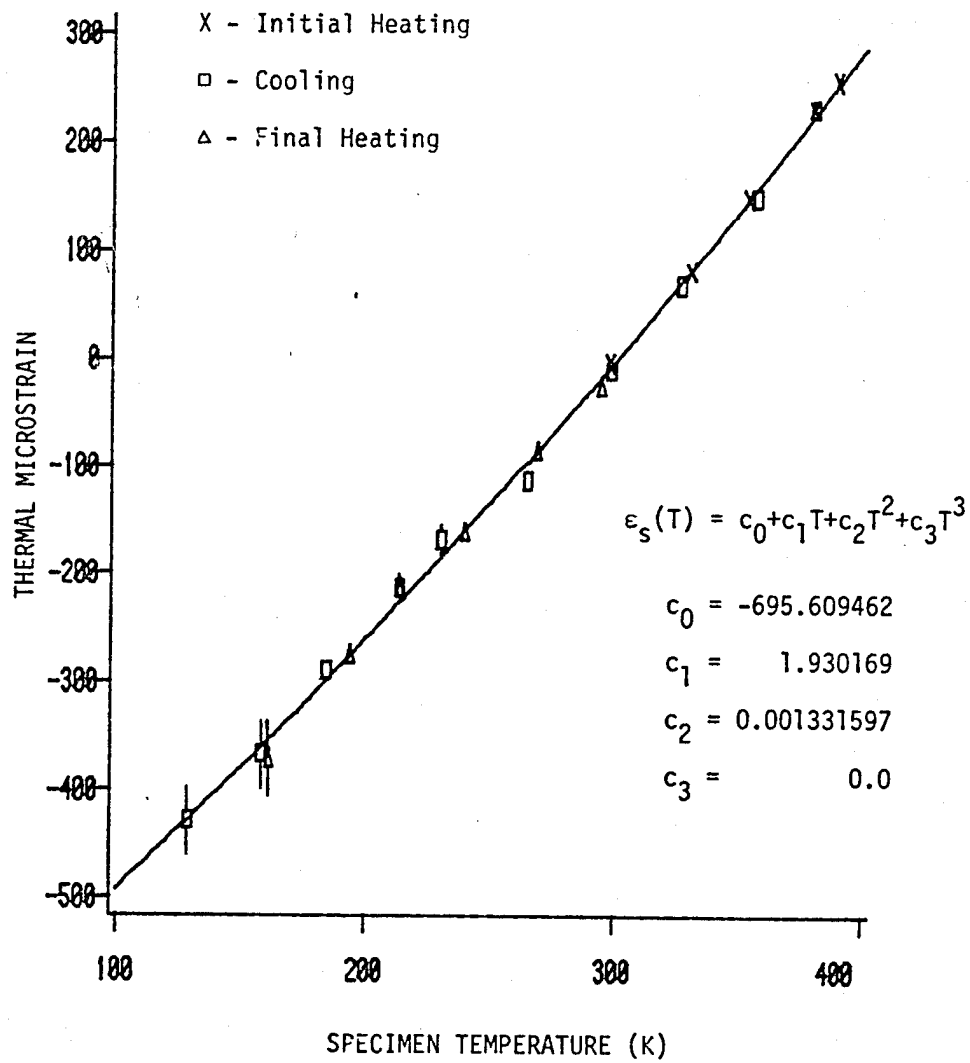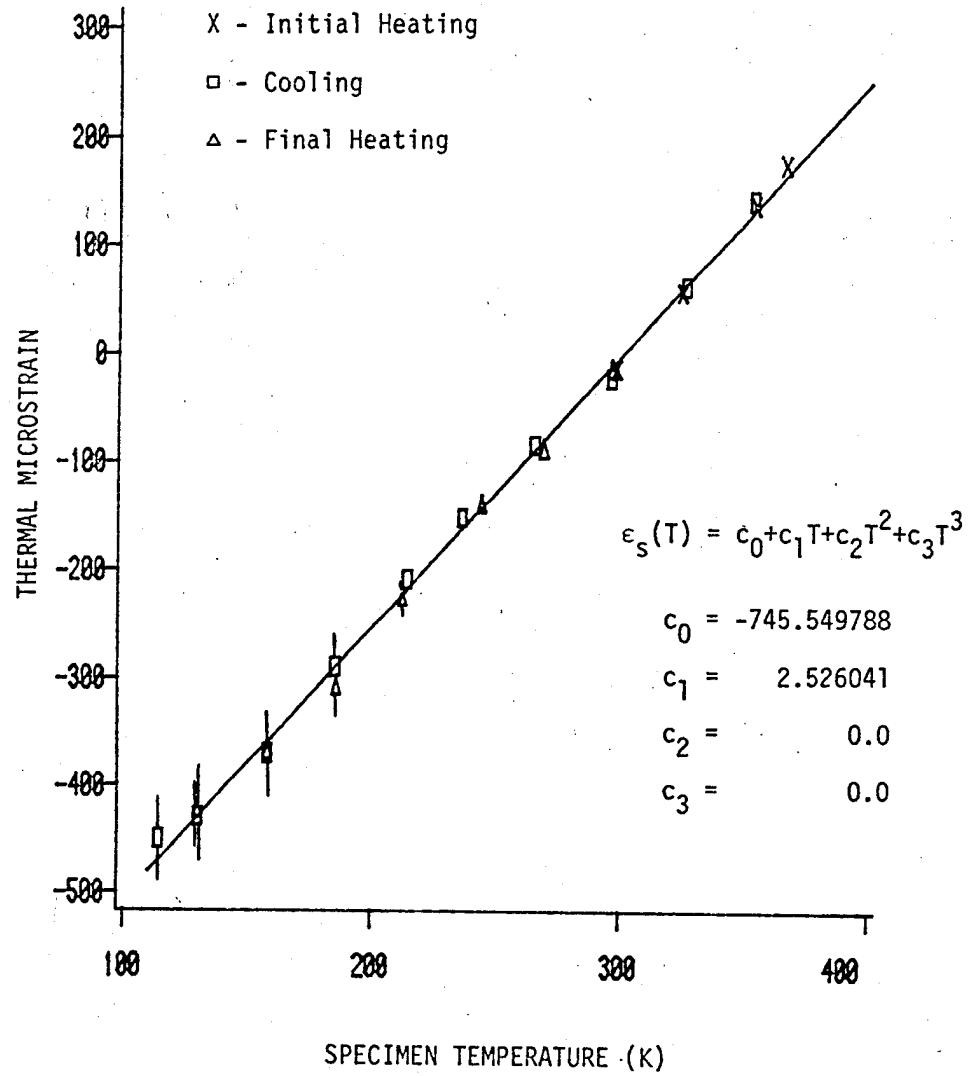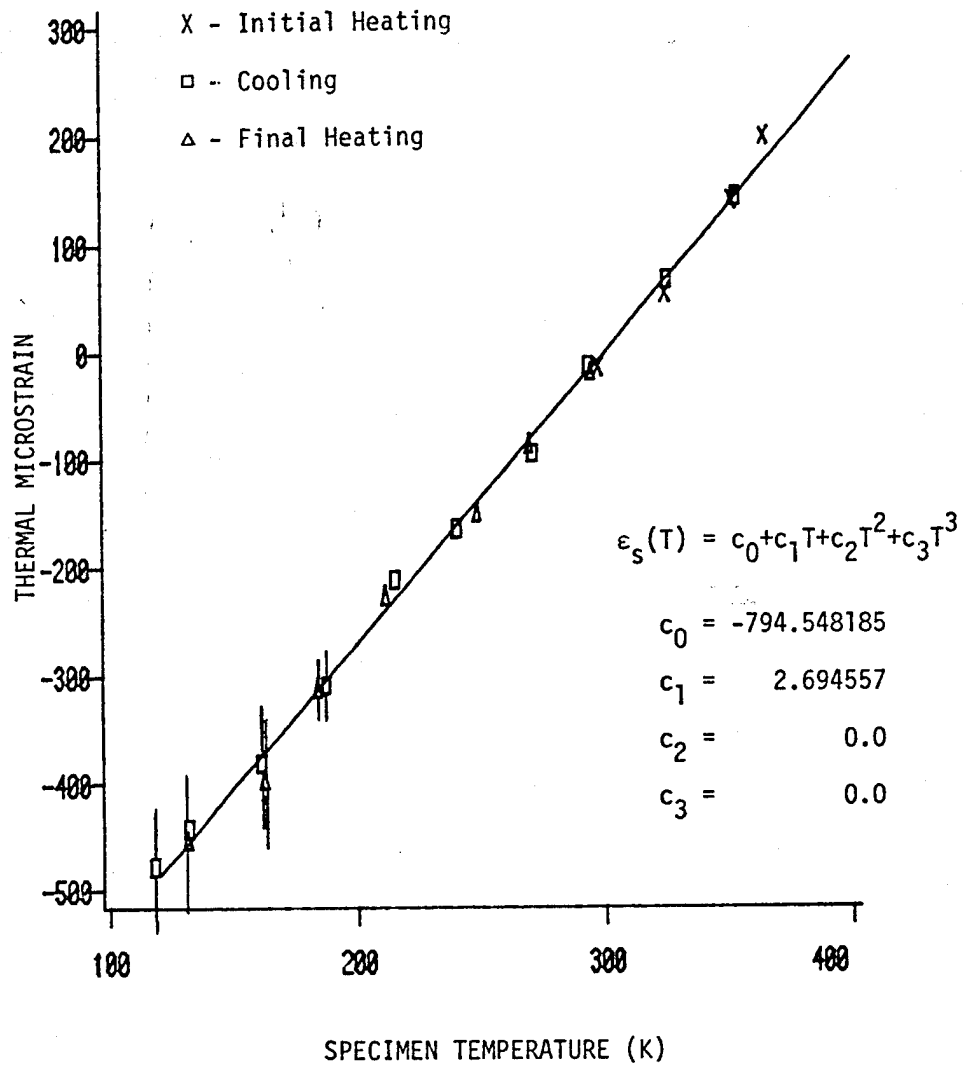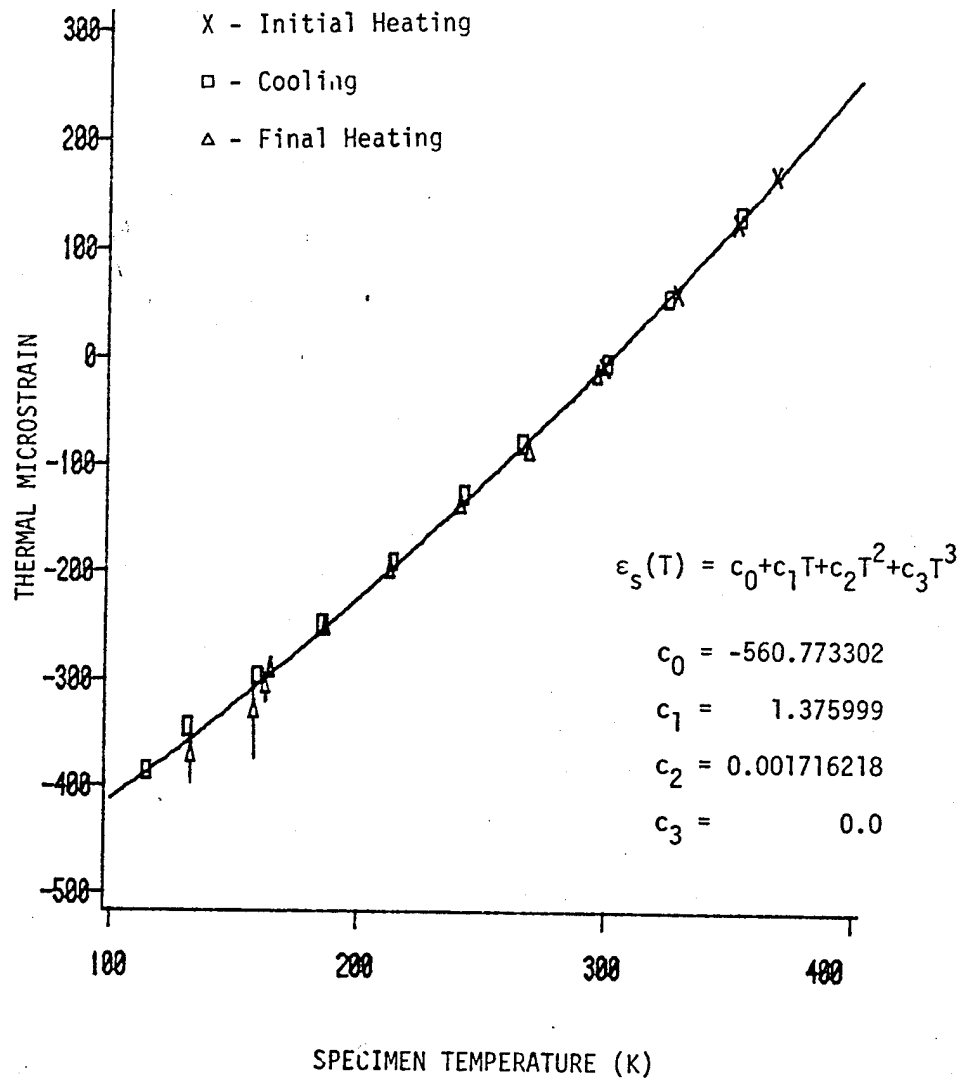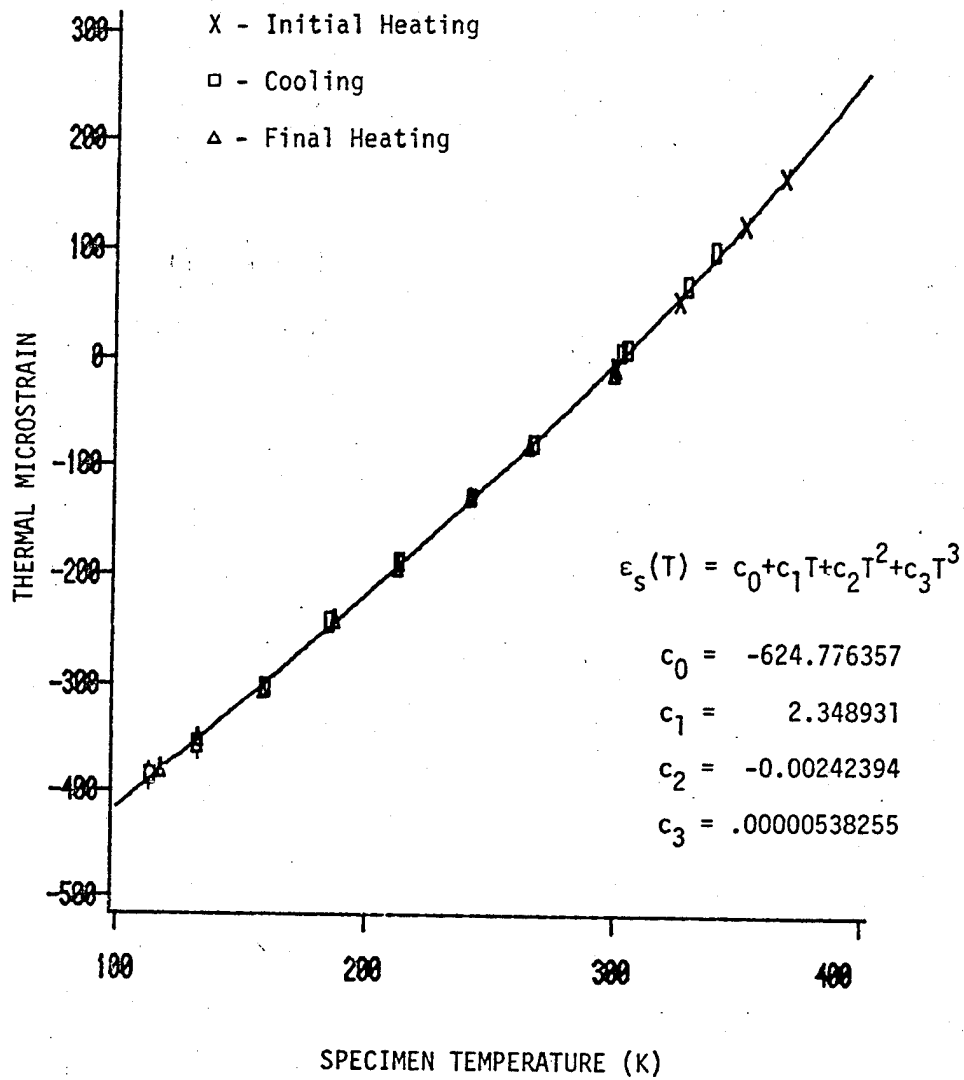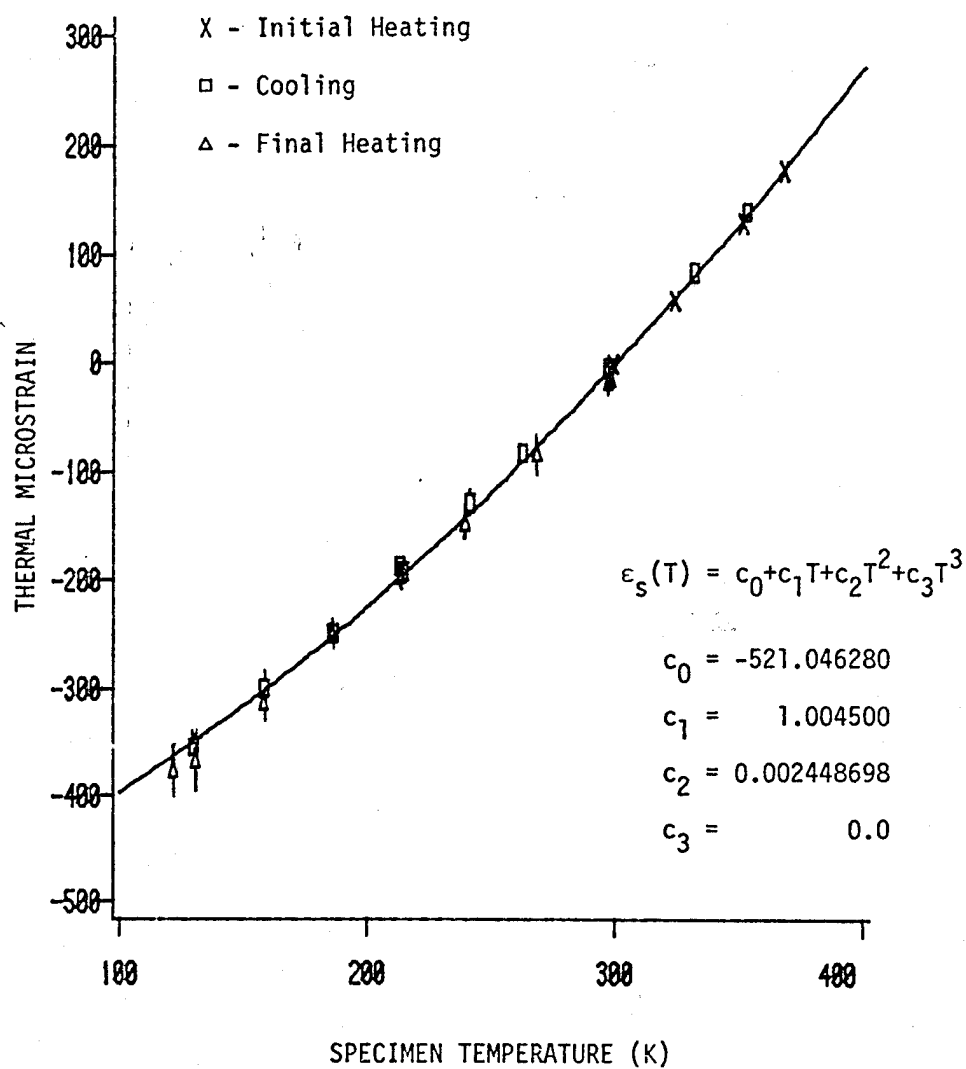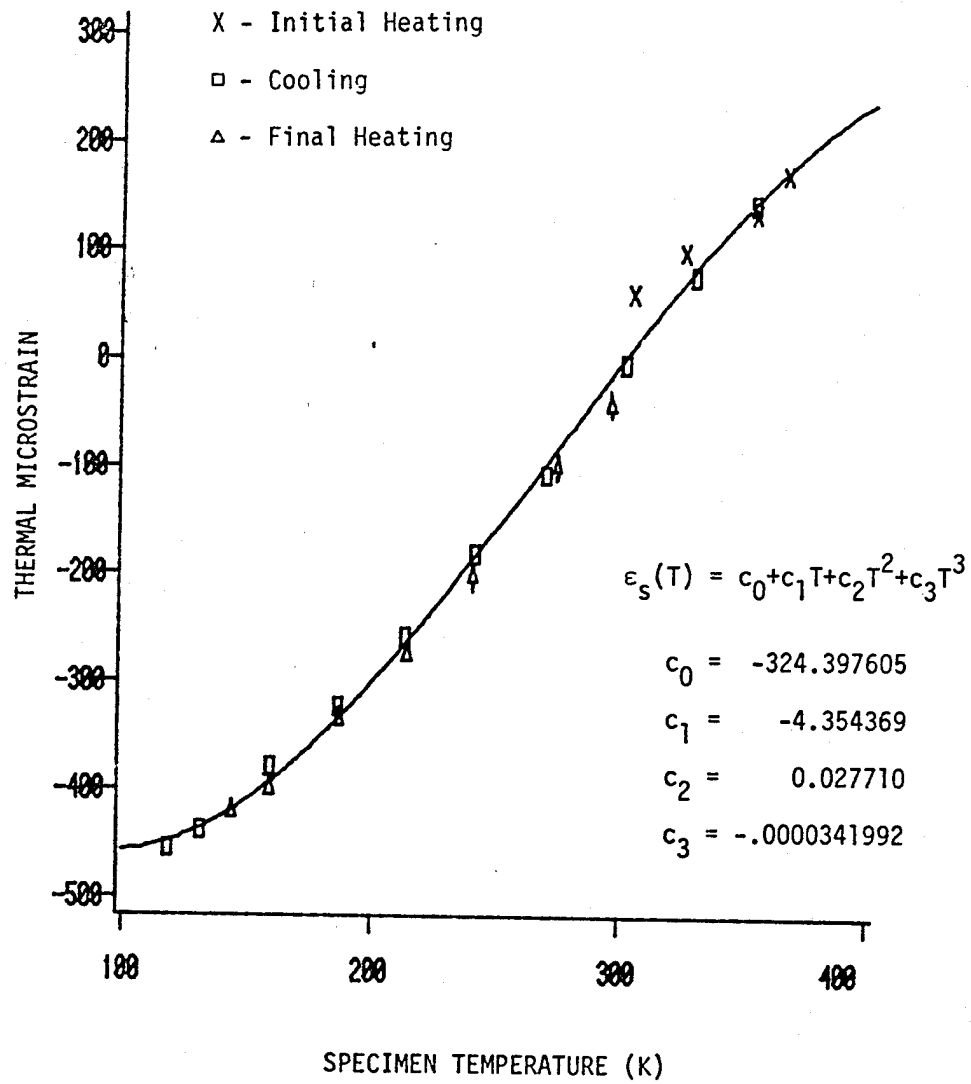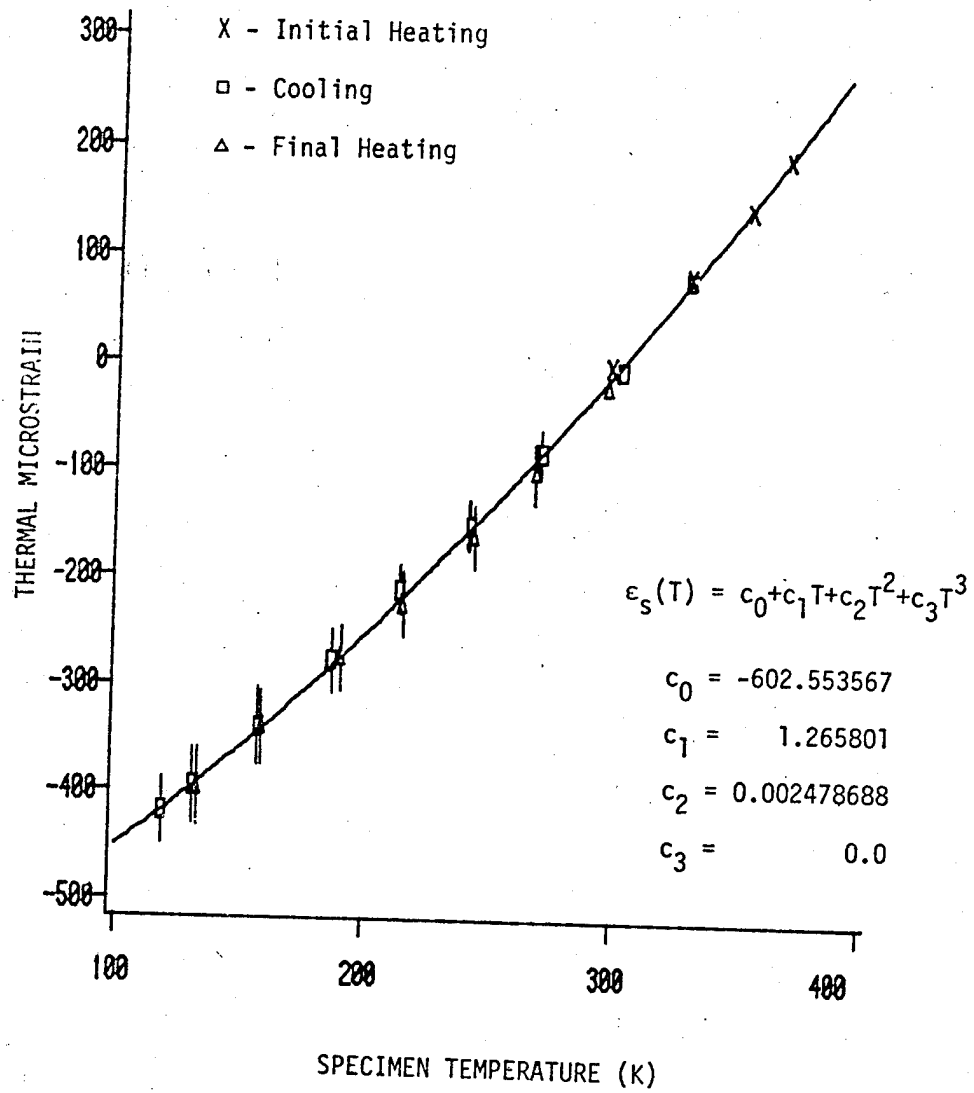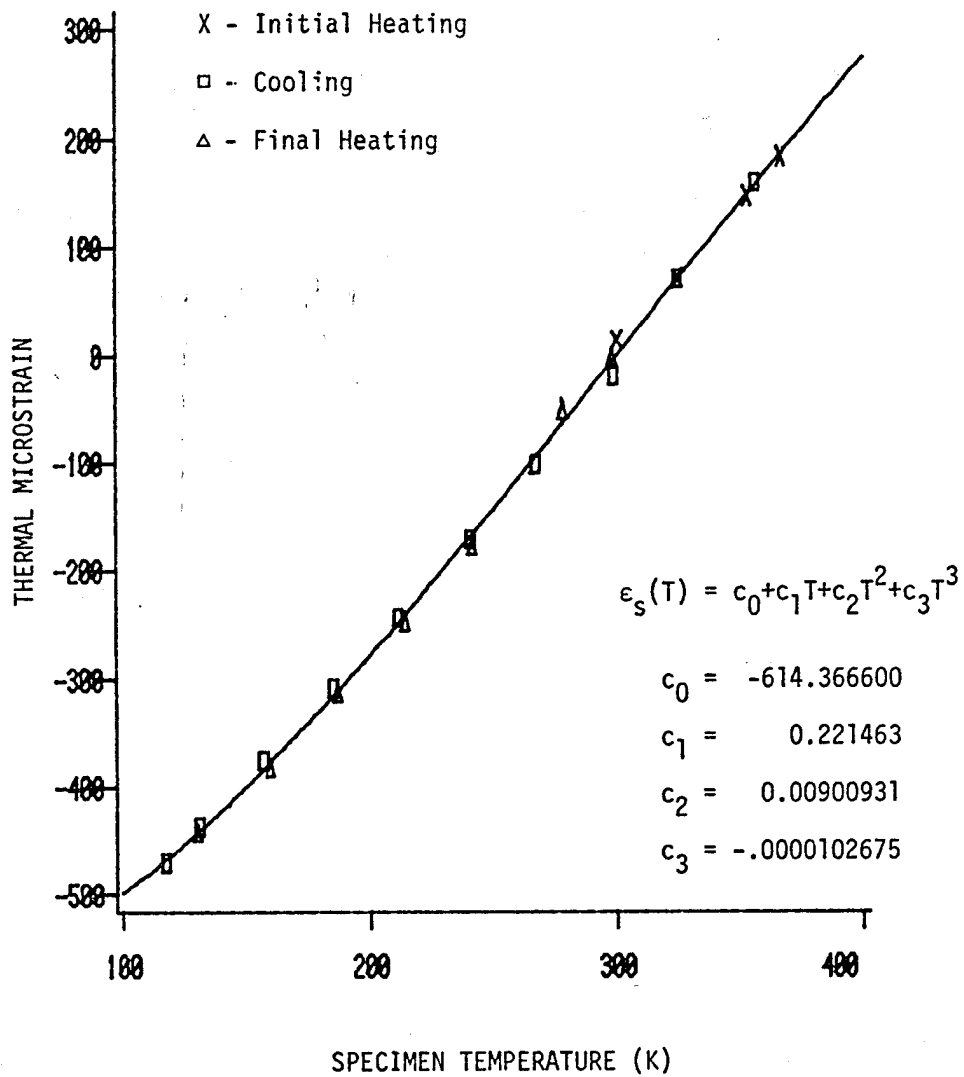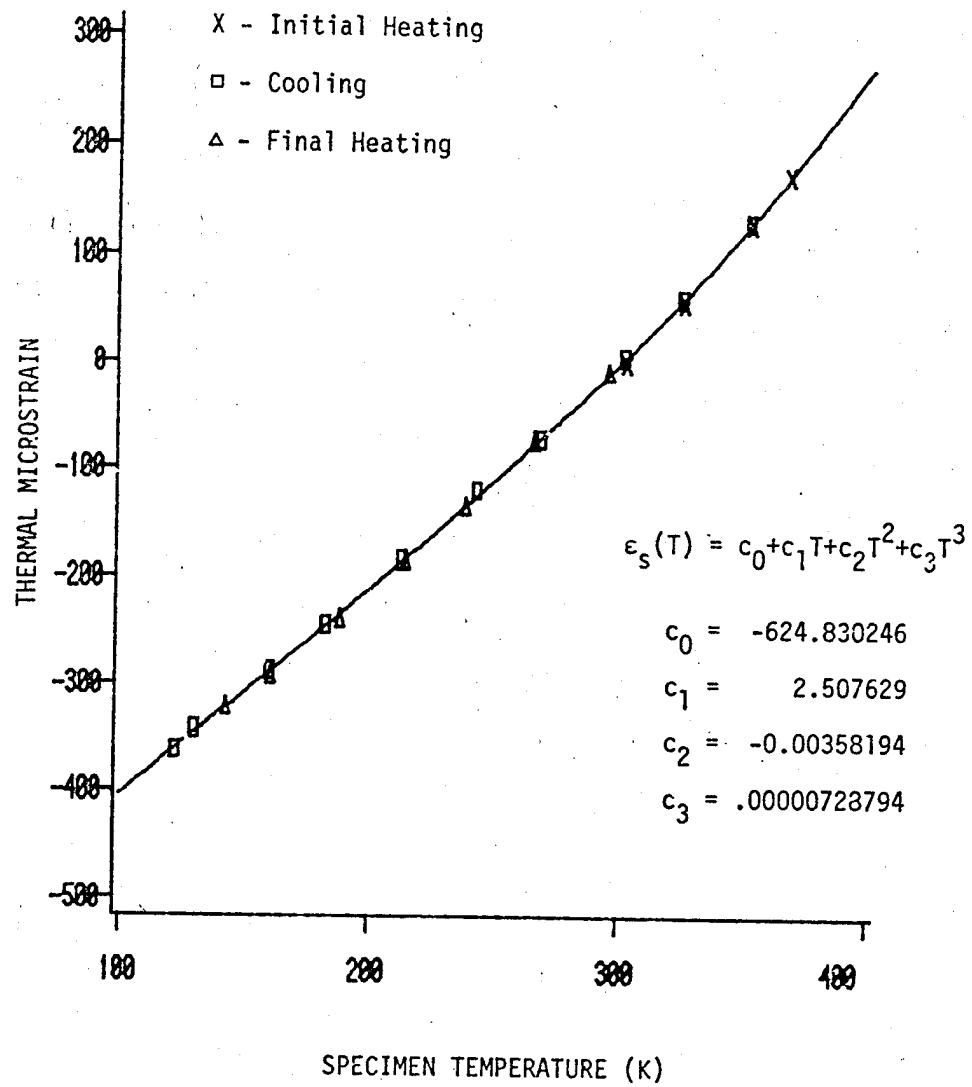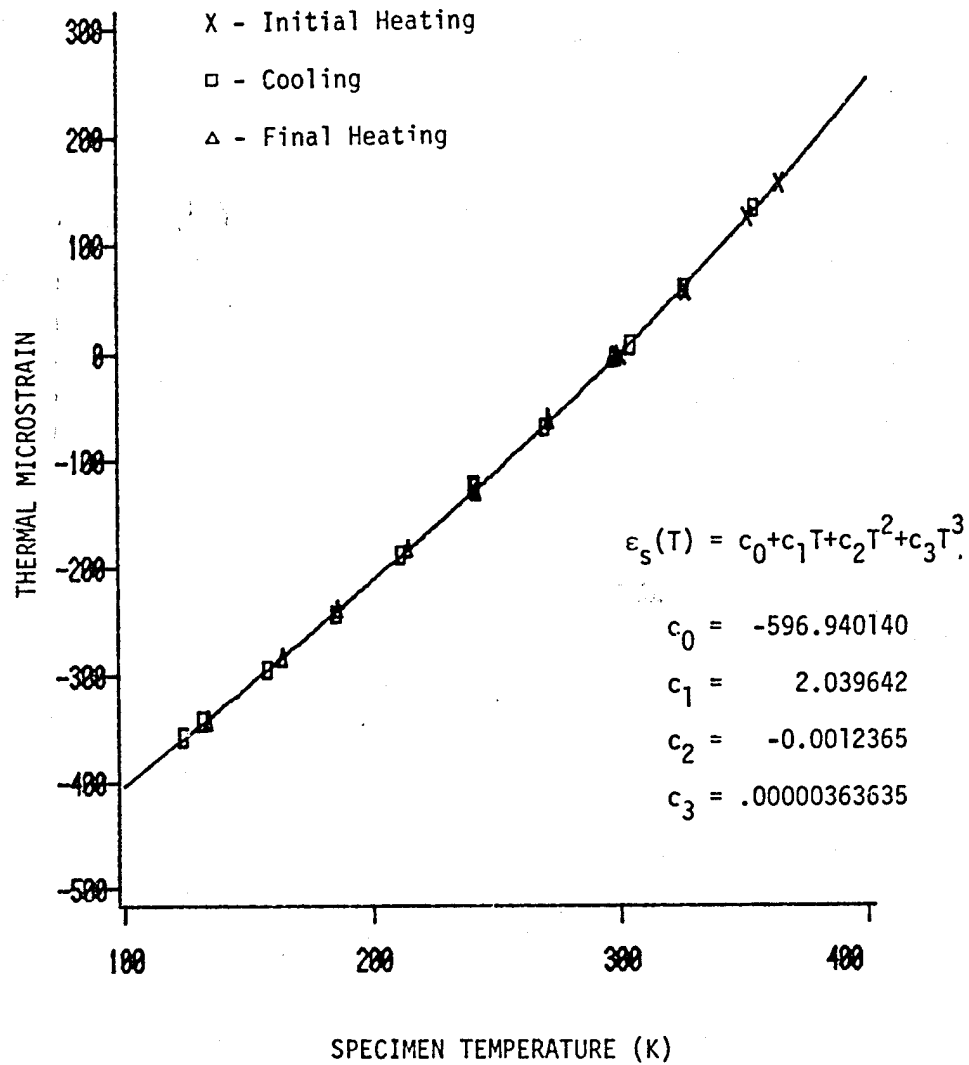
Fig. C.7 Run C2-1
Thermal Strain vs Temperature

Fig. C.8 Run C2-2
Thermal Strain vs Temperature

Fig. C.9 Run C2-3
Thermal Strain vs Temperature

X – Initial Heating

□ – Cooling

△ – Final Heating

$$\varepsilon_s(T) = c_0 + c_1 T + c_2 T^2 + c_3 T^3$$

$c_0 = -560.773302$

$c_1 = 1.375999$

$c_2 = 0.001716218$

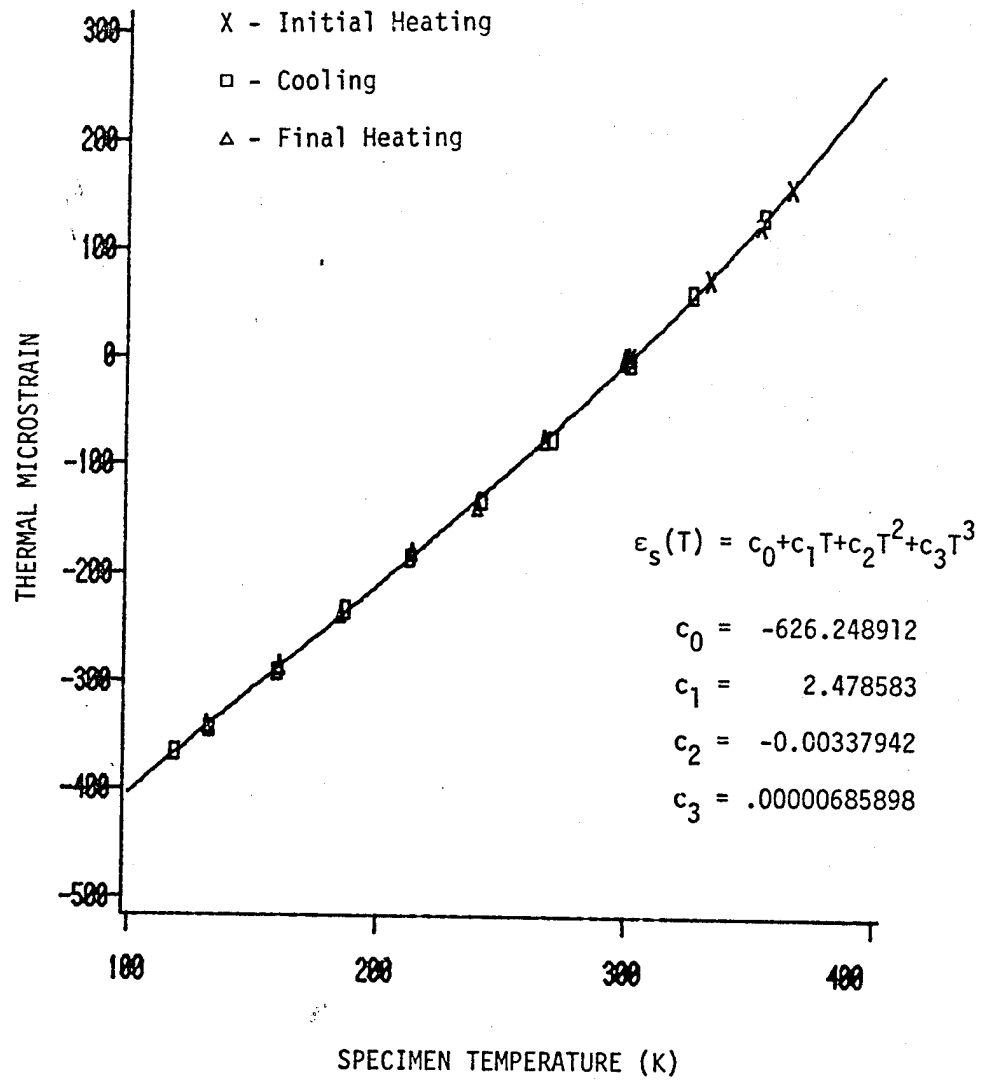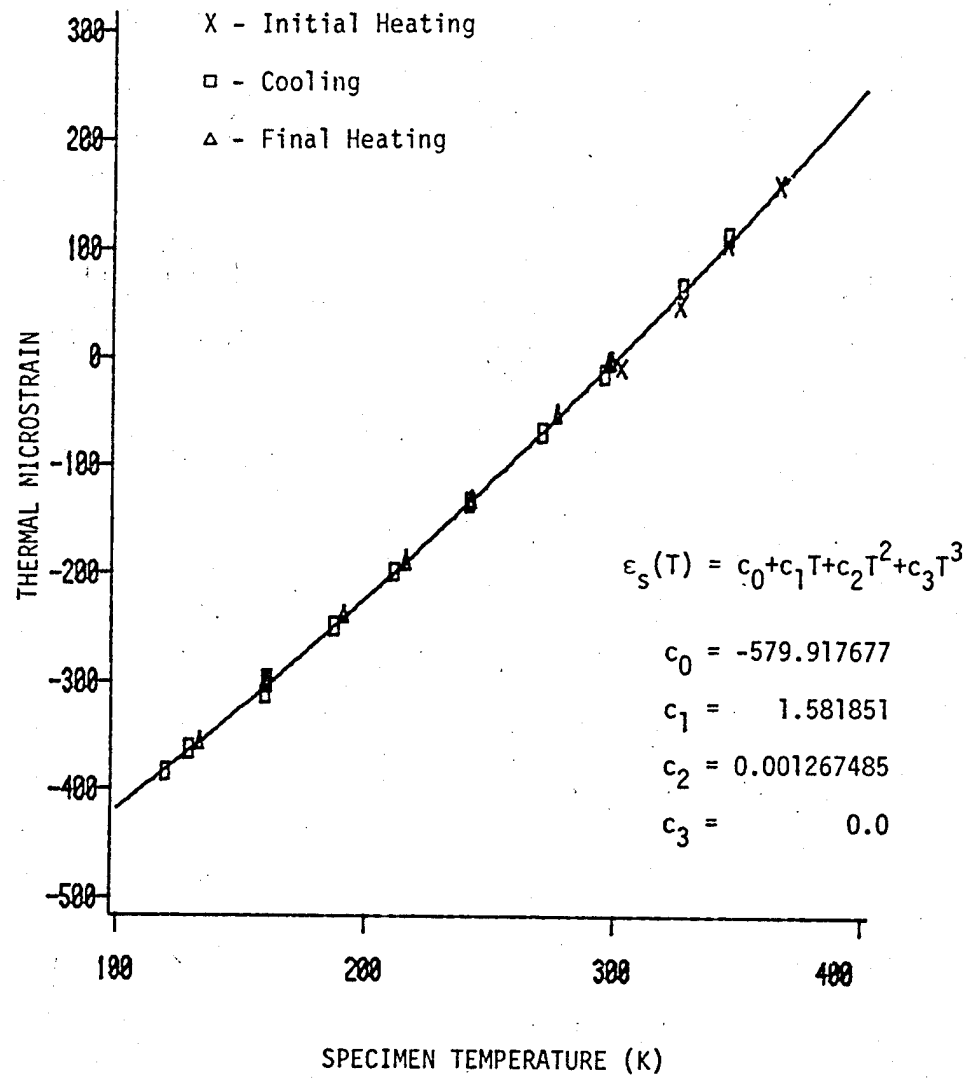$c_3 = 0.0$
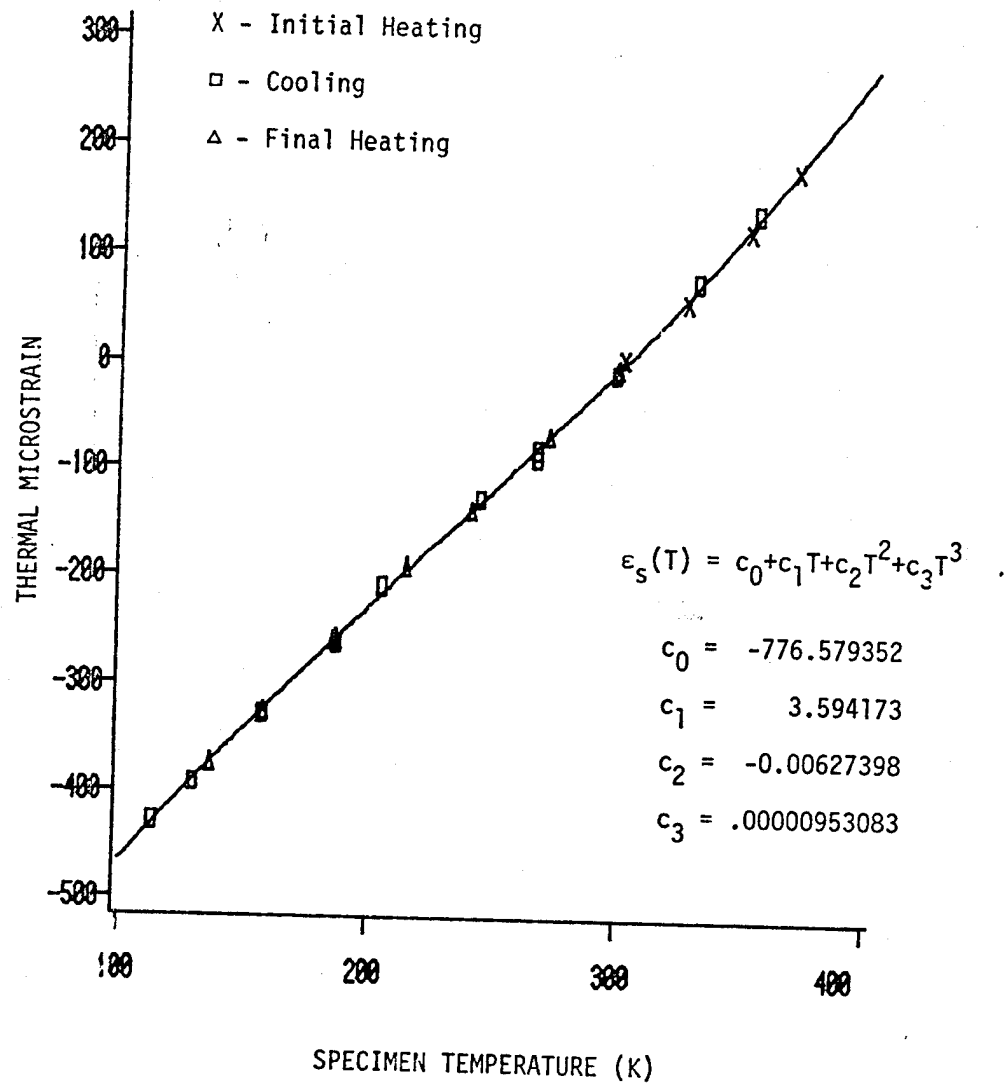
SPECIMEN TEMPERATURE (K)

Fig. C.10 Run C2-4
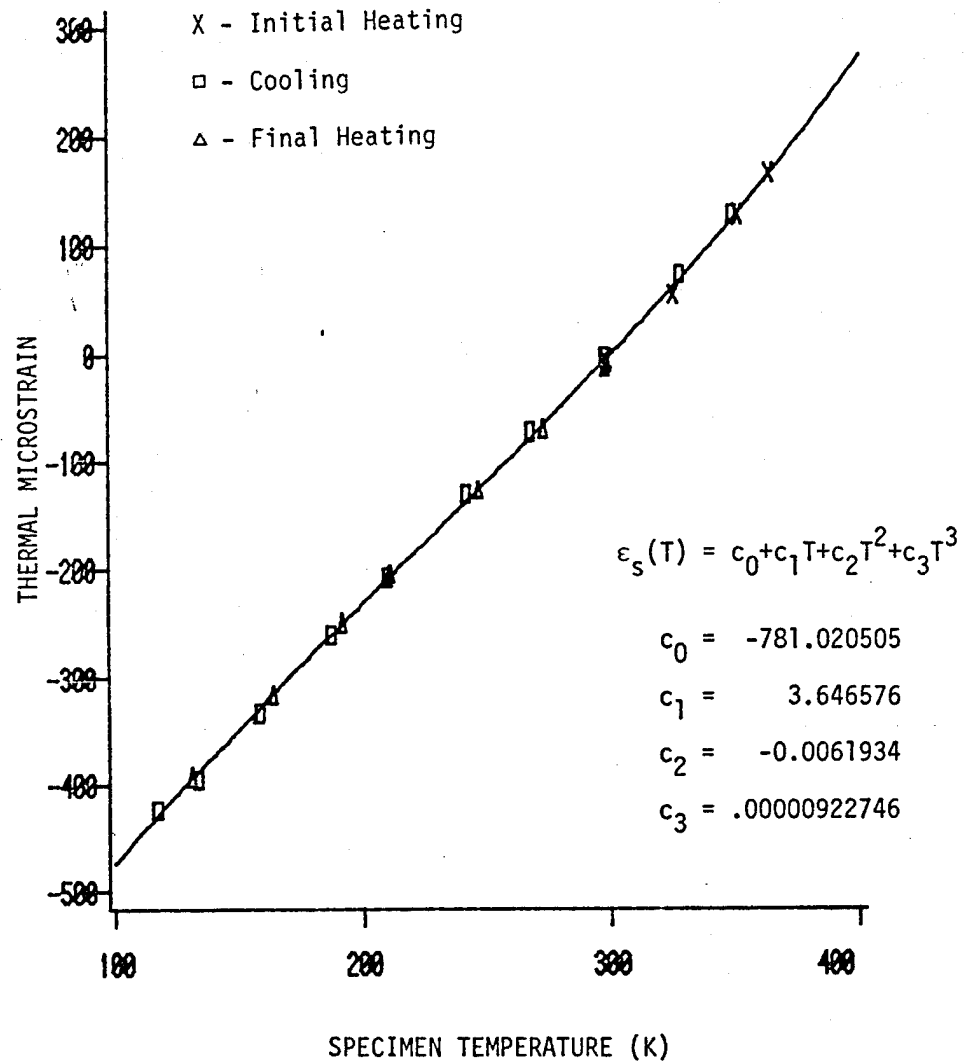Thermal Strain vs Temperature

Fig. C.11 Run C2-5
Thermal Strain vs Temperature

Fig. C.12 Run C2-6
Thermal Strain vs Temperature

$$\varepsilon_s(T) = c_0 + c_1 T + c_2 T^2 + c_3 T^3$$

c_0 = -324.397605

c_1 =   -4.354369

c_2 =   0.027710

c_3 = -.0000341992

SPECIMEN TEMPERATURE (K)

Fig. C.13 Run C3-1
Thermal Strain vs Temperature

Fig. C.14 Run C3-2
Thermal Strain vs Temperature

X - Initial Heating

□ - Cooling

△ - Final Heating

$$\varepsilon_s(T) = c_0 + c_1 T + c_2 T^2 + c_3 T^3$$

c_0 = -614.366600

c_1 = 0.221463

c_2 = 0.00900931

c_3 = -.0000102675

THERMAL MICROSTRAIN

SPECIMEN TEMPERATURE (K)

Fig. C.15 Run C3-3
Thermal Strain vs Temperature

$$\varepsilon_s(T) = c_0 + c_1 T + c_2 T^2 + c_3 T^3$$

$c_0 = -624.830246$

$c_1 = 2.507629$

$c_2 = -0.00358194$

$c_3 = .00000723794$

SPECIMEN TEMPERATURE (K)

Fig. C.16 Run C4-1
Thermal Strain vs Temperature

X - Initial Heating

□ - Cooling

△ - Final Heating

$\varepsilon_s(T) = c_0 + c_1 T + c_2 T^2 + c_3 T^3$

$c_0 = -596.940140$

$c_1 = 2.039642$

$c_2 = -0.0012365$

$c_3 = .00000363635$

THERMAL MICROSTRAIN

SPECIMEN TEMPERATURE (K)

Fig. C.17 Run C4-2
Thermal Strain vs Temperature

113

Fig. C.18 Run C4-3
Thermal Strain vs Temperature

Fig. C.19 Run C5-1
Thermal Strain vs Temperature
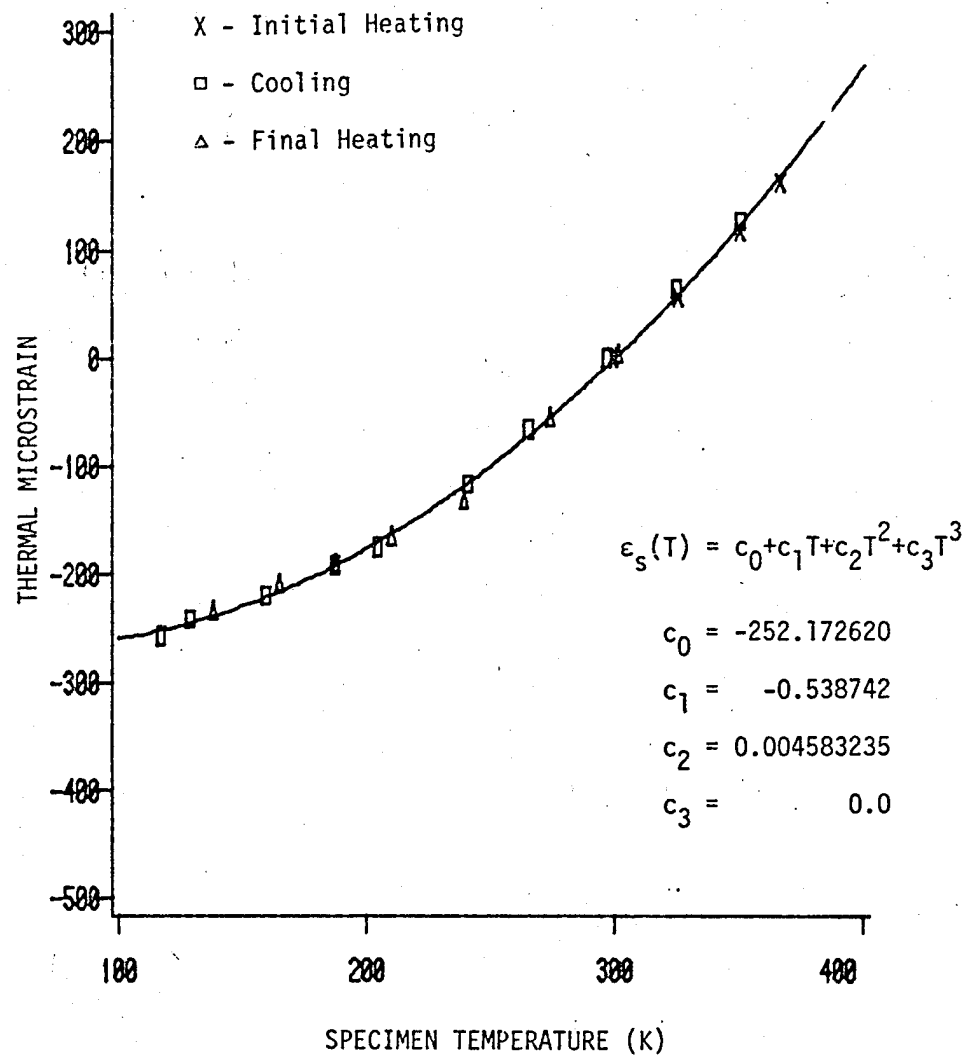
Fig. C.20 Run C5-2
Thermal Strain vs Temperature

Fig. C.21 Run C5-3
Thermal Strain vs Temperature
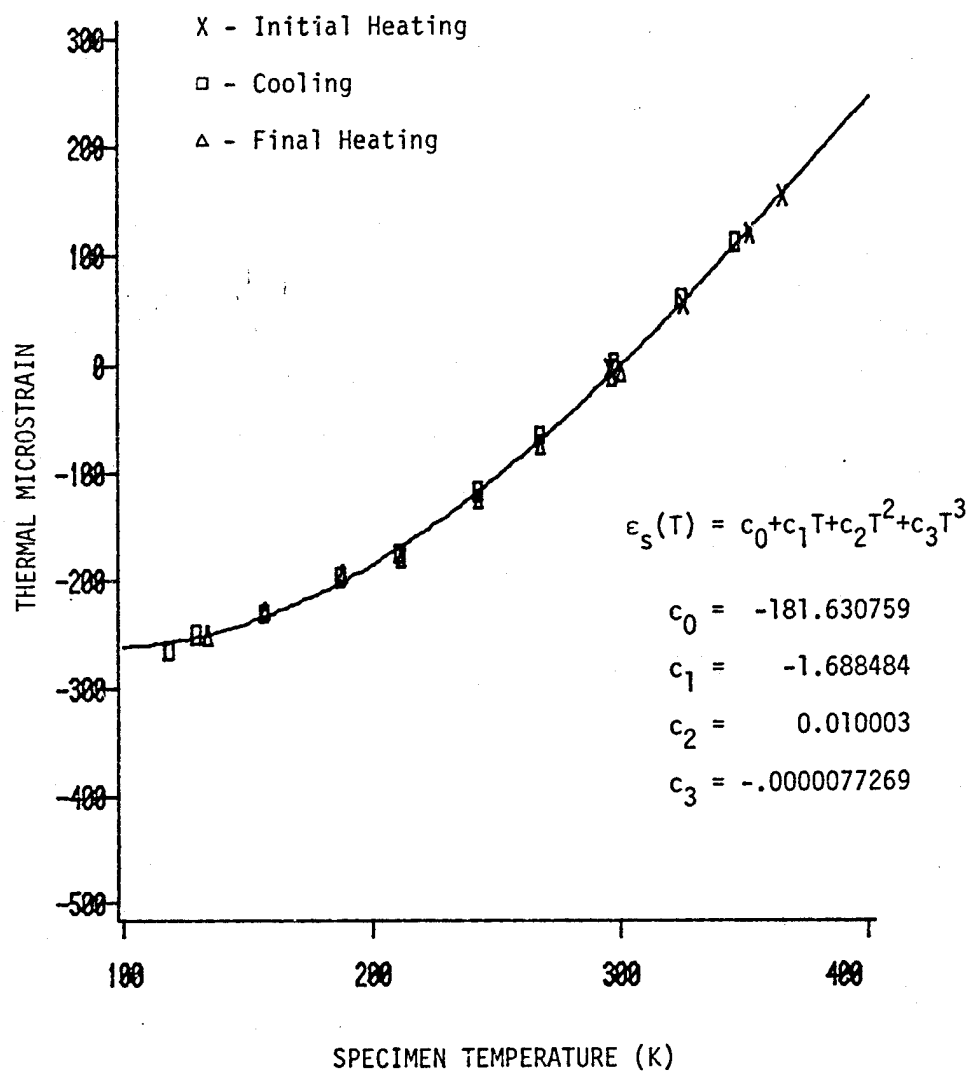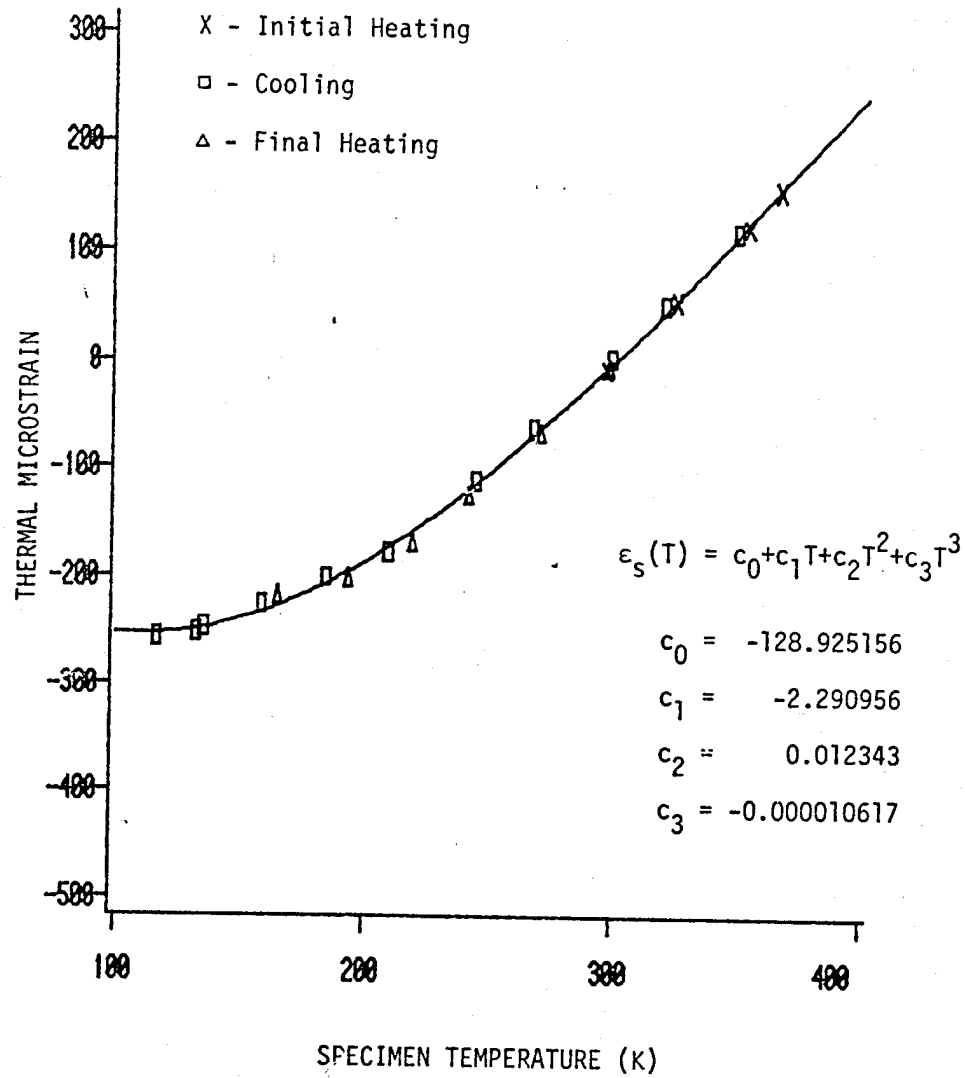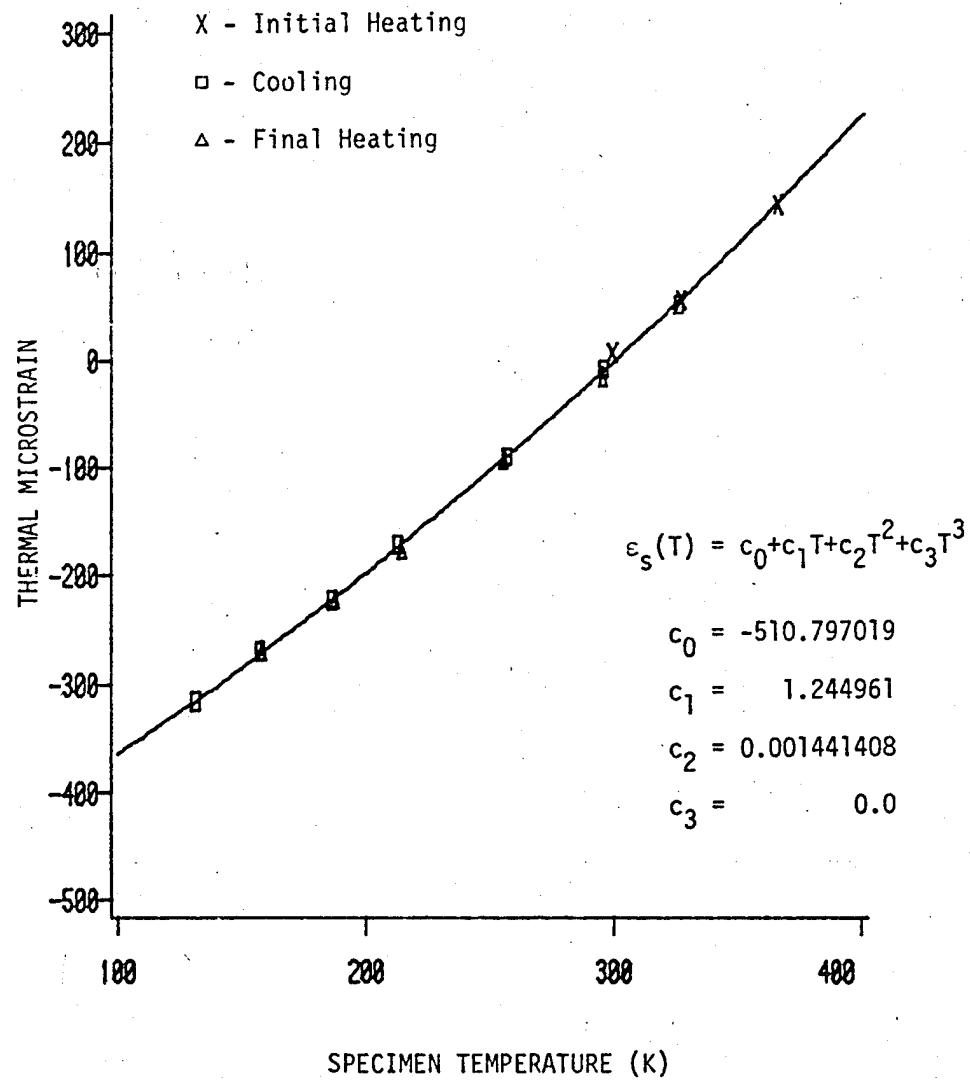
Fig. C.22 Run C6-1
Thermal Strain vs Temperature

X - Initial Heating

□ - Cooling

△ - Final Heating

$$\varepsilon_s(T) = c_0 + c_1 T + c_2 T^2 + c_3 T^3$$

$c_0 = -181.630759$

$c_1 = -1.688484$

$c_2 = 0.010003$

$c_3 = -.0000077269$

THERMAL MICROSTRAIN

SPECIMEN TEMPERATURE (K)

Fig. C.23 Run C6-2
Thermal Strain vs Temperature

Fig. C.24 Run C6-3
Thermal Strain vs Temperature

Fig. C.25 Run C6-4
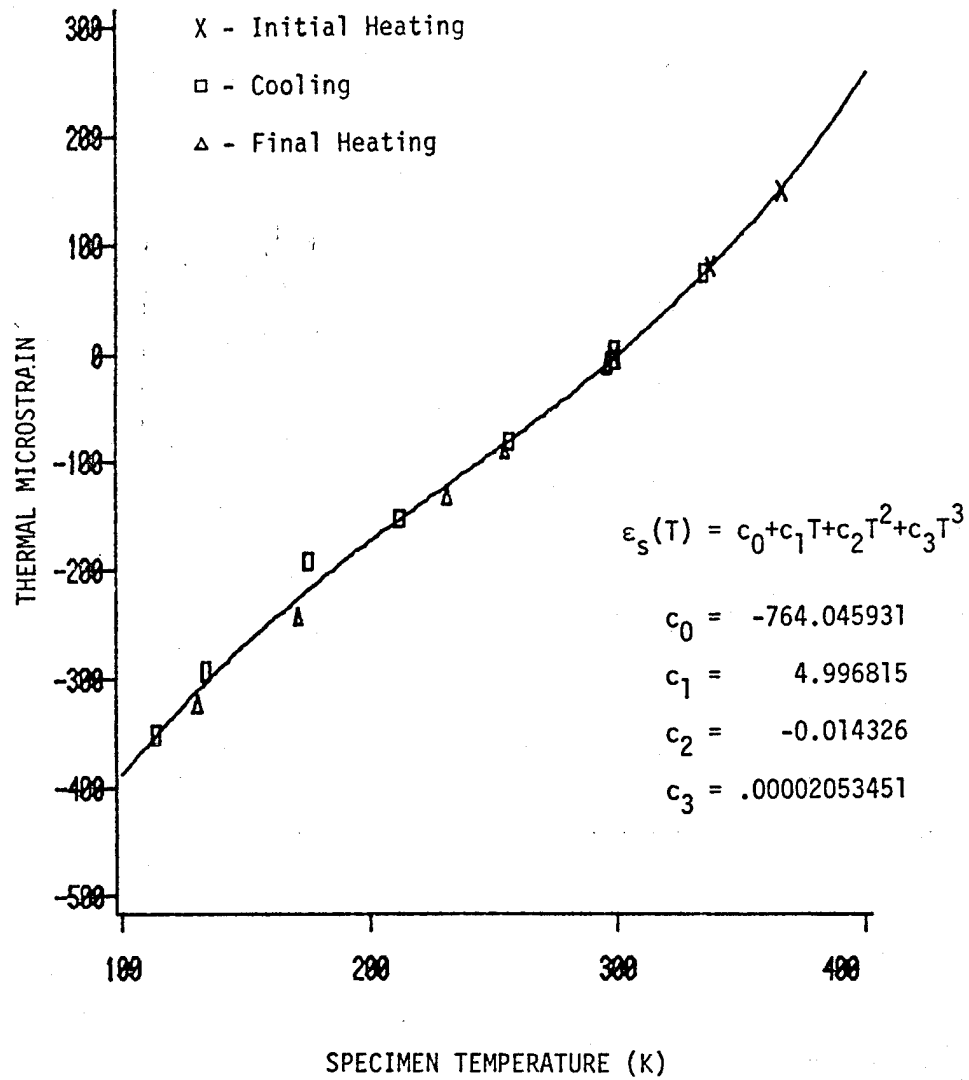Thermal Strain vs Temperature
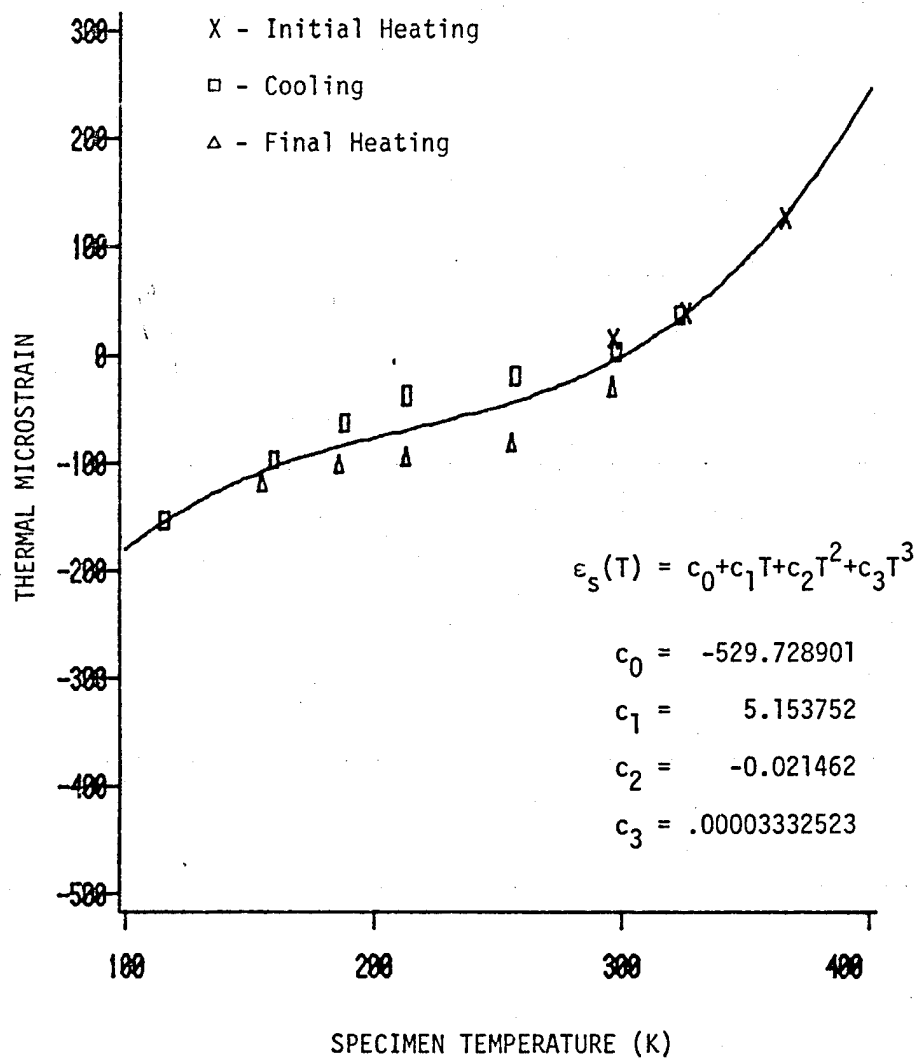
Fig. C.26 Run C8-1
Thermal Strain vs Temperature
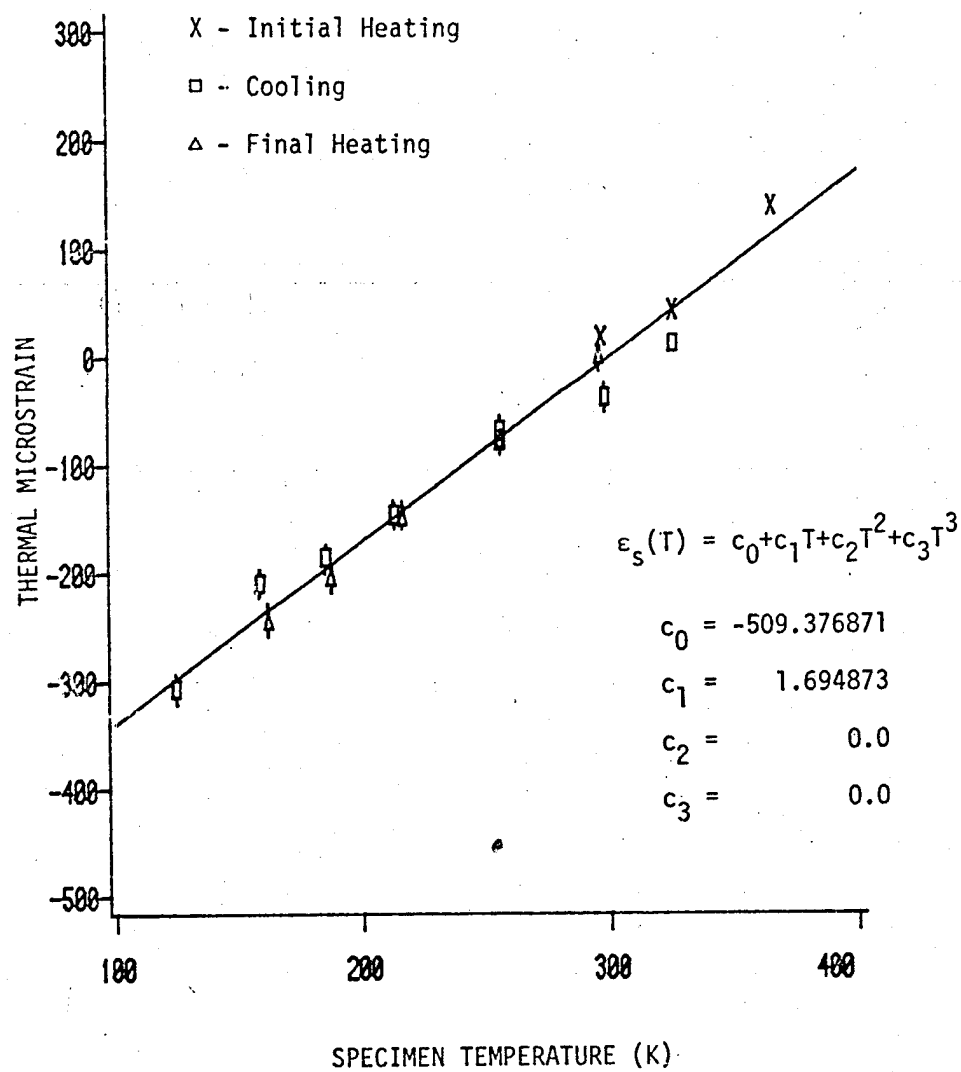
Fig. C.27 Run C8-2
Thermal Strain vs Temperature
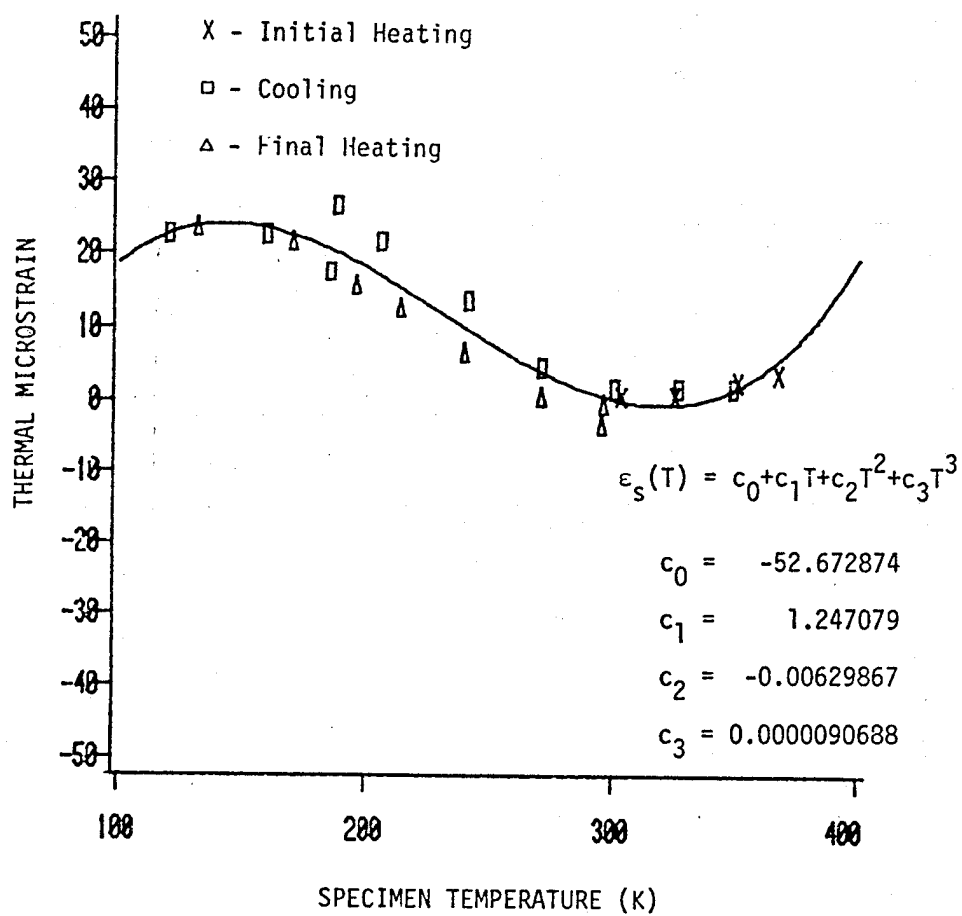
Fig. C.28 Run C8-3
Thermal Strain vs Temperature
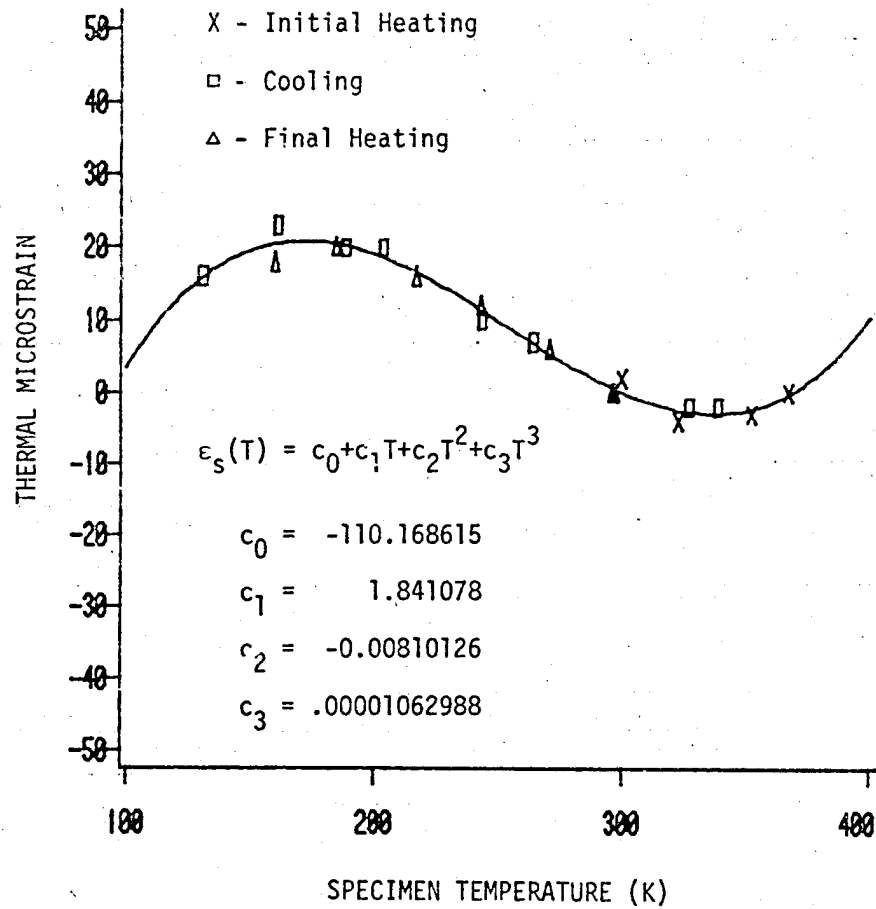
Fig. C.29 Run C7-1
Thermal Strain vs Temperature

X - Initial Heating

□ - Cooling

△ - Final Heating

$$\epsilon_s(T) = c_0 + c_1 T + c_2 T^2 + c_3 T^3$$

$c_0 = -110.168615$

$c_1 = 1.841078$

$c_2 = -0.00810126$

$c_3 = .00001062988$

THERMAL MICROSTRAIN

SPECIMEN TEMPERATURE (K)

Fig. C.30 Run C7-2
Thermal Strain vs Temperature

The figure shows a plot of THERMAL MICROSTRAIN (y-axis, from -50 to 50) versus SPECIMEN TEMPERATURE (K) (x-axis, from 100 to 400).

Legend:
X - Initial Heating
□ - Cooling
△ - Final Heating

$$\varepsilon_s(T) = c_0 + c_1 T + c_2 T^2 + c_3 T^3$$

$c_0 = -94.944994$

$c_1 = 1.697219$

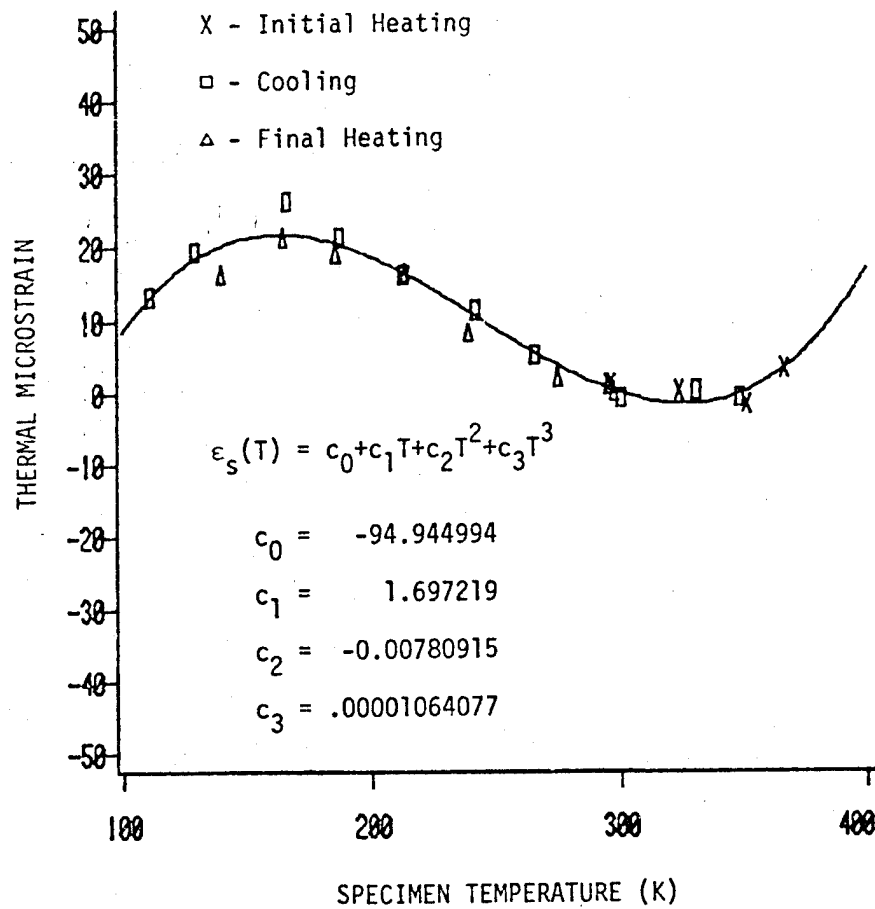$c_2 = -0.00780915$

$c_3 = .00001064077$

Fig. C.31 Run C7-3
Thermal Strain vs Temperature

END
DATE
FILMED
12-28-82
NTIS